Truss and Frames
Recent Advances and New Perspectives

Edited by Aykut Kentli

Truss and Frames - Recent Advances and New Perspectives

Edited by Aykut Kentli

IntechOpen
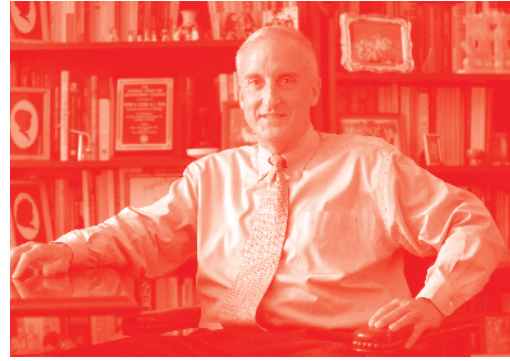
Supporting open minds since 2005

Notice
Statements and opinions expressed in the chapters are these of the individual contributors and not necessarily those of the editors or publisher. No responsibility is accepted for the accuracy of information contained in the published chapters. The publisher assumes no responsibility for any damage or injury to persons or property arising out of the use of any materials, instructions, methods or ideas contained in the book.

We are IntechOpen,
the world's leading publisher of Open Access books
Built by scientists, for scientists

4,600+
Open access books available

120,000+
International authors and editors

135M+
Downloads

151
Countries delivered to

Our authors are among the
Top 1%
most cited scientists

12.2%
Contributors from top 500 universities

CLARIVATE ANALYTICS

BOOK CITATION INDEX

INDEXED

WEB OF SCIENCE™

Selection of our books indexed in the Book Citation Index
in Web of Science™ Core Collection (BKCI)

Interested in publishing with us?
Contact book.department@intechopen.com

Numbers displayed above are based on latest data collected.
For more information visit www.intechopen.com

Meet the editor

Aykut Kentli was born in Isparta, Turkey on September 5th, 1975. He graduated from Istanbul Technical University - Faculty of Mechanical Engineering in 1997. He entered Marmara University as a graduate student in Mechanical Engineering with a specialization in Multi-objective Design Optimization. He received his MSc degree in 2002 and PhD degree in 2008 in Mechanical Engineering. Since 1997, he has been working as an academician at the Mechanical Engineering Department of Marmara University Faculty of Engineering. He commenced lecturing on the courses of Manufacturing Processes, Statics, Strength of Materials, Machine Design and Mechanical System Design. His research interests are design optimization and fuzzy logic and their applications to engineering systems.

Contents

Preface

Trusses and frames have always been the main components of load carrying structures. Even though technological improvements have replaced many standard elements over the time, trusses and frames have held their position as indispensable elements. Today, application areas of these elements have changed from nano to mega structures and many researchers have studied them using several methods (numerical, analytical, and experimental).

This book attempts to explain some recent studies. It is written for academic researchers with an interest in analyzing truss and frame structures. It contains two sections and six chapters. In the first section, different numerical approaches are given. The first chapter presents an approach to assessing the dynamic stability of a structure. As a case study, the two link mechanism is selected. The second chapter shows an application of the finite element method in analysis of catenary-like structures. Results are compared with real data. The third and last chapter of this section presents the use of the differential evolution algorithm to optimize the truss systems considering natural frequencies of vibrations. The second section presents three different studies on obtaining lightweight structures. The fourth chapter reviews studies using topology optimization methods to find suitable geometry to obtain lightweight structures. The fifth chapter presents several design solutions to light combined structures. The sixth chapter focuses on finding suitable material properties for the sandwich core model used in analysis of parts built by direct metal sintering method. We hope that the book is helpful to researchers in the field of analysis of truss-frame structures and related areas.

Dr Aykut Kentli
Professor,
Marmara University,
Engineering Faculty,
Mechanical Engineering Department,
Istanbul, Turkey

Section 1

Numerical Analysis of Structures

Dynamic Stability of Open Two-Link Mechanical Structures

Leonid Kondratenko and Lubov Mironova

Abstract

The chapter deals with the assessment of the dynamic stability of elements selected from the truss or frame construction, which contains input and output parts (links) connected by a force line. From the aggregate of all factors, the resulting force factors and reactions are considered. Instead of the commonly used study of the moving of parts, a new method has been applied, consisting in the study of fluctuations in the speeds of movement and stresses. For this purpose, two partial differential equations are derived that relate the acceleration and the rate of voltage change to the gradients of these variables along the line of force. Using the Laplace transform obtained, the general equations of motion of the slave link. A technique for assessing the degree of distribution of force line parameters is derived, and the conditions for the loss of dynamic stability are identified. It is shown that in this mode, the destruction element of the truss or the frame is possible.

Keywords: frame, truss, two-link element, force line, speed, stress, partial derivative, differential equation, dynamic stability

1. Introduction

In various designs, parts that transmit any motion are often used. Any such design often consists of an input and an output link connected by a force line. With the perception of the load, either compression (stretching) or twisting takes place here. Usually, such elements are checked for longitudinal stability, according to Euler's criterion [1], or for the ultimate twisting. However, such devices often perceive variable loads, for example, wind, shock, etc., at which various vibrations occur. In this regard, it is advisable to evaluate the dynamic stability, which can manifest itself in the form of self-oscillatory regimes, both for the whole truss structure and for its elements, or in the form of sudden destruction. The proposed work is devoted to the study of the loss of dynamic stability of the elements of a truss or frame.

The stability problem of the movement of mathematics and mechanics has been studied since the nineteenth century. To solve such problems, the criteria and theories of Routh E., Gurwitz A., Lyapunov A., Chetayev N., Mikhailov A., Nyquist H., Bolotin V., Popov E. [2–8], etc. are used.

In the last years, many developments have been made, both in the theory and applications of the subject. However, accurate analytical solutions in the calculations of vibrations of a structural element were obtained in rare cases. Typically, calculations are performed approximately. Simplifications are made when choosing a design scheme for the mechanism. In such cases, negligible features of the system are neglected, and the main parameters that determine the nature of the phenomenon are distinguished.

In most cases, a method is specified in which parts of complex geometric shape (springs, crankshafts, etc.) are considered as equivalent straight bar or nonlinear elastic elements are replaced by linear elements. This approach allows replacing a mechanical system with concentrated masses with a system with distributed parameters [9]. Thus, simplifications are allowed that lead to the loss of objective data.

Some publications [10, 11] provide solutions to such problems by an approximate method with the replacement of the corresponding functional equations by suitable finite-dimensional difference schemes. As a result, the authors come to the problem of optimal control of the approximating system, which is described by equations in finite differences or the system of ordinary differential equations [9]. Then there is a need to consider the maximum principle and evaluate approximation methods. Such questions have not enough yet been investigated.

Some specialists of mechanical, for example, the authors of the Encyclopedia of Engineering Industry, Fedosov E., Krasovsky A., Popov E., propose to evaluate the stability of mechanical systems with distributed parameters by dispersion relations, i.e., according to the internal properties of the physical process. Here we use differential equations with variable coefficients that characterize the process under consideration. In this case, the solution of differential equations should be sought by numerical methods [12].

The condition for the stable operation of a system with distributed parameters was formulated in [13, 14]. The mathematical essence of the stability condition is formulated as follows:

If in the subspace $W_\varphi = 0$ the process $\varphi \equiv 0$ is stable under integrally small perturbations with respect to the measure $\|\rho\|$, and in the subspace $W_\varphi < 0$ – asymptotically stable under integrally small perturbations with measure $\|\rho\|$, then in a neighborhood Z_R for any $\delta(\varepsilon, t_0) > 0$, there exists a number such that for $t \geq T$ it is true $\rho[\varphi(\cdot, t)] < 2\delta$, if $\rho[\varphi(\cdot, t_0)] < \delta$ and $\rho[h(x)] < \delta$. Here, φ are the parameters of the process; $h(x)$ is a vector function of admissible solutions.

At present, it has not been possible to find scientific publications in which stability criteria are sufficiently clearly formulated in the study of open two-link mechanical systems with distributed parameters in the presence of significant nonlinearities.

These mechanisms are widely used by technicians. Therefore, it is very important to develop such methods that would make it possible to more accurately mathematically formalize the functioning processes and determine the zones of stable and unstable operation of these mechanisms.

In this regard, the proposed work attempts to consider in more detail the stability issues of these mechanical systems.

2. Statement of the problem

The reliability of the functioning of the noted mechanisms under external variable loads is largely determined by the speeds of the links and the stresses in the force lines. Therefore, there is a need to study the Equations [15]

$$\frac{d\Omega_j}{dt} = \sum_{i=1}^{n} \frac{\partial\Omega_j}{\partial\xi_i} f_i, \tag{1}$$

where ξ_i are the coordinates of the system, $f_i = d\,\xi_i/dt$, t is the time, and Ω_j is the speed of the technological object.

Then the investigation reduces to solving equations

$$\frac{d\xi_i}{dt} = f_i(t, \xi_1, \xi_2, \ldots, \xi_n). \tag{2}$$

If such a path seems natural for specialists in control systems, then for the specialists-mechanics, it may seem unusual, since they often solve the problem of determining the change of coordinates and the shape of oscillations [16–21]. Such processes are usually investigated by methods of the theory of elasticity, for example, using the equation [22, 23]

$$v\frac{\partial^2 u}{\partial t^2} - \frac{\partial}{\partial x}\left(Ef\frac{\partial u}{\partial x}\right) = Q(x,t), \tag{3}$$

whose solution is sought in the form

$$u(x,t) = \sum_{i=1}^{\infty} H_i\theta(x)\sin\left(p_i t + \alpha_i\right). \tag{4}$$

where v and E are mass and elastic characteristics of the mechanical highway, f is cross-sectional area, Q is intensity of external load, and H_i, θ, p_i, and α_i are constants determined from the initial conditions.

In the case of using the Lagrange equation of the second kind, the oscillations of the kinetic (T) and potential energy (U) are considered. The Lagrange equation of the second kind has the form

$$\frac{d}{dt}\left(\frac{\partial T}{\partial\dot{q}}\right) - \frac{\partial T}{\partial q} = Q. \tag{5}$$

Here

$$Q = -\frac{\partial U}{\partial q}. \tag{6}$$

The parameters of the movement of the mechanism are determined from Eq. (5) after some transformations.

These Eqs. (5, 6) which are the basis of many papers on the dynamics of machines, for example, [21, 24, 25], etc., allow, under given boundary conditions, to estimate the change in the displacements of rod section, pipe string, etc. in time and space.

On the one hand, such information is redundant if it is necessary to take into account the interconnection of a large number of factors. For example, to assess the performance of the system, it is enough to know under what conditions self-oscillations occur (i.e., stability is lost), and at what not.

On the other hand, due to the lack of explicit information about the stresses developed in the dynamic process, it is difficult to estimate the probability of part failure.

In the above approaches, such methods of solving problems are specified in which a linear relationship between stresses and displacements of points of a solid body is adopted. According to the accepted linear dependence, these quantities are recalculated. These approaches may not always be applicable, since it is known from rheology that the elastic modulus can depend on the vibration frequency [26, 27].

In addition, depending on the stresses, the rod can be bent and thereby change the peculiarities of the formation of force factors at the links of the mechanism. At the same time, various nonlinear effects, including the essential ones, such as backlash, have a significant impact on the functioning. In this regard, there is a need to develop a method where the oscillations are clearly taken into account speeds and voltages, as well of various nonlinearities.

3. Basic equations

To solve this problem, it is assumed that in dynamics the elements of a truss or frame can be represented as models in **Figure 1**.

In accordance with the theory of strength of materials [1], part of the links of a mechanical system can be represented as a separate element, on which, in addition to external forces, bond reactions act. Therefore, during vibrations, the ends of such an element move with certain speeds, and force factors (F_c, M_r) are the corresponding resulting factors. To this we add viscous resistance (h), which we will consider as resistance to the movement of a particular unit from the side of the entire or adjacent part of the structure to this element (**Figure 1**).

When considering longitudinal vibrations in a straight solid rod, we use the equation quantity of motion in differential form for the case of the absence of mass forces [28]

$$\rho \frac{\partial \upsilon}{\partial t} = \frac{\partial \sigma}{\partial x} \tag{7}$$

and the equation of longitudinal oscillations [27]

$$\frac{\partial^2 u}{\partial t^2} = \frac{E}{\rho} \frac{\partial^2 u}{\partial x^2}. \tag{8}$$

where υ is a speed of longitudinal displacement ($\upsilon = \partial u/\partial t$), u is the displacement along the x-axis, σ are longitudinal (normal) stresses, ρ is density of the material, and E is modulus of elasticity.

Let us assume at this stage that E = const and ρ = const. We determine the derivative $\partial \upsilon/\partial t$ from Eq. (7) and substitute it in the left side of Eq. (8). We therefore have
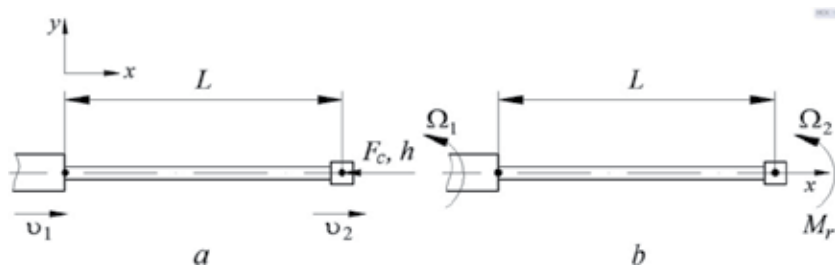
Figure 1.
Models of a rod with a mass: (a) with longitudinal vibrations; (b) with torsional vibrations.

$$\frac{1}{\rho}\frac{\partial\sigma}{\partial x} = \frac{E}{\rho}\frac{\partial^2 u}{\partial x^2}. \tag{9}$$

We integrate the Eq. (9) by x, assuming that for $x = 0$, $\sigma = $ const:

$$\frac{1}{E}\int_0^x \frac{\partial\sigma}{\partial x}dx = \int_0^x \frac{\partial^2 u}{\partial x^2}dx. \tag{10}$$

We finally obtain

$$\frac{1}{E}(\sigma_x - \sigma_0) = \left.\frac{\partial u}{\partial x}\right|_x - \left.\frac{\partial u}{\partial x}\right|_{x=0}. \tag{11}$$

Denote the current value of the stress σ_x by σ. Given that the surface forces acting on each point of the cross section of the elementary volume are directed in the opposite direction from the direction of the speed of movement, we rewrite the resulting equation in the form

$$\rho\frac{\partial v}{\partial t} = -\frac{\partial\sigma}{\partial x}. \tag{12}$$

We therefore have

$$\frac{1}{E}\frac{\partial\sigma}{\partial t} = -\frac{\partial v}{\partial x}. \tag{13}$$

When considering torsional vibrations, we assume that the movement of the sections is absent and the elastic vibrations are described by the equation

$$\frac{\partial^2\varphi}{\partial t^2} = \frac{G}{\rho}\frac{\partial^2\varphi}{\partial x^2}. \tag{14}$$

where φ and x are the angle of rotation of the section of the rod and the coordinate (**Figure 1b**) and G is the shear modulus of the material.

In addition, we use the equation quantity of motion in differential form for an elementary section of a rod with an outer radius r at $\rho = $ const [28, 29]

$$\rho r\frac{\partial\Omega}{\partial t} = -\frac{\partial\tau}{\partial x}, \tag{15}$$

where Ω is the speed of rod cross section ($\Omega = \partial\varphi/\partial t$) and τ is maximum shear stresses of rod cross section.

From comparison Eqs. (14) and (15), we arrive at the equation

$$G\frac{\partial^2\varphi}{\partial x^2} = -\frac{1}{r}\frac{\partial\tau}{\partial x}. \tag{16}$$

We integrate this equation over coordinate x. We finally obtain

$$rG\frac{\partial\varphi}{\partial x} = rG\left.\frac{\partial\varphi}{\partial x}\right|_0 - (\tau_x - \tau_0) = -\tau + B_\tau. \tag{17}$$

Here B_τ is constant characterizing the stress at the initial conditions $x = x_0$ and $t = t_0$.

We differentiate the derived Eq. (17) over t. We have

$$rG\frac{\partial\Omega}{\partial x} = -\frac{\partial\tau}{\partial t}. \qquad (18)$$

The system of Eqs. (12), (13), (15), and (18), first published in manuscript [29], makes it possible to describe changes in stresses in the elementary volume and velocity of movement of the elementary sections of solid-state lines. These are also applicable of the elementary sections of the solid (of the frames and of the trusses).

It should be noted that the process of motion transmission in systems with hydraulic lines is characterized by the equations [30].

$$\frac{\partial v}{\partial t} = -\frac{1}{\rho_0}\frac{\partial P}{\partial x} - 2\tau_0\rho_0 r_0; \quad \frac{\partial P}{\partial t} = -\kappa\frac{\partial v}{\partial x}, \qquad (19)$$

where ρ_0 is the initial density of the medium, P is line pressure, κ is reduced modulus of elasticity of the line, τ_0 is shear stress on the pipe wall, and r_0 is the radius of the pipe section.

Thus, the transfer of motion in solid and liquid media can be described by similar equations. This is shown in the analysis of the hydraulic drive operation [29].

4. Analysis of the Zener model

The equations of motion for the elementary volume of a substance with relatively low speeds of displacement are obtained above. However, in the event of any abrupt changes caused by either external influences or rapidly occurring vibration phenomena, there is a need for a deeper study of the process of motion transmission in mechanical systems [31].

A number of Maxwell, Voigt, and Zener phenomenological models have been developed for this problem. We consider the more general Zener model [26, 27] (**Figure 2**).
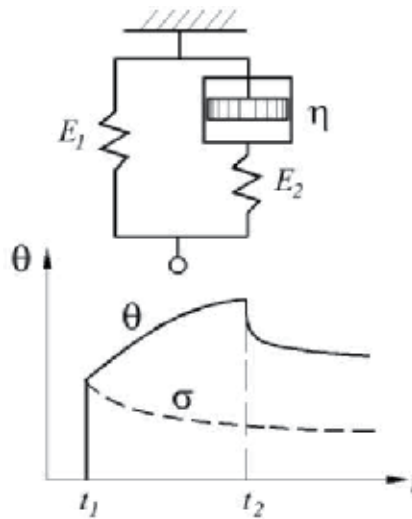
Figure 2.
Zener rheological model: θ is deformation; η is viscosity; σ is normal stress; t is time.

Here it is believed that there is a body that, under the action of stress, is elastically deformed and at the same time can flow. When stress is applied when $t = t_1$, the springs are instantly deformed by magnitudes σ/E_1 and σ/E_2, and the piston starts to move evenly with speed $(d\sigma/dt)/\eta$.

The differential equation is written in the form

$$\sigma + \frac{\eta}{E_2}\frac{d\sigma}{dt} = E_1\theta + \eta\frac{d\theta}{dt}. \tag{20}$$

Here, E_1 and E_2 are the isothermal and adiabatic modulus of elasticity, respectively.

We transform Eq. (20) into an operator form

$$D\sigma = E_2 D\theta - \frac{\sigma - E_1\theta}{\tau_\varepsilon}. \tag{21}$$

where

$$D \equiv \frac{d}{dt}; \; \tau_\varepsilon = \frac{\eta}{E_2}. \tag{22}$$

Here τ_ε is the relaxation time under the condition of constant deformation.

We perform another transformation

$$\sigma\left(D + \frac{1}{\tau_\varepsilon}\right) = \theta E_2\left(D + \frac{1}{k_e\tau_\varepsilon}\right). \tag{23}$$

Here $k_e = E_2/E_1$.

Passing under zero initial conditions to Laplace transformations [29], we rewrite the Eq. (23) in the form

$$\sigma(s)\left(s + \frac{1}{\tau_\varepsilon}\right) = \theta(s)E_2\left(s + \frac{1}{k_e\tau_\varepsilon}\right). \tag{24}$$

Here, we replaced the operator D with a complex variable with ($D = s$), and $s = u + jv; j = (-1)^{1/2}$.

The Laplace image of the stress change from (18), taking into account the jump-like deformation $\theta(t) = \theta_0 1(t)$, is written in the form [32]

$$\sigma(s) = \theta_0 E_2 \frac{s + 1/k_e\tau_\varepsilon}{s(s + 1/\tau_\varepsilon)}. \tag{25}$$

We define the original by means of residues relative to the poles. We then have

$$\sigma(t) = \theta_0 E_2\left[\frac{1}{k_e} + \left(1 - \frac{1}{k_e}\right)\exp\left(-\frac{t}{\tau_\varepsilon}\right)\right] = \theta_0 E_1\left[1 + \left(\frac{E_2}{E_1} - 1\right)\exp\left(-\frac{t}{\tau_\varepsilon}\right)\right]. \tag{26}$$

From this expression, it follows that when $t_1 = 0$, i.e., at the time of a jump-like change in the relative deformation of the rod, the stress is $\sigma(0) = \sigma_0 E_2$, but then with time the stress decreases, relaxes, at $t_2 > \tau_\varepsilon$ to the value $\sigma(t_2) = \theta_0 E_1$. This conclusion is mathematically obtained in [29], and the process is illustrated by the graph in **Figure 2**.

Obviously, the elastic modulus E_2 corresponds to the adiabatic deformation process, and E_1 corresponds to the isothermal process.

Physically, this can be represented as follows. Initially, an adiabatic, without heat transfer, convergence of atoms in metal crystals takes place, but at the same time the entire atomic system becomes unbalanced—non-equilibrium. In order for the system to reach an equilibrium state, a relaxation time $\tau_\varepsilon = \eta/E_2$ is necessary, when the atoms, having received their share of thermal energy, occupy a new position.

Note. In physics [33], elastic oscillations in some cases are interpreted as the motion of a phonon gas. In this case, the relaxation of the internal energy in the crystal lattice is described by the kinematic equation for phonons. Acoustic relaxation is always accompanied by sound absorption, its dispersion, and the dependence of the speed of sound on frequency. The physical encyclopedia for solid dielectrics suggests estimating the relaxation constant from the phonon lifetime

$$\tau_\varepsilon \cong \tau_f = 3\lambda/\left(Cc_{av}^2\right), \tag{27}$$

where C is the lattice heat capacity, λ is thermal conductivity coefficient, and c_{av} is the average value of the speed of sound.

If the deformation will change according to the harmonic law, then the stress will also change according to the harmonic law, but with a slightly different amplitude and phase advance, depending on frequency.

The ratio modulus $\sigma(\omega)/\theta(\omega)$ and phase shift φ are calculated from (23) using expressions [29].

$$\left|\frac{\sigma(\omega)}{\theta(\omega)}\right| = E_1 \frac{\sqrt{1 + (k_e \tau_\varepsilon \omega)^2}}{\sqrt{1 + (\tau_\varepsilon \omega)^2}}; \tag{28}$$

$$\phi = arctg(k_e \tau_\varepsilon \omega) - arctg(\tau_\varepsilon \omega). \tag{29}$$

where ω is the circular oscillation frequency.

The peculiarity of the passage of a harmonic signal through a metal is illustrated in **Figure 3**.

Here are graphs of the functions $E = E(\omega)$ and $\varphi = \varphi(\omega)$. And here is $\tau'_\varepsilon = k_e \tau_\varepsilon$.

The physical meaning of the function $E(\omega)$ is illustrated by two cases.

The first case: when $\omega < 1/\tau'_\varepsilon$, we have

$$|E(\omega)| = E_1. \tag{30}$$
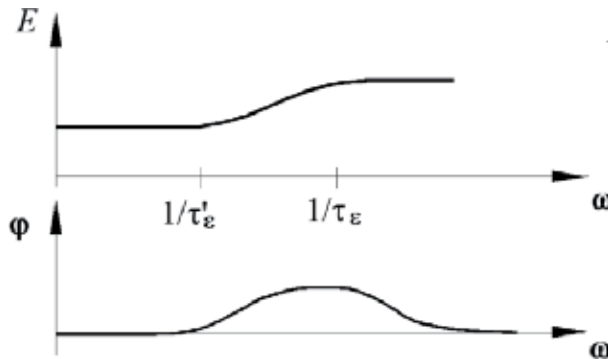
Figure 3.
Passage of a harmonic signal through a metal.

The modulus function $E(\omega)$ is equal to the isothermal modulus of elasticity.
The second case: when $\omega > 1/\tau_\varepsilon$, we have

$$|E(\omega)| = E_2. \tag{31}$$

The modulus function $E(\omega)$ is equal to the adiabatic modulus of elasticity.

From Eq. (23), it follows that the ratio $\sigma(\omega)/\theta(\omega)$ describes some complex function, which can be called the function of the generalized elastic modulus $E_\omega(s)$, i.e., we have

$$E_\omega(s) = E_2 \frac{s + (k_e\tau_\varepsilon)^{-1}}{s + (\tau_\varepsilon)^{-1}} = E_u(\omega) + jE_v(\omega), \tag{32}$$

where $E_u(\omega)$ and $E_v(\omega)$ are, respectively, the values of the function $E_\omega(\omega)$ along the real and imaginary axes of the complex plane (U, jV).

It follows from the above that the value of the elastic modulus strongly depends on the experimental conditions, in particular, on the oscillation frequency, and on the relaxation spectrum. So, for casting steel 1X15H15M2K3BT, the static modulus of elasticity is $E_{st} = 1.617 * 10^5$ MPa, and dynamic is $E_\omega = 2.058 * 10^5$ MPa.

If the frequency value is equal to $\omega = (\tau_\varepsilon)^{-1}$, then this may have a certain impact on the properties of the mechanical system.

Since alloys, such as steel, contain different phases, it is likely that each of them will have its own combination of E_2, E_1, and τ_ε. In this case, you may have to take into account the average relaxation time, the width relaxation of spectrum, etc.

5. Derivation of the initial equations

Let us turn further to the longitudinal oscillations.

The interaction of the elastic wave is largely with the interface of the media due to the wave impedance, which is determined by the relation [34]. It follows that

$$-\frac{\sigma}{v} = \rho a_1, \tag{33}$$

where a_1 is the velocity of propagation of longitudinal oscillations in the medium.

When considering harmonic oscillations propagating along a line, we usually study the wave resistance in operator form or mechanical impedance

$$Z_b(j\omega) = \frac{\sigma(j\omega)}{v(j\omega)}. \tag{34}$$

Referring to Formula (34) and taking into account that

$$a_1 = \Theta\sqrt{\frac{E}{\rho}}, \tag{35}$$

where [34]

$$\Theta = \sqrt{\frac{1-\mu}{(1+\mu)(1-2\mu)}}, \tag{36}$$

we write

$$Z_b(j\omega) = \rho(\omega)\Theta\sqrt{\frac{E_\omega(j\omega)}{\rho(j\omega)}} = \Theta\sqrt{E_\omega(j\omega)\rho(j\omega)}. \tag{37}$$

Note that the ratio $E_v/E_u = tg\,\xi$ characterizes the magnitude of internal friction and ξ determines the phase on which the change of stress is ahead of the change in deformation.

Then Eq. (37) becomes

$$Z_b(j\omega) = \frac{\sigma(j\omega)}{v(j\omega)} = \Theta\sqrt{E_u(\omega)\rho(\omega)}\sqrt{1 + j\frac{E_v(\omega)}{E_u(\omega)}}. \tag{38}$$

If ρ = const and Θ = 1, then the last equation may be written in the form

$$Z_b(j\omega) = \frac{j\omega E_u(\omega)\sqrt{\rho/E_u(\omega)}\sqrt{1 + jE_v(\omega)/E_u(\omega)}}{j\omega} = \frac{E_u(\omega)\theta(j\omega)}{j\omega}. \tag{39}$$

Here

$$\theta(j\omega) = \pm\sqrt{j\frac{\omega}{E_u(\omega)}[\rho j\omega + \psi(\omega)]}; \ \ \psi(\omega) = -\frac{\rho\omega E_v(\omega)}{E_u(\omega)}. \tag{40}$$

Internal friction in solids ψ can play a significant role. For example, it is known that magnesium alloys and a number of other materials have very good vibration-insulating properties, largely due to internal friction. At the same time, for steels this value is small and it is often neglected.

The dynamic features of lines with parameters distributed over length (in principle, parameters are distributed in any line) are characterized by the operator coefficient of wave propagation, which, in Laplace images, can be written in the form [29, 31]

$$\theta(s) = \pm\sqrt{\frac{s}{E_u(\omega)}[\rho s + \psi(\omega)]}. \tag{41}$$

Then, when E_v = 0, ρ = const, and $E_u = E$, the wave resistance will be

$$Z_b(s) = \frac{\sigma(s)}{v(s)} = \frac{\theta(s)E}{s}. \tag{42}$$

From where it also follows

$$\theta(s) = \frac{sZ_b(s)}{E}. \tag{43}$$

Conducting a one-dimensional Laplace transform [30] of Eqs. (13) and (14) for longitudinal oscillations with zero initial conditions and taking into account that with the accepted assumptions

$$\theta(s) = \pm s\sqrt{\frac{\rho}{E}}, \tag{44}$$

we obtain

$$\rho s v(s) = -\frac{d\sigma(s)}{dx};\tag{45}$$

$$E\frac{dv(s)}{dx} = -s\sigma(s).\tag{46}$$

The solution of the system of Eqs. (45) and (46) allows to find for the selected section the instantaneous deviations from the steady-state values of stress and speed of movement sections of rod. Each of these quantities will be the sum of the quantities of the same name, determined in the front of the perturbation propagating in the forward and reverse directions. The instantaneous deviations of the marked variables, as well as the peculiarities of the disturbance propagation along the line, depend on the physical and geometric properties of the line.

Differentiating Eq. (23) with respect to x, then eliminating the derivative $dv(s)/dx$ using Eq. (24), and applying relation (20), we obtain

$$\frac{\partial^2\sigma(s)}{\partial x^2} - \theta^2(s)\sigma(s) = 0.\tag{47}$$

This equation is a second-order differential equation with constant coefficients. The solution is

$$\sigma(s) = C_1 \exp\left[\theta(s)x\right] + C_2 \exp\left[-\theta(s)\right].\tag{48}$$

The integration constants C_1 and C_2 are determined by the boundary conditions. Let at $x = 0$

$$\sigma(s,x) = \sigma_1(s,0); \frac{\partial\sigma(s,x)}{\partial x} = -\frac{E}{s}\theta^2(s)v_1(s,0).\tag{49}$$

The last condition from (49) is obtained from (45) by replacing $\rho s = \theta^2(s)E/s$. Then, taking into account (49), we get

$$C_1 = \frac{\sigma_1(s,0) - s^{-1}\theta(s)Ev_1(s,0)}{2}; C_2 = \frac{\sigma_1(s,0) + s^{-1}\theta(s)Ev_1(s,0)}{2}.\tag{50}$$

After substituting these dependencies, the solution will be

$$\sigma(s,x) = \frac{\sigma_1(s,0)\{\exp\left[\theta(s)x\right] + \exp\left[-\theta(s)x\right]\}}{2}$$
$$-\frac{s^{-1}\theta(s)E\sigma_1(s,0)\{\exp\left[\theta(s)x\right] - \exp\left[-\theta(s)x\right]\}}{2}.\tag{51}$$

When we introduce hyperbolic functions, then we get

$$\sigma(s,x) = \sigma_1(s,0)ch\left[\theta(s)x\right] - \theta(s)s^{-1}Ev_1(s,0)sh\left[\theta(s)x\right].\tag{52}$$

Having solved the system of Eqs. (47) and (48) with respect to $v(s,x)$ in the manner described, we obtain

$$\frac{\partial^2 v(s)}{\partial x^2} - \theta^2(s)v(s) = 0.\tag{53}$$

For boundary conditions with $x = 0$

$$v(s, x) = v_1(s, 0); \quad \frac{\partial v(s, x)}{\partial x} = -\frac{s\sigma(s, 0)}{E},$$ (54)

We finally obtain

$$v(s, x) = v_1(s, 0)ch[\theta(s)x] - \frac{s\sigma_1(s, 0)sh[\theta(s)x]}{\theta(s)E}.$$ (55)

Movement in two-link elements that occurs within elastic limits can be viewed as the movement of the driven point (link) from the movement of the leading point (link), which is affected by the previous links of the truss, for example, which perceive wind load. If, in the process of oscillation, the output link does not allow the input impulse to pass, then waves of disturbance are reflected from the end of the lines.

Consider the case of a matched load when there are no reflected waves in the system and oscillations in the system do not affect the movement of the driven link due to the attached large mass. In this case, the boundary conditions are the following relations:

$$v(s, l) = v_2(s); \quad v(s, 0) = v_1(s); \quad \sigma(s, l) = \sigma_2(s); \quad \sigma(s, 0) = \sigma_1(s);$$

$$\sigma_2(s) = \frac{F_c(s) + h_n v_2(s) + ms v_2(s)}{f_2}.$$ (56)

Here f_2 is the sectional area of the line in front of the slave link of mass m; h_n and F_c are coefficient of friction loss, proportional to the speed of movement, as well as the resistance force acting on the slave link; l is the length of the line.

Together we solve (52)–(56) by performing the following transformations

$$\sigma_1(s) = \frac{1}{chA}\left[\sigma_2(s) + \frac{1}{s}Ev_1(s)\theta(s)shA\right];$$

$$v_2(s) = v_1(s)chA - \frac{s}{E\theta(s)}shA\left\{\frac{1}{chA}\left[\sigma_2(s) + \frac{1}{s}Ev_1(s)\theta(s)shA\right]\right\};$$

$$v_2(s) = \frac{v_1(s)}{chA} - \frac{s}{E\theta(s)}\sigma_2(s)thA;$$ (57)

$$\left[\frac{v_1(s)}{chA} - v_2(s)\right]\frac{E\,\theta(s)}{s\,thA} = \frac{1}{f_2}[F(s) + h_n v_2(s) + ms v_2(s)].$$

After bringing similar members, we obtain the equation of motion of the driven link of the mechanical system in the form

$$v_2(s)\left[1 + h_n \vartheta_n(s)s + m\vartheta_n(s)s^2\right] = \frac{v_1(s)}{ch[\theta(s)l]} - F_c(s)\vartheta_n(s)s.$$ (58)

Here

$$\vartheta_n(s) = \vartheta_{n0}Z_n(s); \quad \vartheta_{n0} = \frac{l}{Ef_2}; \quad Z_n(s) = \frac{thA}{A}; \quad A = \theta(s)l.$$ (59)

Substituting (58) into the last equation of system (57), we obtain an equation describing the stresses fluctuations in the force line in the vicinity of the slave link in form

$$\sigma_2(s) = \frac{F_c(s) + \upsilon_1(s)(h_n + ms)/chA}{f_2[1 + h_n\vartheta_n(s)s + m\vartheta_n(s)s^2]}. \tag{60}$$

Performing such transformations in relation to torsional vibrations, we obtain

$$\Omega_2(s)\left[1 + h_k\vartheta_k(s)s + J\vartheta_k(s)s^2\right] = \frac{\Omega_1(s)}{chA_k} - M_r(s)\vartheta_n(s)s. \tag{61}$$

Here

$$\vartheta_k(s) = \vartheta_{k0}Z_k(s); \vartheta_{k0} = \frac{l}{GrW_{p2}}; Z_k(s) = \frac{thA_k}{A_k}; A_k = \theta_k(s)l; \theta_k(s) = \pm\sqrt{\frac{\rho}{G}}. \tag{62}$$

Comparing (15), (18), and (19), we can see that the processes of motion transfer in solid and liquid media can be described by similar equations. This is shown when analyzing the operation of the hydraulic drive [9, 35–37].

6. Lemma on the degree of distribution of force line parameters

Eqs. (47) and (48) make it possible to calculate the frequency characteristics of the system, i.e., determine the response of the model to the harmonic change in the speed of the lead link or the resistance force acting on the driven link.

For example, for $\upsilon_1 \equiv 0$ and $s = j\omega$, we obtain the characteristic $W_F(j\omega)$, illustrating the influence of F on υ_2, and the characteristic $W_{F\sigma}(j\omega)$, illustrating the influence of F on σ:

$$W_F(j\omega) = \frac{\upsilon_2(j\omega)}{F_c(j\omega)} = -\frac{\vartheta_n(j\omega)j\omega}{1 + h_n\vartheta_n(j\omega)j\omega + m\vartheta_n(j\omega)(j\omega)^2}; \tag{63}$$

$$W_{F\sigma}(j\omega) = \frac{\sigma_2(j\omega)}{F_c(j\omega)} = \frac{1}{f_2\left[1 + h_n\vartheta_n(j\omega)j\omega + m\vartheta_n(j\omega)(j\omega)^2\right]}. \tag{64}$$

For $F \equiv 0$, we obtain the frequency characteristics $W_\upsilon(j\omega)$, illustrating the effect of υ_1 on υ_2, and $W_{F\sigma}(j\omega)$, illustrating the influence of υ_1 on σ_2. So we have

$$W_\upsilon(j\omega) = \frac{\upsilon_2(j\omega)}{\upsilon_1(j\omega)} = -\frac{ch^{-1}[\theta(j\omega)l]}{1 + h_n\vartheta_n(j\omega)j\omega + m\vartheta_n(j\omega)(j\omega)^2}, \tag{65}$$

$$W_{F\sigma}(j\omega) = \frac{\sigma_2(j\omega)}{\upsilon_1(j\omega)} = \frac{h_n + mj\omega}{f_2ch[\theta(j\omega)l]\left[1 + h_n\vartheta_n(j\omega)j\omega + m\vartheta_n(j\omega)(j\omega)^2\right]}. \tag{66}$$

From (63) to (66), it can be seen that changes in the voltage and speed of movement of the output link are lagging behind changes in input impacts.

We introduce the notation $\alpha = l\,\omega\,(\rho/E)^{1/2}$.

Insofar as

$$Z_n(j\omega) = \frac{th[\theta(j\omega)l]}{\theta(j\omega)l} = \frac{jtg\alpha}{j\alpha} = \frac{tg\alpha}{\alpha}; \ ch(j\alpha) = \cos\alpha, \tag{67}$$

then

$$\vartheta_n(j\omega) = \vartheta_n(\alpha) = \vartheta_{n0}Z_n(\alpha) \tag{68}$$

and cosα are not complex functions.

The graph of the function $Z_n(\alpha)$ is shown in **Figure 4**.

On the whole we conclude that at $k = 1$ $\alpha \to 0$, $Z_n \to 1$; at $\pi/2 + k\pi > \alpha > \pi + k\pi$, $Z_n < 0$. Here $k = 0, 1, 2....n$.

Eq. (58), given this, can be rewritten in the form

$$v_2(s)\left[1 + h_n\vartheta_n(\alpha)s + m\vartheta_n(\alpha)s^2\right] = v_1(s)\cos^{-1}(\alpha) - F_c(s)s\vartheta_n(\alpha). \tag{69}$$

If $\alpha \to 0$, then Eq. (69) is reduced to the well-known equation describing dynamic processes in the mechanism with short lines of force:

$$v_2(s)\left[1 + h_n\vartheta_{n0}s + m\vartheta_{n0}s^2\right] = v_1(s) - F_c(s)s\vartheta_{n0}. \tag{70}$$

The breaks shown in **Figure 4** are mathematically related to the function of tangent. For a real mechanism, this means that motion parameters are rebuilt. Apparently, in this instant, the form of oscillations changes abruptly. Below this feature is discussed in more detail.

The appearance of resonance is described by another expression that defines the conditions for the formation of the maximum amplitude of oscillations.

$$A_F(\omega) = \frac{\vartheta_n(\alpha)\omega}{\sqrt{[1 - m\vartheta_n(\alpha)\omega^2]^2 + [h_n\vartheta_n(\alpha)\omega]^2}} = \left(\sqrt{\frac{[1 - m\vartheta_n(\alpha)\omega^2]^2}{[\vartheta_n(\alpha)\omega^2]} + h_n^2}\right)^{-1}. \tag{71}$$

Thus A_F achieves its maximum when the condition

$$\frac{1 - m\vartheta_n(\alpha)\omega^2}{\vartheta_n(\alpha)\omega} = 0. \tag{72}$$

We show that this condition is similar to the rule for determining natural frequencies. This rule was formulated by Babakov [22].

Consider the following problem. Let the rod hang vertically. At the end of the rod, a load is fixed. The load is assumed to be point (**Figure 5**).
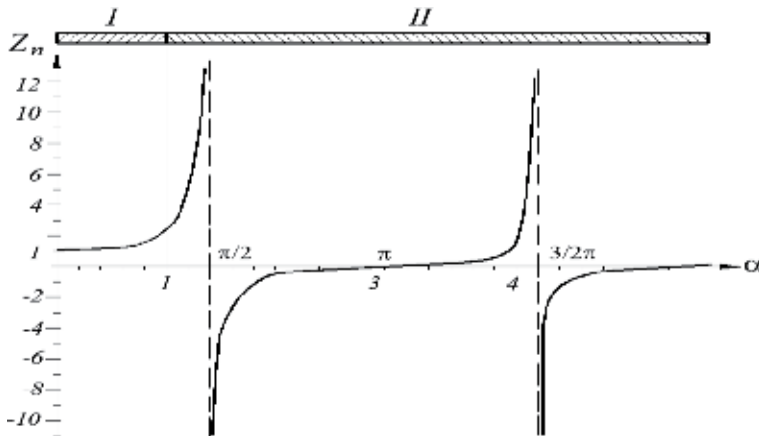
Figure 4.
Change of function Zₙ of dimensionless parameter α: I is the range of admissible function values for systems with lumped parameters; II is the range of admissible values of the function for systems with distributed parameters.
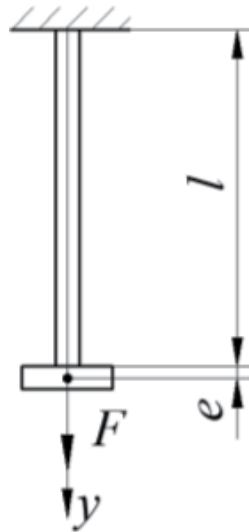
Figure 5.
Cargo suspended on a rod.

Let the mass of the load be m and the ratio of the mass of the rod with the cross-sectional area f to the mass of the load be $a = l\mu/m$. Here μ is the linear mass of the rod.

It is believed that the longitudinal tension of the rod during oscillations is balanced by the force of inertia of the load. This leads to the following condition at the lower end of the rod:

$$Ef\left(\frac{\partial y}{\partial x}\right)_{x=l} = -m\left(\frac{\partial^2 y}{\partial t^2}\right)_{x=l}. \tag{73}$$

At the top end, which is fixed we have $y(0, t) = 0$. At the initial time, the rod is stretched by the force F applied to the lower end and then without the initial speed is left to itself, so that

$$y(x.0) = \frac{Fx}{Ef}; \frac{dy(x, 0)}{dt} = 0. \tag{74}$$

The solution of the problem is reduced to the calculation of the constant B, D, and parameter b values in the equation of the vibration modes

$$\varphi(x) = B\cos(bx) + D\sin(bx), \tag{75}$$

and, moreover, to the calculation of the constants A_i and B_i of the general solution

$$u(x,t) = \sum_{i-1}^{\infty}\left[A_i\cos(p_i t) + B_i\sin(p_i t)\right]\varphi(x) \tag{76}$$

in accordance with the initial conditions (74).

From the first boundary condition (41), it follows that $B = 0$.

After that, from the second condition is the equation of frequencies

$$\beta tg\beta = a, \tag{77}$$

where $\beta = al$.

Thus, the equation of the own modes of oscillations of the rod has the form

$$\varphi_k(x) = D_k \sin\left(\frac{\beta_k x}{l}\right), \quad (k=1,2,3,\dots). \tag{78}$$

Here β_k is the roots of Eq. (77).

The solution of Eq. (78) can be carried out graphically [21].

The lowest natural frequencies corresponding to these values are calculated by the formula

$$\omega = p_1 = \frac{\beta_1}{l}\sqrt{\frac{Ef}{\mu}}. \tag{79}$$

Note that the linear mass of the rod $\mu = \rho f$. Expanding the coefficients, we obtain the original equation

$$\beta \, tg\beta = \frac{lf\rho}{m}. \tag{80}$$

We now turn to Eq. (79) and divide the numerator of the right side by the denominator

$$Ef \frac{\sqrt{\rho/E}}{tg\alpha} = m\omega. \tag{81}$$

We will still carry out a number of transformations. We have

$$Efl \frac{\sqrt{\rho/E}}{m} = l\omega \, tg\alpha; \quad \frac{fl}{m} = \frac{l\omega \, tg\alpha}{\sqrt{E\rho}}. \tag{82}$$

After multiplying both sides of the last equation by ρ and after performing the corresponding transformations, we get

$$\frac{\rho fl}{m} = \alpha \, tg\alpha. \tag{83}$$

Since here the parameters α and β are equivalent, it can be argued that the roots of Eqs. (72) and (80) are the same. This is confirmed by the results of calculations.

The results obtained make it possible to formulate a lemma on the degree of distribution of the parameters of power lines. But for this, we introduce the notation

$$\alpha = l\omega\sqrt{\rho/\chi}, \tag{84}$$

where χ is the elastic modulus of the material of the force line.

We state the lemma as follows. *If the parameters of the mechanical two-link system, characterized by the oscillation frequency ω, length l, density ρ, and the elastic modulus of the material of the force line χ connecting these links, are such that magnitude of the dimensionless coefficient α lies in the interval $0 \leq \alpha \leq 1$, then the wave processes in the lines of force can be neglected.*

This lemma is also valid for systems where torsional vibrations of rods and vibrations in hydraulic systems take place. The criterion on the degree of distribution of the system parameters was first described in the book [29].

7. Dynamic stability of rod systems

Wave phenomena take place in hydraulic, mechanical, electrical environments [4]. As shown above, wave processes take place in systems with lines of any length, but depending on the conditions, they can either be neglected or not ignored. If at the same time there is a transfer of energy to perform any effective work, then the problem of ensuring sustainable functioning inevitably arises.

Publications devoted to the study of the stability of open-loop systems with distributed parameters in the presence of significant nonlinearities, where sufficiently precise criteria are stated, could not be found. Therefore, here outlines the main points of this issue, which were developed in more detail in [9, 29, 35–37].

We algebraically decompose Eq. (58) into two. We have

$$\frac{v_1}{\cos \alpha} = v_2(s) + \vartheta_n(\alpha) f_2 s \sigma(s); \tag{85}$$

$$\sigma(s) f_2 = F_c(s) + h_n v_2(s) + m s v_2(s). \tag{86}$$

Here α corresponds to the expression (84).

The accuracy of the decomposition is easily verified by the inverse solution.

Moving on to the originals of Eq. (58), we do the inverse transform Laplace of functions

$$F_1(s) = \vartheta_n(\alpha) f_2 s \sigma(s) \text{ and } F_2(s) = v_1(s)/\cos \alpha. \tag{87}$$

We have then

$$L^{-1}|F_1(s)| = \frac{1}{2\pi j} \int_{c-j\infty}^{c+j\infty} \vartheta_n(\alpha) f_2 \sigma(s) e^{st} ds = \vartheta_n(\alpha) f_2 \frac{1}{2\pi j} \int_{c-j\infty}^{c+j\infty} s \sigma(s) e^{st} ds = \vartheta_n(\alpha) f_2 \frac{d\sigma}{dt}. \tag{88}$$

$$L^{-1}|F_2(s)| = v_1(t)/\cos \alpha. \tag{89}$$

Then the originals (31) can be written in the form

$$v_1(t)/\cos \alpha = v_2(t) + \vartheta_n(\alpha) f_2 \frac{d\sigma}{dt}; \tag{90}$$

$$\sigma(t) f_2 = F_c(t) + h_n v_2(t) + m \frac{dv_2}{dt}. \tag{91}$$

The system of Eqs. (90, 91) may contain various nonlinearities (yield zone in the stress diagram, nonlinear friction, etc.) and is solved by the updated Runge-Kutta method [9, 38]. The admissibility of such a technique was checked by comparing the frequency characteristics constructed by formulas (63) to (66) and using the above method when introducing harmonic oscillations with different frequencies [29, 35].

In addition, given that the fluctuations of the speeds of movement and stresses (pressure) in mechanical and hydraulic systems can be described by similar equations, we checked the adequacy of the proposed method by means of full-scale and numerical experiments in an electric drive. The results had good convergence [9, 29, 31, 35–37].

In the process of modeling, it turned out that when $Z < 0$ (**Figure 4**), the solution becomes unstable. **Figure 6** shows an example of the process of loss of
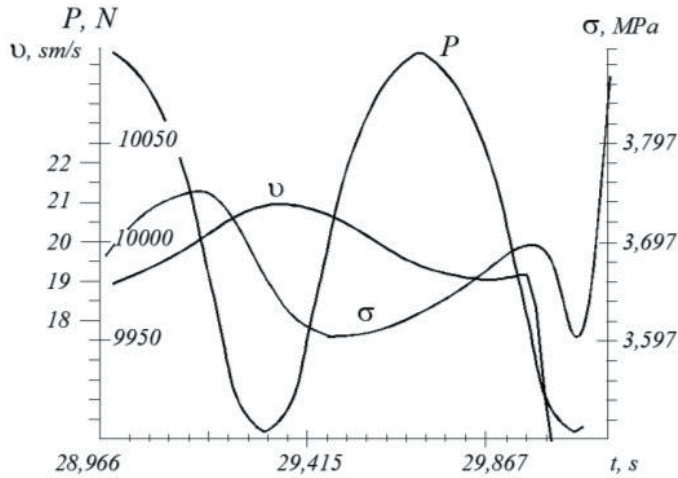
Figure 6.
Loss of stable operation in the mechanical element during longitudinal movement.
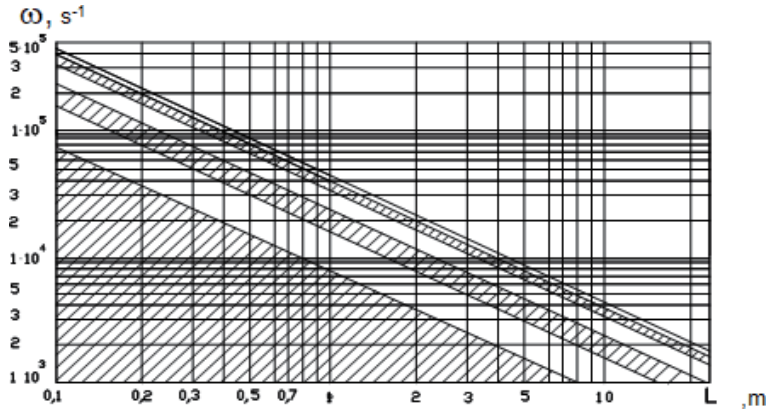
Figure 7.
Zones of steady (shaded) and unstable operation of the mechanical system of longitudinal movement.

dynamic stability in a mechanical element with longitudinal vibrations. For a truss, this means breaking one of the rods.

The areas of dynamic stability for mechanical elements with longitudinal vibrations are shown in **Figure 7**.

8. Conclusions

In trusses under the influence of variable loads, vibrations occur periodically in different elements, characterized by fluctuations in speed and stress. Under certain conditions, due to wave motions in the rods, the shape of the oscillations may change, i.e., lost stability of motion. At this instant, the destruction of the carrier element will occur. The proposed chapter considers the conditions for the occurrence of such an event.

Author details

Leonid Kondratenko* and Lubov Mironova
Moscow Aviation Institute (SNRU), Moscow, Russia

*Address all correspondence to: kondrat.leonid@yandex.ru

IntechOpen

References

[1] Feodos'ev VI. Strength of Materials. Moscow: FML; 2001. p. 558

[2] Routh EJ. Dynamics of a System of Rigid Bodies. London: Macmillan and Co; 1905. p. 484

[3] Mint HA. Ueber die Bedingungen, unter welchen eine Gleichung nur Wurzeln mit negativen reellen Teilen besitzt. Journal of Mathematical Analysis and Applications. 1895;**46**: 273-284

[4] Lyapunov AM. The General Problem of the Stability of Motion. ONTI: Moscow-Leningrad; 1935. p. 473

[5] Chetaev NG. Stability of Motion. Moscow: Gostekhizdat; 1950. p. 176

[6] Mihaylov AV. Mint: The theory of stability of linear feedback circuits with lumped parameters. Journal of Technical Physics. 1939;**1**:20-31

[7] Bolotin VV. Dynamic Stability of Elastic Systems. Moscow: Gostekhizdat; 1956. p. 600

[8] Popov EP. Applied Theory of Control Processes in Nonlinear Systems. Moscow: FML; 1973. p. 583

[9] Kondratenko L, Mironova L. Features of loss of stability of the work of two-link mechanisms that have an infinite number of degrees of freedom. International Journal of Mathematical, Engineering and Management Sciences. 2018;**3**(4):315-334

[10] Berezyanskij YUM. Kondrat'ev YU. G. Spectral Methods in Infinite-Dimensional Analysis. Kiev ANUSSR: Nauk. Dumka; 1988. p. 680

[11] Godunov SK, Ryaben'kij VS. Difference schemes. FML, Nauka: Moscow; 1977. p. 442

[12] Fedosov EA. Engineering Encyclopedia. (Chapter Ed.). Vol. 1–4. Mashinostroenie: Moscow; 2000

[13] Shaginyan SG. On the stability of dynamical systems with distributed parameters for integrally small perturbations. Journal of Works of IPMM NAS of Ukraine. 2009;**18**:200-209

[14] Sirazetdinov TK. Stability of Systems with Distributed Parameters. Novosibirsk: Nauka; 1987. p. 232

[15] Timoshenko S, Woinovsky-Krieger S. Theory of Plates and Shells. McGRAW-HELL BOOK COMPANY: New York-Toronto-London; 1959. p. 591

[16] Dikovich IA. Dynamics of Elastic-Plastic Beams. Sudprom: Leningrad; 1962. p. 291

[17] Lur'e AI. Theory of Elasticity. The Science. Moscow: Nauka; 1970. p. 939

[18] Grigolyuk EI, Selezov NT. Nonclassical Theories of Vibrations of Rods, Plates and Shells. VINITI: VINITI, Moscow; 1973. p. 273

[19] Vol'mir AS. Нелинейная динамика пластинок и оболочек. Moscow: Nauka; 1972. p. 432

[20] Guz' AN, Babich IYU. Three-Dimensional Theory of Stability of Deformed Bodies. Naukova dumka: Kiev; 1985. p. 279

[21] Gluhov LV, Ivanov SD, Lukashina NV, Preobrazhenskij IN. Dynamics, Strength and Reliability of Elements of Engineering Structures. Moscow: ACB; 2003. p. 304

[22] Babakov IM. Theory of Oscillations. GTTL: Moscow; 1958. p. 628

[23] Kolesnikov KS, editor. Engineering Encyclopedia. The Dynamics and

Strength of Machines. Theory of Mechanisms and Machines. Vol. 1, 3. Moscow: Mashinostroenie; 1994

[24] Kolovskij MZ. The Dynamics of Machines. Mashinostroenie: Leningrad; 1989. p. 253

[25] Vul'fson MI. Fluctuations of Machines with Cyclic Mechanisms. Mashinostroenie: Leningrad; 1990. p. 309

[26] Postnikov VS. Internal Friction. Metallurgy: Moscow; 1974. p. 350

[27] Reiner M. Rheology. In: Flugge S, editor. Handbuch Der Physik, vol. VI. Berlin, Germany: Springer; 1958

[28] Sedov LI. Continuum Mechanics. Vol. 1, 2. Nedra: Moscow; 1970

[29] Kondratenko LA. Vibrations and Speed Regulation Methods of Movement of Technological Objects. MRSU: Moscow; 2005. p. 448

[30] Popov DN. Dynamics and Regulation of Hydro-Pneumatic Systems. Mashinostroenie: Moscow; 1977. p. 423

[31] Mironova L, Kondratenko L. Method for the study of dynamic characteristics in the mechanisms of motion transmission. In: Proceedings of the 39th International JVE Conference, June 25–26, 2019; Russia, St. Petersburg. Journal of Vibroengineering Procedia. 2019; 25. pp. 214-219. DOI: 10.21595/vp.2019.20786

[32] Ivanov VA, Chemodanov BK, Medvedev VS. Mathematical Foundations of the Theory of Automatic Control. Vysshaya shkola: Moscow; 1971. p. 727

[33] Prohorov AM. Physical Encyclopedia. Vol. 3. The Great Encyclopedia: Moscow; 1994. p. 704

[34] YAvorskij BM, Detlaf AA. Handbook of Physics. Moscow: Nauka; 1965. p. 942

[35] Kondratenko LA. Calculation of Velocity Variations and Stresses in Machine Assemblies and Components. Sputnik: Moscow; 2008. p. 317

[36] Kondratenko LA, Mironova LI. Imitation of nonlinear drives with distributed parameters of power lines. Journal of Engineering & Automation Problems. 2018;**1**:92-97

[37] Kondratenko LA, Terekhov VM, Mironova LI. About one method of research torsional vibrations of the core and his application in technologies of mechanical engineering. Journal of Engineering & Automation Problems. 2017;**1**:133-137

[38] Kamke E. Differentialgleichungen: Lösungsmethoden und Lösungen. Akademische Verlagsgesellschaft Geest & Portig K.G. Leipzig; 1956

Nonlinear Truss-Based Finite Element Methods for Catenary-Like Structures

Jose Rodolfo Chreim and Joao Lucas Dozzi Dantas

Abstract

This chapter is devoted to an application of a finite element method formulation to forecast the static and mechanical behavior of catenary-like structures subject to general force distributions, whose development was motivated by the need of installing assemblies of containment structures, called log boom lines, upstream a hydroelectric power plant to protect its integrity from the threats that logs carried through the river pose on it. Each log boom is modeled by a tridimensional truss element and the entire lines by assemblages of trusses. While the external forces, modeled with the aid of both simulations from computational fluid dynamics and experiments from a towing tank, originate from both the river stream and the logs that accumulate through the extension of the lines, the internal forces are calculated from classic expressions of solid mechanics; hence, the numerical method imposes equilibrium between them, which ultimately defines the geometry assembly. Verification and validation were performed at both model and prototype scales, and the results corroborated the accuracy of the tool for a series of flow conditions.

Keywords: finite element method, fluid-structure interaction, containment grids, catenary-like, numerical simulation

1. Introduction

The operation of a hydroelectric power plant at the Madeira River is compromised due to the presence of many logs carried through the water stream that can damage the power plant machinery and reduce its production efficiency. To prevent such damage, nine assemblies of containment structures, called log booms (**Figures 1** and **2**), were installed near the power plant and across the river to retain and deflect these logs. Nevertheless, as the influence of logs and stream can exert large loads over the assemblies, they are under the risk of structural failure; so a numerical tool based on the finite element method (FEM) was developed to predict the distributions of loads and equilibrium configurations of the lines, therefore assisting their surveillance and maintenance. The numerical tool was part of a research and development (R&D) project developed by the Institute for Technological Research (IPT), and it can be extended to similar problems in which the structures behave likewise, as is the case of fishing nets and cleaning structures [1]. Moreover, while commercial software could be used for the same purpose, the intrinsic drawbacks of large computation time, automation, and customization
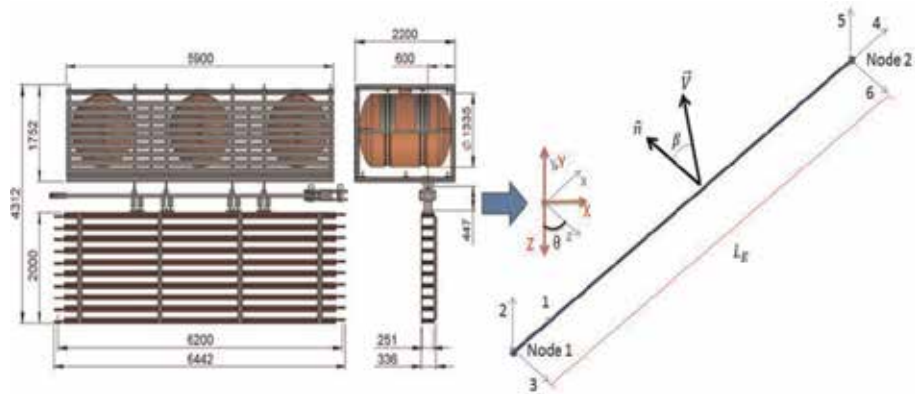
Figure 1.
Log boom unit schematics and its truss element representation with six DoF. The local reference frame is in blue, while the global in red.
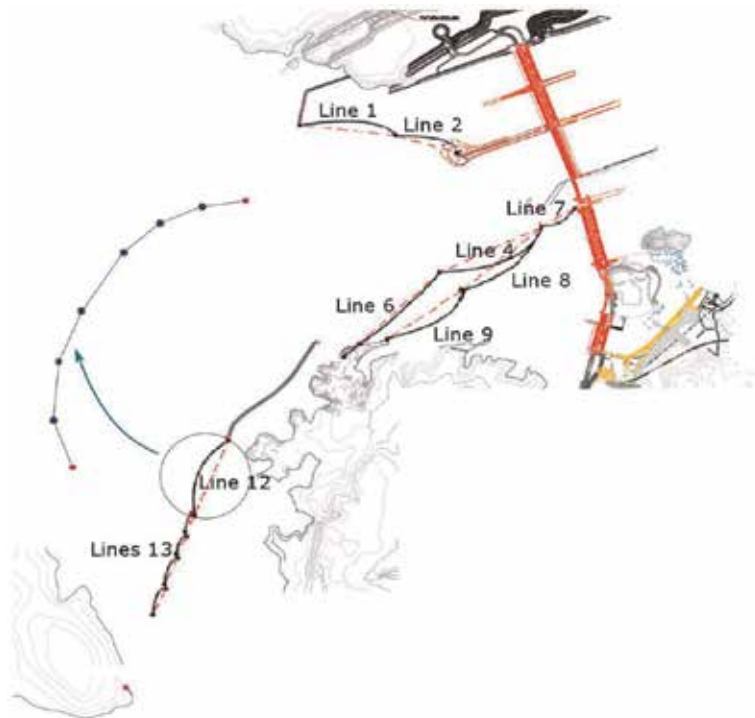
Figure 2.
Log boom lines and example of assembly of trusses used to model them.

difficulties were generally not justified by the potential increase in accuracy, as the tool would eventually be integrated in a larger numerical simulator.

2. Numerical model

The mathematical model used in the present formulation is based on the works of Felippa and Gavin [2–4], whereas the numerical implementation was developed within the Matrix Laboratory (MATLAB) environment [5]. The material deformations are assumed elastic only (i.e., no plasticity or yielding) as each log boom is

mainly composed of steel, making the unit respond linearly until approximately 80% of the yield stress [6], but the displacements are geometrically nonlinear, as the forces, the geometric stiffness, and the assembly equilibrium configuration depend on one another.

2.1 Mathematical model

Consider the three-dimensional truss element composed by six degrees of freedom (DoF) that represent all the possible translation directions its nodes have. Such element is used to model the structural behavior of each log boom (**Figure 1**).

With this numbering, the element constitutive stiffness matrix $\mathbf{K_{Ee}}$ is

$$
K_{Ee} = \frac{E_e A_\phi}{L_0}
\begin{bmatrix}
1 & 0 & 0 & -1 & 0 & 0 \\
0 & 0 & 0 & 0 & 0 & 0 \\
0 & 0 & 0 & 0 & 0 & 0 \\
-1 & 0 & 0 & 1 & 0 & 0 \\
0 & 0 & 0 & 0 & 0 & 0 \\
0 & 0 & 0 & 0 & 0 & 0
\end{bmatrix}
\tag{1}
$$

while its geometric stiffness matrix $\mathbf{K_{Ge}}$ is

$$
K_{G_e} = \frac{T}{L_0}
\begin{bmatrix}
0 & 0 & 0 & 0 & 0 & 0 \\
0 & 1 & 0 & 0 & -1 & 0 \\
0 & 0 & 1 & 0 & 0 & -1 \\
0 & 0 & 0 & 0 & 0 & 0 \\
0 & -1 & 0 & 0 & 1 & 0 \\
0 & 0 & -1 & 0 & 0 & 1
\end{bmatrix}
\tag{2}
$$

These matrices represent the stiffness of the truss due to its constitutiveness (as $\mathbf{K_{Ee}}$ depends on the stiffness module $\mathbf{E_e}$, on the cross-sectional area $\mathbf{A_\phi}$, and on the undeformed length $\mathbf{L_0}$) and existence of external influence (counterbalanced by the tension $\mathbf{T}$). Consequently, the tangential element matrix $\mathbf{K_{Te}}$, defined as the overall stiffness, is simply their sum:

$$
K_{Te} = K_{Ee} + K_{Ge}
\tag{3}
$$

An assembly is then modeled by the joint of $\mathbf{N}$ trusses, representing its $\mathbf{N}$ log booms, as in **Figure 2**; thus, to account for the assembly overall stiffness $\mathbf{K_T}$, each $\mathbf{K_{Te}}$ is linearly transformed from the truss local coordinate systems to the global assembly counterpart, and they are later superimposed.

Now, considering a function $\mathbf{g(u)}$ that represents the unbalance between internal and external forces ($\mathbf{F}$ and $\mathbf{R}$, respectively), for a given geometric configuration $\mathbf{u}$, there is a relation between $\mathbf{g(u)}$ and $\mathbf{K_T}$:

$$
g(u) \equiv R - F = K_T \Delta u
\tag{4}
$$

The equilibrium configuration $\mathbf{u}^*$ is achieved when $\mathbf{g(u)}=\mathbf{0}$, and in order to find it, $\mathbf{g(u^*)}$ can be expanded into a Taylor series about an arbitrary initial configuration $\mathbf{u^j}$:

$$g(u^*) = g(u^j) + \frac{dg(u)}{du}\bigg|_{u=u^j}(u^* - u^j) + \frac{1}{2}\frac{d^2\,g(u)}{du^2}\bigg|_{u=u^j}(u^* - u^j)^2 + O(u^3) = 0$$

(5)

Truncating Eq. (5) to the first order, $\mathbf{u}^*$ can be approximated by the unbalance and its first derivative:

$$u^* \approx u^j - \left(\frac{d\,g(u)}{du}\bigg|_{u=u^j}\right)^{-1}g(u^j)$$

(6)

which, however, is a linear approximation of this nonlinear formulation. Given such nonlinearity, the problem must be solved numerically, and all the equations presented insofar are part of an iterative scheme, in which $\mathbf{j}$ ($\mathbf{j=0, 1, ...}$) is the $\mathbf{j^{th}}$ iteration. Therefore, numerically speaking, successive expansions must be taken about the consecutive values of $\mathbf{u}$ until a satisfactory equilibrium $\mathbf{u^{*\,Num}}$ is achieved within a specified tolerance. So, from Eq. (6), at each iteration an improved equilibrium configuration $\mathbf{u^{j+1}}$ is obtained. Also, rearranging Eq. (4) in terms of the same improved equilibrium configuration, one obtains:

$$u^{j+1} = u^j - \left[K_T^j\right]^{-1}\left(R^j - F^j\right)$$

(7)

As expected, by similarity, $\mathbf{K_T^j} = \frac{\mathbf{d\,g(u)}}{\mathbf{du}}\big|_{\mathbf{u=u^j}}$, i.e., the tangential matrix is a function of $\mathbf{u^j}$. So, the numerical method consists of starting from an initial geometry, calculating the external and internal forces, calculating the assembly tangential matrix, and updating the geometric configuration. This process is repeated until the internal and external forces are sufficiently close.

2.2 Force calculations

The loads acting on the assembly originate from the hydrodynamic interaction and from the log accumulation and must be counterbalanced by the internal forces, which are a function of the mechanical properties of the material. Although the formulation is tridimensional, for the purposes by which the model was made, it is sufficient to obtain the equilibrium configuration on the XZ plane. Hence, the calculations presented next will only be on this plane.

2.2.1 External loads

To estimate the external forces, a database was created with the aid of computational fluid dynamics (CFD) (**Figure 3**). The software Siemens Star-CCM+, version 12.02.011, was used for these numerical simulations: both water and air were admitted incompressible, and the flow field was modeled using the unsteady Reynolds-averaged Navier-Stokes equations implicitly (at the first iterations, the movements were frozen to ensure fluid stabilization and then gradually released, still seeking stabilization); the interaction between the fluids was represented by the volume of fluid Eulerian multiphase model, and the multiphase conditions were defined by the flat wave model with a numerical damping, added in the momentum equation on the vertical direction, on both the inlet and outlet boundary conditions to minimize the effects of reflection and ensure better convergence; finally, the k-ω SST model was adopted.
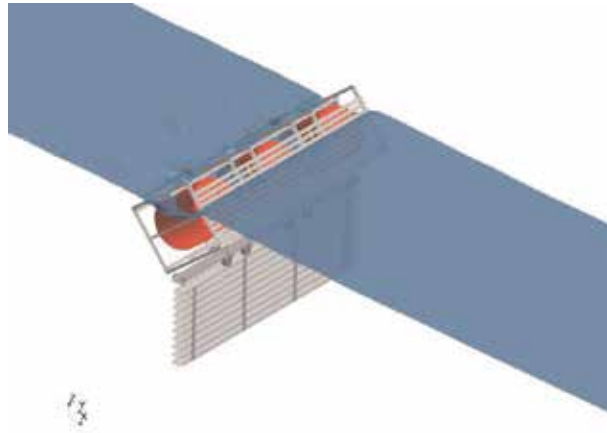
Figure 3.
CFD domain used to obtain the external force database.
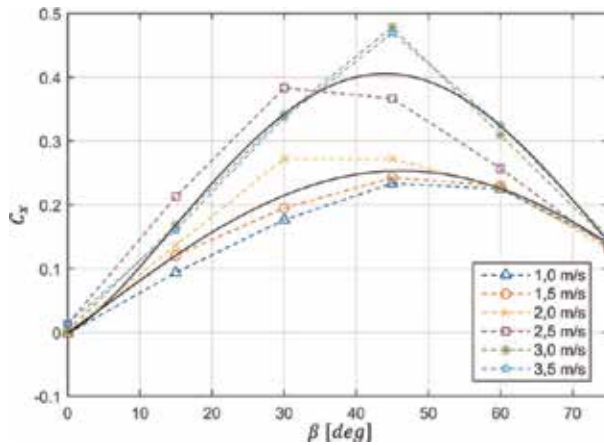
Figure 4.
Example of C_x and C_z coefficients as functions of the velocity magnitude and incidence angle.

A series of velocity magnitudes **V** and incidence angles **β** were simulated such that normal and tangential coefficients (**C_z** and **C_x**, respectively) were calculated [7–9]. From them, fitting curves in the form of Eq. (8) were adjusted, whose values of **K** depend on **V** (**Figure 4**):

$$C_x = K_{1x} \cos{(K_{2x}\beta)}^{K_{3x}}$$
$$C_z = K_{1z} \text{sen}(K_{2z}\beta)^{K_{3z}} \qquad (8)$$

Each part of the log boom that is free to rotate was assigned with a pair of coefficients (i.e., the grids and the chassis) such that the total hydrodynamic force acting on the trusses is retrieved based on them. So, for the **i^{th}** log boom (**$i = 1, ..., N$**),

$$R_{xi}(V_i, \beta_i) = \frac{1}{2}\rho V_i^2(C_{cxi}A_{CN} + C_{Gxi}A_{GN})$$
$$R_{zi}(V_i, \beta_i) = \frac{1}{2}\rho V_i^2(C_{czi}A_{CN} + C_{Gzi}A_{GN}) \qquad (9)$$
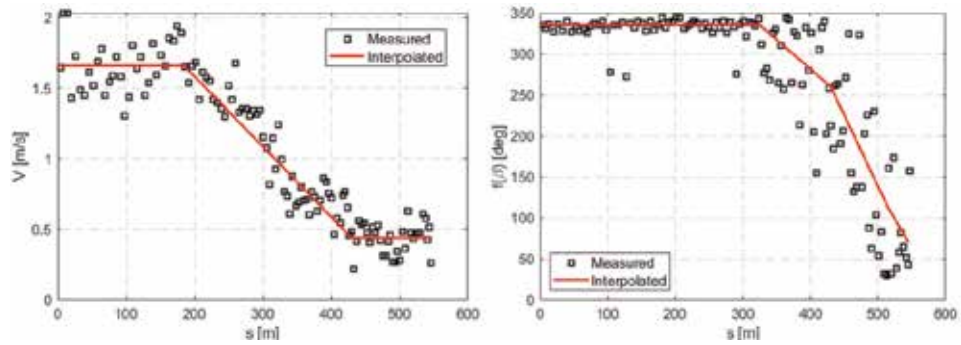
Figure 5.
Example of the variation of the velocity magnitude and incidence angle along a projected line that connects the mooring points. The angles are measured taking the north coordinate of reference; thus, it is not β itself, but a function of it.

$\mathbf{A_{CN}}$ and $\mathbf{A_{GN}}$ are the chassis and grid front areas, and $\boldsymbol{\rho}$ is the water density. The $\mathbf{V}$ and $\boldsymbol{\beta}$ combinations used in the simulations were arithmetically averaged from velocimetry data measured in situ along a line $\mathbf{s}$ that connects the assemblies' mooring points (**Figure 5**).

Once the hydrodynamic coefficients were obtained, the contribution from the logs that accumulate along the lines was assumed to be increments on the normal coefficients [10] and estimated with the aid of data from experiments at the towing tank of the IPT (**Figure 6**). Thus, considering already such increments, Eq. (9) accounts for the total external forces acting on the center of the element, which are equally distributed to its nodes and further transformed from local to global coordinates as well, according to the angle $\boldsymbol{\theta_i}$ between the two reference frames:

$$R_{Xi} = -R_{zi}\ \sin(\theta_i) + R_{xi}\ \cos(\theta_i)$$
$$R_{Zi} =\ \ R_{zi}\ \cos(\theta_i) + R_{xi}\ \sin(\theta_i)$$

$$(10)$$

So, $\mathbf{R_{Xi}/2}$ and $\mathbf{R_{Zi}/2}$ act on the $\mathbf{X}$ and $\mathbf{Z}$ directions of each node element.

2.2.2 Internal loads

The tension distribution throughout the trusses is calculated based on classic linear relations of solid mechanics, and it acts on the axial direction of the element.

Figure 6.
Example of experiment to measure the influence of the logs on the assembly.

Therefore, for the same $\mathbf{i^{th}}$ log boom, stretched to a new length $\mathbf{L_i}$ (thus having new coordinates $\mathbf{u_i}$), the internal tension acting upon it is calculated as in Eq. (11):

$$T_i = EA_\phi \left(\frac{L_i - L_0}{L_0} \right) \tag{11}$$

This tension must be transformed to internal forces $\mathbf{F_i}$ that act on the nodes and are represented on the global coordinate system. Considering the same angle $\mathbf{\theta_i}$, the internal forces are obtained through a similar transformation:

$$\begin{aligned} F_{Xi} &= T_i \cos(\theta_i) \\ F_{Zi} &= T_i \, \sin(\theta_i) \end{aligned} \tag{12}$$

2.3 Initial condition

Originally, the solution strategy was to adopt the line completely stretched along the $\mathbf{X}$ direction and then gradually move the leftmost mooring point by small increments $\vec{\mathbf{\Delta^j}}$ toward its final location, while the rightmost mooring point would start at its correct location. Then, at each $\vec{\mathbf{\Delta^j}}$ the iterative scheme was run until convergence (**Figure 7**).

However, such quasi-static approach is computationally expensive because of the repetitiveness of the iterative procedure. Additionally, $\vec{\mathbf{\Delta^j}}$ has to be carefully chosen to avoid numerical divergence. Thus, an improved initial condition was proposed in which the assembly was initially approximated by a catenary whose "weight vector" was obtained from the average of the hydrodynamic forces along $\mathbf{s}$ (**Figure 8**). Then, with the initial geometry determined, the external and internal forces could be calculated based on node equilibrium (**Figure 9**), as in Eq. (13):

$$\vec{T}_{i-1} + \vec{T}_i + \frac{\vec{R}_{i-1} + \vec{R}_i}{2} = \vec{0} \tag{13}$$

in which $\vec{R}_i = R_{iX}\hat{X} + R_{iZ}\hat{Z}$ and $\vec{T}_{i-1}$ and $\vec{T}_i$ are not known a priori (note that there is no "element 0," but $\vec{T}_0 = \vec{T}_1$); thus, a recursive scheme starting from one of
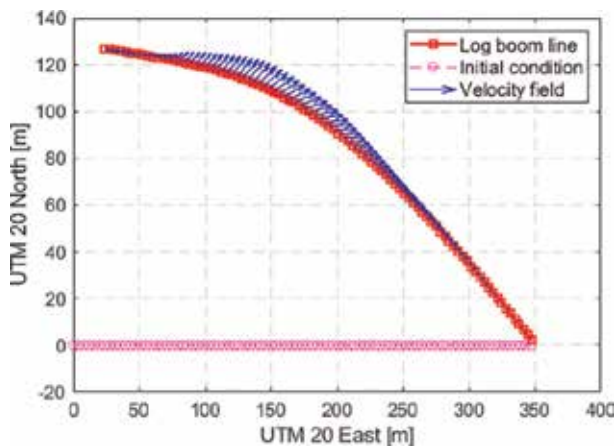
Figure 7.
Example of initial condition and its evolution until final convergence.
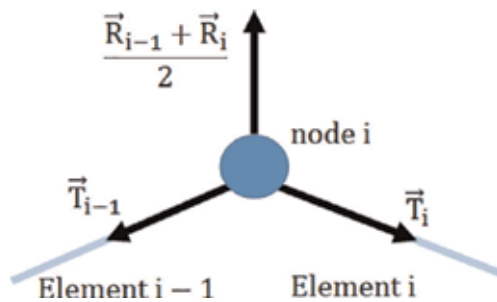
Figure 8.
Schematics of the new initial condition to obtain the tension distribution throughout the elements.
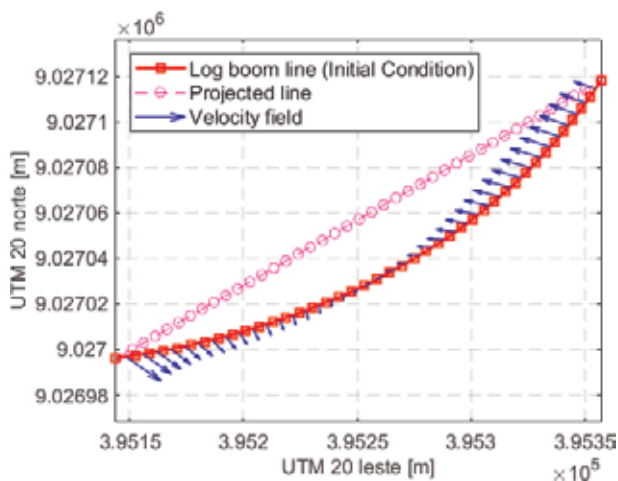
Figure 9.
Example of improved initial condition (catenary shape).

the mooring points is performed, as (13) has only one unknown at any of these locations. The internal forces are then calculated using Eq. (12), and the iterative scheme starts by either stretching the geometry by a small amount $\vec{\delta}$ from the catenary geometry or, equivalently, by creating a small unbalance $\mathbf{g}$.

2.4 Static condensation

An intrinsic characteristic of structural problems is the presence of fixed degrees of freedom (F) in addition to the free ones (L). Thus, a common practice in FEM, known as static condensation, is to renumber the DoF seeking to reorder and split the linear system into two sub-systems. So, the displacement array can be written as:

$$\Delta u = \left\{ \begin{array}{c} \Delta u_L \\ \Delta u_F \end{array} \right\} \tag{14}$$

and the unbalance array can be similarly split:

$$g(u) = \left\{ \begin{array}{c} g(u_L) \\ g(u_F) \end{array} \right\} \tag{15}$$

For the log boom assembly, the fixed DoF are related to the mooring points, so $\Delta \mathbf{u_F}$ are their known displacements, and $\mathbf{g(u_F)}$ are the unknown reaction forces, whereas the free DoF are related to the unknown displacement of the rest of the line; $\Delta \mathbf{u_L}$ and $\mathbf{g(u_L)}$ are the known difference between the external hydrodynamic and internal loads. Thus, the linear system (Eq. (4)) can be rewritten as:

$$\left\{ \begin{array}{c} \Delta u_L \\ \Delta u_F \end{array} \right\}^j = -\left[K_T^j \right]^{-1} \left\{ \begin{array}{c} g(u_L) \\ g(u_F) \end{array} \right\}^j \tag{16}$$

Additionally, the matrix $\mathbf{K_T}$ can be interpreted as follows:

$$K_T = \begin{bmatrix} K_{LL} & K_{LF} \\ K_{FL} & K_{FF} \end{bmatrix} \tag{17}$$

Thus, from Eq. (4),

$$\begin{cases} K_{LL}^j \Delta u_L^j + K_{LF} \Delta u_F^j = g(u^j)_L \\ K_{FL}^j \Delta u_L^j + K_{FF}^j \Delta u_F^j = g(u^j)_F \end{cases} \tag{18}$$

These sub-systems are solved recursively: the first of Eq. (18) is solved for $\Delta \mathbf{u_L^j}$ and, sequentially, the reaction forces as calculated from the second one. Moreover, static condensation is needed regardless of the initial condition used.

2.5 Sub-relaxation

Several times, the initial condition itself is not sufficient to ensure convergence because the average velocity used to calculate the catenary "weight" might not create a representative starting geometry. So, whenever the direct method fails, a sub-relaxation parameter is applied to the force unbalance as a way to prevent large deflections through the line, which is especially interesting during the first iterations; the restrained deflections are generally sufficient to adequately converge the simulation. The sub-relaxation $\mathbf{\Omega}$, $\mathbf{0 < \Omega \leq 1}$ is applied in the updating process of $\mathbf{g(u)}$ such that

$$g(u^j) = g(u^{j-1}) + \Omega^j (R^j - F^j) \tag{19}$$

$\mathbf{\Omega}$ is usually a function of the iteration, but it must necessarily achieve unity prior to final convergence. An example of how this parameter varies with the iteration is shown in **Figure 10**.

2.6 Post-processing

After numerical convergence, a series of variables can be outputted, such as the final geometry, the velocity magnitude and incidence angle acting over each log boom, the reaction forces, and the tension distribution along the length of the line $\mathbf{L_A}$. These variables, especially the last one, are of great importance, once they help predict whether or not the simulated condition threatens the integrity of the line. Examples of converged line and tension distribution are presented on **Figures 11** and **12**.
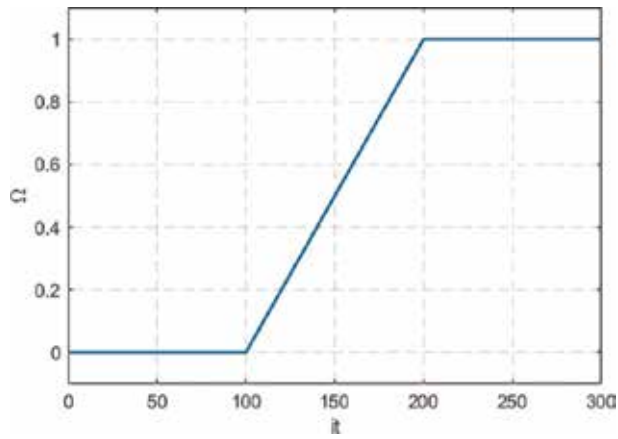
Figure 10.
Example of Ω behavior as a function of the iteration.
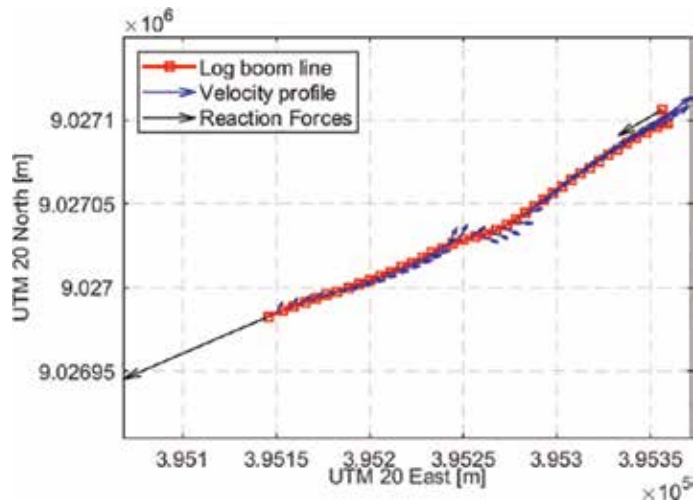
Figure 11.
Example of configuration after convergence, evidencing the final geometry, the velocity profile, and the reaction forces.
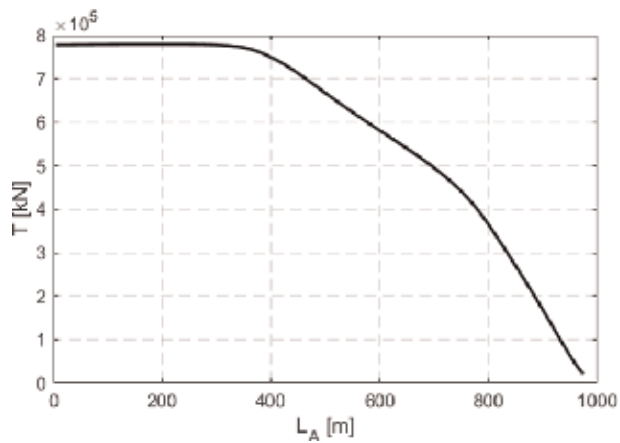
Figure 12.
Example of tension distribution along the assembly length L_A.

3. Results

In order to verify and validate the tool, thus assessing the numerical method developed, many simulations were compared to theoretical, experimental, and numerical data. As the ASME Verification & Validation Committee defines [11], validation determines the degree of accuracy that a numerical model has in representing the real world from its perspective, whereas verification evaluates its intrinsic errors and uncertainties. So, the committee states that verification precedes validation, as they must be performed to ensure the numerical reliability of the solution. In this work code and solution verifications were done by systematically refining the discretization and comparing the outputs with theoretical data from the problem of a catenary [12]. Following, the validation was done for two major cases: by comparing the solution with experimental results from a 1:10 scale model tested in the towing tank at the Naval and Ocean Engineering Laboratory of the IPT [13] and by comparing the solution with numerical simulations from SIMPACK® Multi-Body Simulation software in prototype scale [12, 14]; the later comparison had to be done against numerical data because it was unfeasible to instrument the in situ assemblies. Additionally, only hydrodynamic cases (i.e., without logs) were compared.

3.1 Verification from a theoretical catenary model

While evaluation of the error was performed through comparison with the catenary model, estimation of the error was done through classical Richardson extrapolation [12]. Code and solution verifications were performed by systematic grid refinement, with the coarsest mesh having 100 elements, the finest 800, and in between these two, successive meshes were created such that the number of trusses was consecutively increased by a value of approximately $\sqrt{2}$, as recommended by the committee [11]. For the analysis, a refinement ratio **r** that is a dimensionless form of representing the number of elements was defined:

$$r = \frac{h_N}{h_{N_{Max}}} \tag{20}$$

h_N is a representative grid size that, for the present formulation, assumes the form of Eq. (21):

$$h_N = \frac{\sum_{i=1}^{N} L_0}{N} = L_0 \tag{21}$$

Thus, according to Eq. (20), **r=1** represents the finest grid and **r=0** an extrapolation in which the number of elements would hypothetically tend to infinity, as their length would decrease accordingly. In the convergence region, the behavior of the solution takes the form of Eq. (23), in which **f_{ext}** is the extrapolated value, **p** the order of convergence, and **C** a constant to be determined. From this expression, a fitting curve is plotted against **r** for the assessment of the convergence behavior:

$$f(h_N) = f_{ext} + Ch_N^p \tag{22}$$

The relative error is simply evaluated by calculating the difference between the theoretical and numerical values:

$$E_r = \frac{|f_{ext} - f(h_N)|}{|f_{ext}|} \tag{23}$$

and the uncertainty **σ** estimated through a grid convergence index (GCI):

$$GCI = \frac{F_S |f(h_{N_{Max}}) - f(h_{(N_{Max}-1)})|}{\left[\frac{h_{N_{Max}}}{h_{(N_{Max}-1)}}\right]^P - 1} \tag{24}$$

$$\sigma = \frac{GCI}{\psi \times f_{ext}} \tag{25}$$

F$_S$ and **ψ** are assigned, 1.25 and 1.1, respectively, so a safe value for **σ** is estimated. The catenary used for verification has a total length of **L$_C$ = 200 m**, and the mooring points are at $(0, 200)$ and $(10, 20)$. A vertical force per unit length **F′ = 617.32 N/m** acts throughout, and the minimum and maximum forces over the catenary are used as variables of verification, **f(h$_N$)**; they are both functions of the curve parameter **a**, which in turn is obtained by solving a transcendental equation that depends on the geometric parameters and on the force distribution:

$$F_{min} = a \times F' \tag{26}$$

$$F_{max} = max\left\{\frac{l \times F'}{\sin\left[\tan^{-1}\left(\frac{l}{a}\right)\right]}\right\} \tag{27}$$

l is the length of a segment measured from one of the catenary vertices. **Figure 13** shows the trends of the numerical forces as a function of the refinement ratio along with the theoretical values, which are **F$_{min}$ ≈ 110.793 kN** and **F$_{min}$ ≈ 133.492 kN**. On both cases **p** is close to 1, i.e., a convergence accuracy of first order. Furthermore, the extrapolated values differ from the theoretical ones by no more than **0.2%**, and for the finest grid, the error is within the numerical uncertainty. Finally, all the values are close to the fitting curve, indicating that even for the poorest grids they seem to be within the convergence region: in fact, if the uncertainties remain of the same order regardless of the level of discretization, the disparity between the poorest grid and theoretical value is acceptable [12].

Finally, **Figure 14** shows a comparison between numerical and theoretical geometries; as they practically overlap, the verification corroborates the precision of the proposed model. As a note, in order not to be much close to the correct
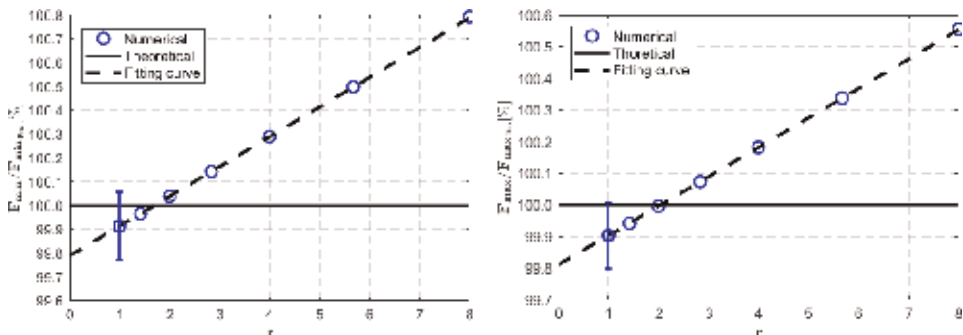
Figure 13.
Convergence of the numerical catenary maximum and minimum forces versus refinement ratio. Values are normalized by the theoretical ones.
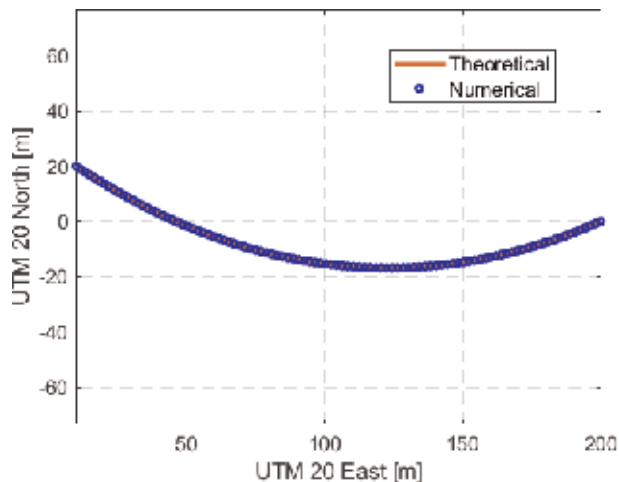
Figure 14.
Geometry comparison for the theoretical formulation and numerical method.

catenary geometry, the verification was conducted with the line completely stretched along the **X** direction.

3.2 Model scale validation

Reduced model experiments were conducted at the facilities of the IPT in a 1:10 scale with the purpose of studying the hydrodynamic behavior of such structures [13]. To do so, the model, developed mainly in polycarbonate and polymer, was constructed with the aid of a laser cutting machine and a 3D printer; the assembly was ballasted by adding lead stripes along the structure but without changing its front area as to minimize drag interference; to test both symmetric and asymmetric setups, log booms were added from a five-unit symmetric configuration, while the left mooring point was offset by distances **ΔZ** along the flow direction, since the model width was limited by the basin; flat plates were attached on both extremities to reduce the interference of the structures and to better control the flow incidence.

Four S-Type S9M uniaxial load cells, produced by HBM, were used at each extremity, each of which with a nominal measure limit of 500 N, so the tensile forces acting on the leftmost and rightmost log booms could be acquired. Additionally, to understand how the stain behaves on each log boom and also how it is transferred throughout the structure, water strain gages, manufactured by Kyowa Electronic Instruments, were placed on one of the modules, as shown schematically in **Figure 15**. These locations were appropriately chosen with the aid of numerical simulations from finite element method: the criterion was to locate the stress concentration area that increased the measurement sensitivity while avoided the high strain gradients, since the latter can contribute to unreliable measurements.

Figures 16–18 compare experimental and numerical results for three different configurations as the function of the velocity. "LE" indicates "left extremity" and "RE" "right extremity," while "Exp" and "Num" refer to experimental and numerical values. No numerical uncertainty was provided since the number of trusses was maintained equal the number of log booms.

The results agree satisfactorily: the differences are more evident as the free stream velocity increases; the numerical method reproduces the experimental observation that the tensile force is larger at the leftmost log boom, an expected trend since tensile loads are higher for elements that are parallel to the stream; the
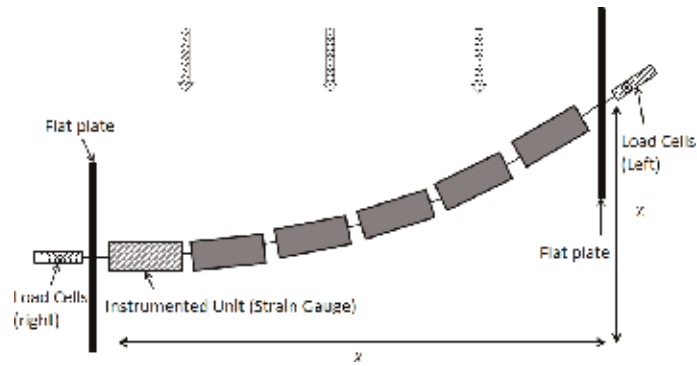
Figure 15.
Schematics of the experimental setup.
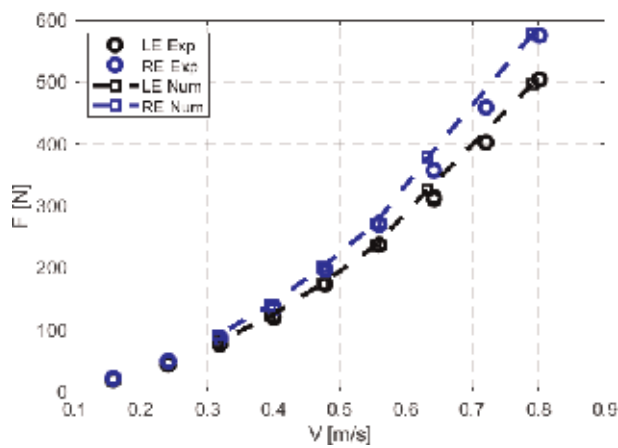
Figure 16.
Force comparison as a function of free stream velocity. Six log boom lines.
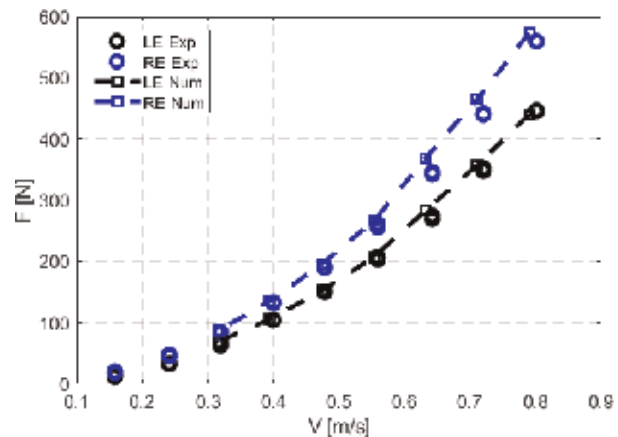
Figure 17.
Force comparison as a function of free stream velocity. Seven log boom lines.

number of log booms seems not to affect the accuracy of the results, as the error remains practically the same regardless of the configuration; the larger differences are within **6**.0% and are possibly due to reasons such as the model material properties, the modeling of the external forces, and the few number of elements. For the
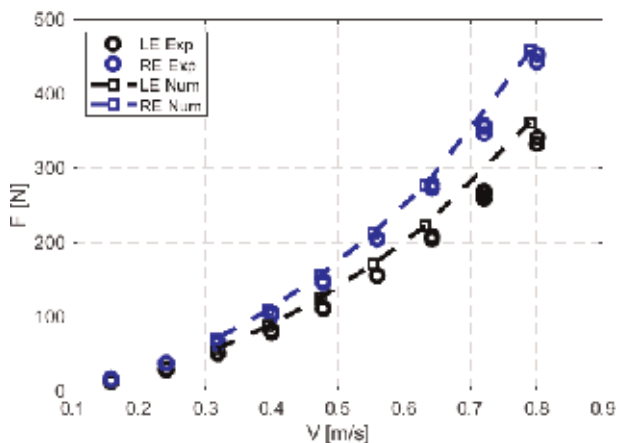
Figure 18.
Force comparison as a function of free stream velocity. Eight log boom lines.

later reason, better agreement could result from finer grids, although the one-to-one representation would be lost.

3.3 Prototype-scale validation

A prototype-scale validation is presented, and the results were compared to simulations from SIMPACK® Multi-Body Simulation software. The variables of comparison are again the reaction forces at the leftmost and rightmost anchor points, and the relative differences u_{LE} and u_{RE} use the values of SIMPACK® for normalization. In the following tables, SP refers to the results from SIMPACK®, while FEM to the results from the current method. Three validation cases were performed: line 02, line 12, and the set of line 13.

3.3.1 Line 02

The first prototype validation was performed for line 02 with a variable velocity profile, similar to the one presented in **Figure 5**. An example of converged solution for line 02 is presented in **Figure 19**, in which the equilibrium configuration, projected line, and velocity distribution are depicted.

The results from SIMPACK® and the current method are presented in [14]: the first simulation considers a 20% increase in the normal external force (C_z), while the second a 50% increase.

Table 1 shows that the maximum relative difference for the simulations that happen at the **RE** (approximately 7.6%), while for the **LE** the maximum difference is about 5.3%. Such values are satisfactory given the simplicity of the tool, in comparison to SIMPACK®.

SP (kN)		FEM (kN)		u (%)	
LE	RE	LE	RE	LE	RE
1025	814	1076	876	5.0	7.6
1239	1029	1305	1104	5.3	7.3

Table 1.
Comparison of results between SIMPACK® and the current method—Line 02.

3.3.2 Line 12

The second validation was performed for line 12 with several velocity profiles, also similar to the one presented in **Figure 5**. Analogously, **Figures 19** and **20** depict an example of a converged solution.

Table 2 presents the comparison between SIMPACK® and the developed formulation. For this set of simulations, the maximum percentage difference happens at the **LE**, and its value is approximately 6.6%, while at the **RE** this difference is about 5.2%; the values are comparable to those for line 02, except that the extremities at which the maximum occurs are swapped.

3.3.3 Lines 13

The last validation was conducted for the group of lines 13, i.e., for lines 13A, 13B, 13C, and 13D. **Figure 21** is an example of a converged simulation for line 13C/13D.
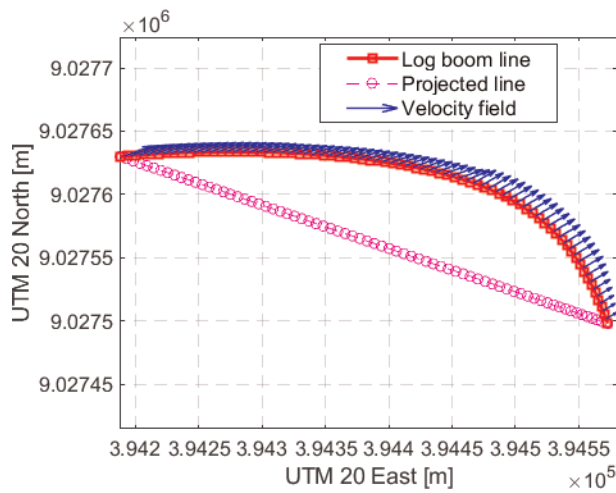
Figure 19.
Example of converged simulation for line 02.
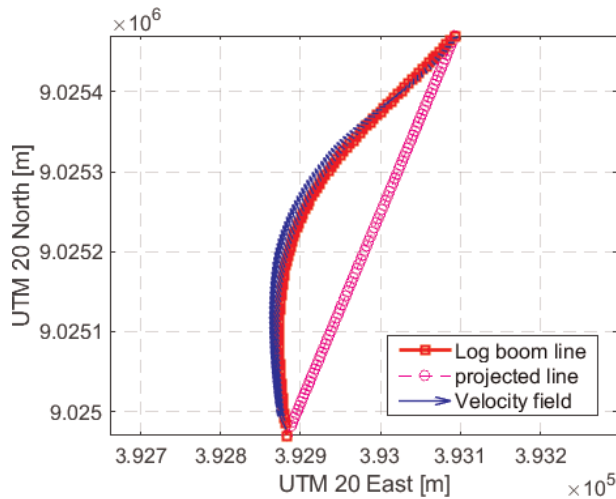
Figure 20.
Example of converged solution for line 12.

SP (kN)		FEM (kN)		u (%)	
LE	RE	LE	RE	LE	RE
1566	1234	1666	1295	6.4	4.9
1540	1204	1641	1267	6.6	5.2
1866	1479	1983	1543	6.3	4.3
2028	1578	2158	1659	6.4	5.2
1463	1124	1559	1181	6.6	5.1
1793	1387	1910	1459	6.5	5.2
1946	1487	2071	1564	6.4	5.2
1789	1382	1905	1454	6.5	5.2
1767	1359	1877	1424	6.2	4.8
1710	1306	1821	1374	6.5	5.2
2255	1748	2405	1840	6.6	5.3
1701	1314	1811	1381	6.4	5.1
1820	1414	1888	1425	3.7	0.8

Table 2.
Comparison of results between SIMPACK® and the current method—Line 12.
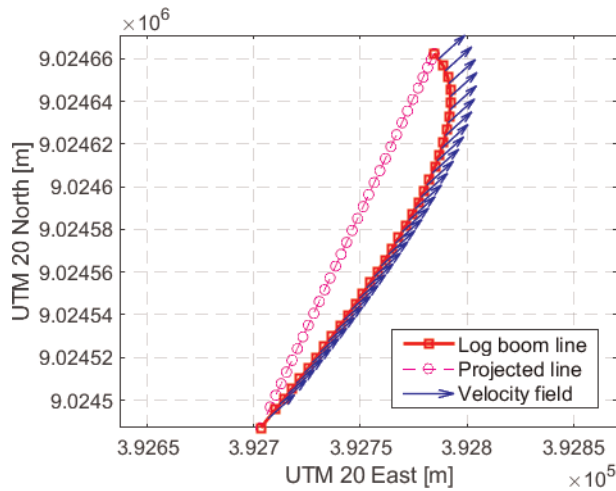
Figure 21.
Example of converged solution for line 13C/13D.

Particularly for line 13, the magnitude and incidence angle remained constant throughout them, varying from simulation to simulation. In **Table 3** these parameters are summarized: the first columns indicate the velocity range (VR) used in each simulation for the choice of the coefficients of Eq. (8), even though the actual velocity magnitude was sometimes not within that range.

Table 4 presents the comparison between SIMPACK® and the developed formulation.

The maximum percentage difference of the simulations happens again at the **LE** and is approximately 7.0% for line 13A/13B and 7.1% for line 13C/13D. At the **RE**, the difference is about 5.5% for line 13A/13B and 6.3% for line 13C/13D.

	Line 13A/13B		Line 13C/13D	
VR (m/s)	V (m/s)	Angle (°)	V (m/s)	Angle (°)
2.5 < V < 3.5	3.18	54.44	2.11	59.60
2.5 < V < 3.5	2.49	54.81	2.04	42.00
1.0 < V < 3.5	2.14	52.11	1.60	56.26
1.0 < V < 3.5	1.80	49.56	1.33	42.48
1.0 < V < 2.0	1.69	53.06	1.13	61.03
1.0 < V < 2.0	1.36	52.80	1.05	43.53

Table 3.
Parameters for simulations of lines 13.

Line 13A/13B						Line 13C/13D					
SP (kN)		FEM (kN)		u (%)		SP (kN)		FEM (kN)		u (%)	
LE	RE	LE	RE	u_{LE}	u_{RE}	LE	RE	LE	RE	u_{LE}	u_{RE}
1550	1263	1655	1329	6.8	5.2	822	647	876	679	6.6	5.0
934	759	1000	801	7.0	5.5	1501	1318	1607	1401	7.1	6.3
745	618	793	650	6.5	5.2	537	436	572	458	6.5	5.1
577	486	615	512	6.7	5.5	600	525	639	556	6.6	5.9
429	358	455	376	6.0	5.2	209	165	221	173	5.8	4.7
280	234	297	247	6.2	5.4	341	301	361	318	6.0	5.5

Table 4.
Comparison of results between SIMPACK® and the current method—Lines 13.

4. Conclusions

A simple truss-based finite element method was proposed to simulate the load distributions and geometric configurations of assemblies that behave in a catenary-like manner, subject to external, variable loads. The formulation was tailored to the particular problem of log booms (structures that retain logs from reaching the machinery of hydropower plants) under the influence of river streams and the logs they convey. The nonlinear formulation imposes equilibrium between internal and external forces so that an iterative scheme must be numerically solved. The method was verified by comparison against analytical results from a theoretical catenary model: the relative error and uncertainty for the maximum and minimum forces were within 0.2%, while the mesh refinement order of convergence was close to 1. The tool was later validated against experimental model-scale data from the towing tank at the Institute for Technological Research [12] and prototype-scale numerical data from commercial software SIMPACK®, and all the results agree adequately [14]: for the experimental data validation, the numerical method was capable of reproducing the observations of the experiments, and the maximum relative discrepancy observed was about 6%. The differences are invariant to the increase in the assembly length, but they seem sensible to variations of the free stream. Likewise, the prototype-scale validations all show adequate agreement, regardless of the line configurations, and a maximum relative error, considering SIMPACK® as the reference, of less than 8%. These percentages corroborate the adequacy of the method for the purpose by which it was developed: to a have a fast, yet reliable,

tool, to forecast the tension distributions throughout the lines such that it can be used as a simulator for the assessment of the structural safety of log boom assemblies.

Acknowledgements

Author details

Jose Rodolfo Chreim* and Joao Lucas Dozzi Dantas
Institute for Technological Research, Sao Paulo, Brazil

*Address all correspondence to: jrchreim@outlook.com

IntechOpen

References

[1] The Ocean Cleanup. The Ocean Cleanup Technology; 2019. Accessed date: 12/Apr/2018. Available from: https://theoceancleanup.com/technology/

[2] Felippa CA. Introduction to Finite Element Methods. Boulder: Department of Aerospace Engineering Sciences, University of Colorado; 2004

[3] Gavin H. Geometric Stiffness Effects in 2D and 3D Frames. Department of Civil and Environment Engineering, Edmund T. Pratt School of Engineering, Duke University; 2012. Accessed date: 12/Apr/2018. Available from: http://people.duke.edu/~hpgavin/cee421/frame-finite-def.pdf

[4] Neto AG, Correia RP. Ambiente de análise de risers em águas ultraprofundas: Análise estática, pré e pós-processador [Undegratuate degree thesis]. São Paulo, Brazil: Universidade de São Paulo; 2006

[5] Castro F, Katsuno E, Dantas J. Instrumentation methodology for a log containment grid model in towing tank tests. In: The 30th American Towing Tank Conference; The Society of Naval Architects and Marine Engineers; 2017

[6] Ferreira AJ. MATLAB Codes for Finite Element Analysis: Solids and Structures. Vol. 157. Netherlands: Springer Science & Business Media; 2008

[7] Katsuno ET, de Castro FS, Dantas JLD. Hydrodynamic analysis of debris containment grids in hydropower plant using porous media. In: 24th ABCM International Congress of Mechanical Engineering (COBEM 2017); ABCM - Associacao Brasileira de Engenharia e Ciencias Mecanicas; 2017

[8] Katsuno ET, de Castro FS, Dantas JLD. Debris containment grid CFD validation with towing tank tests. In: The 30th American Towing Tank Conference; The Society of Naval Architects and Marine Engineers; 2017

[9] Katsuno ET, de Castro FS, Assi GRS, Dantas JLD. Numerical analysis of debris containment grid fluid-body interaction. In: ASME 2018 37th International Conference on Ocean, Offshore and Arctic Engineering; American Society of Mechanical Engineers; 2018

[10] de Castro FS, Katsuno ET, Assi GRS, Dantas JLD. Structural investigation of the log accumulation in a debris containment grid through towing tank experiments. In: ASME 2018 37th International Conference on Ocean, Offshore and Arctic Engineering; American Society of Mechanical Engineers; 2018

[11] V&V20 Committee et al. Standard for Verification and Validation in Computational Fluid Dynamics and Heat Transfer. New York: The American Society of Mechanical Engineers; 2009

[12] Chreim JR, Dantas JLD, Lima AA. Nonlinear truss-based quasi-static structural model for force distribution predictions on debris containment grids. In: ASME 2018 37th International Conference on Ocean, Offshore and Arctic Engineering; American Society of Mechanical Engineers; 2018

[13] de Castro FS, Katsuno ET, de Souza JMP, Kogishi AM, Dantas JLD. Structural analysis for a reduced scale model of a hydropower plant debris containment grid. In: 24th ABCM International Congress of Mechanical Engineering (COBEM 2017); ABCM – Associacao Brasileira de Engenharia e Ciencias Mecanicas; 2017

[14] Chreim JR, Lima BM, Dantas JLD. Validation of a simple dynamical structural model for hydrodynamic loads. In: 27th International Congress on Waterborne Transportation, Shipbuilding, and Offshore Constructions; 2018

Design Optimization of 3D Steel Frameworks Under Constraints of Natural Frequencies of Vibration

Cláudio H.B. Resende, José P.G. Carvalho,
Afonso C.C. Lemonge and Patricia H. Hallak

Abstract

Steel multistorey 3D frames are commonly used in business and residential buildings, industrial sheds, warehouses, etc. The design optimization of tall steel buildings is usually governed by horizontal loadings, such as, wind load, as well as its dynamic behavior, for which the structure must have the stiffness and stability in accordance with the safety criteria established by codes. This chapter deals with sizing structural optimization problems, concerning weight minimization of 3D steel frames, considering natural frequencies of vibration as well as allowable displacements as the constraints of the optimization problem. The discrete design variables are to be chosen from commercial profiles tables. A differential evolution (DE) is the search algorithm adopted coupled to an adaptive penalty method (APM) to handle the constraints. Three different 3D frames are optimized, presenting very interesting results.

Keywords: steel frame optimization, differential evolution, natural frequencies of vibration, wind load, adaptive penalty method

1. Introduction

Steel multistorey 3D frames are commonly used in business and residential buildings, industrial sheds, warehouses, etc. The design optimization of tall steel buildings is usually governed by horizontal loadings, such as, wind load, as well as its dynamic behavior, for which the structure must have the stiffness and stability following the safety criteria established by codes. The task of finding the most economical structures, that is, with the minimum weight and satisfying the constraints imposed by the codes, such as, ASD-AISC [1], NBR 6123 [2], and NBR 8800 [3], is not trivial. This may require an interactive process (trial and error) that may require very expensive or even impossible computational time. The behavior constraints include, for instance, combined bending and axial stress, shear stress, compression buckling, tension slenderness, drift ratio, multiple natural frequencies of vibration, elastic critical loads, etc.

This chapter is not an attempt to provide a survey of publications on structural optimization problems of multistorey 3D frames concerning many types of constraints. However, one can cite some papers where readers can find reviews regarding this issue.

An optimization process via genetic algorithms using MATLAB-SAP2000 Open Application Programming Interface (OAPI) is presented for optimum design of space frames with semirigid connections in Artar and Daloğlu [4].

An enhanced imperialist competitive algorithm for optimum design of skeletal structures is proposed by Maheri and Talezadeh [5]. In Aydoğdu et al. [6], an enhanced artificial bee colony algorithm is adopted to find the optimum design problem of steel space frames formulated according to the provisions of LRFD-AISC. Talatahari et al. [7] proposed the combination of an eagle strategy algorithm with the differential evolution (DE) which is implemented by interfacing SAP2000 structural analysis code and MATLAB mathematical software to find the optimum design of framed structures. Maheri et al. [8] proposed an enhanced honey bee mating optimization algorithm for the design of side sway steel frames. The robustness of the algorithm in terms of both solution quality and computational cost is proven by solving four design optimization problems of side sway steel frames. Optimal seismic design of three-dimensional steel frames is carried out in Kaveh and BolandGerami [9] with the structures subjected to gravity and earthquake loadings and designed according to the LRFD-AISC design criteria.

The harmony search metaheuristic is used as the search engine. Kaveh and BolandGerami [9] used a cascade-enhanced colliding body optimization to find the optimum design of large-scale space steel frames according to ASD-AISC. Jalili et al. [10] presented a modified biogeography-based optimization (MBBO) algorithm for the optimum design of skeletal structures with discrete variables. Gholizadeh and Poorhoseini [11] proposed a modified dolphin echolocation (MDE) algorithm proposed for the optimization of steel frame structures. Gholizadeh and Milany [12] used an improved fireworks algorithm (IFWA) to deal with the discrete structural optimization problems of steel trusses and frames.

Since the tall buildings present the need for in-depth analyses regarding their lateral stability, several studies are found in the literature on this subject. Cost efficiencies of various steel frameworks are investigated for the economical design of multistorey buildings by Hasançebi [13]. Braced and unbraced steel frames subjected to gravity and lateral seismic loads were studied by Memari and Madhkan [14]. Kameshki and Saka [15] compared pin-jointed frames considering several types of bracings with rigidly connected frames without bracings. Liang et al. [16] applied a performance-based design optimization method to discover optimum topologies of bracings for steel frames. In his paper Hasançebi [13] highlights important aspects regarding restrictions on the fabrication of structural elements. In this sense, it is essential. In this sense, it is imperative that construction costs of the resulting structures, rather than design weights only, must be evaluated. Studies on this subject were conducted by Pavlovčič et al. [17].

This chapter deals with sizing structural optimization problems, concerning weight minimization of 3D steel frames, considering natural frequencies of vibration as well as allowable displacements as the constraints of the optimization problem. The discrete design variables are to be chosen from commercial profile tables. A DE [18] is the search algorithm adopted coupled with an adaptive penalty method (APM) to handle the constraints [19]. An essential aspect of this chapter is the importance that must be given concerning the constraints regarding the first natural frequency of vibration of the frames. Often, they are neglected in the formulations of these structural optimization problems. A brief review of optimization problems considering natural frequencies of vibration as constraints is provided by Carvalho et al. in [20].

This chapter is as organized as follows: Section 2 presents the formulation of the optimization problem. Section 3 presents the basics concepts on differential evolution algorithm and the strategy to handle the constraints. Numerical experiments

and analysis of results are described in Sections 4 and 5, respectively. Finally, the conclusions and extensions of this chapter are described in Section 6.

2. Formulation of the optimization problem

The optimization problem deals with the weight minimization of 3D steel frames consisting of N members, under constraint of natural frequencies of vibration and allowable displacements due to design loads.

The objective is to find an integer index vector $\mathbf{x}$ (Eq. (1)) which points to commercial steel profile where each index i points to a cross-sectional area (A_i), the inertias about the main axes (I_{xi}, I_{yi}) and the torsional constant (I_{ti}). These properties are used to define a candidate solution in the evolutionary process. Two different search spaces are adopted for columns and beams, containing 29 and 56 available profiles, respectively, provided in **Table 1**.

$$\mathbf{x} = \{I_1, I_2, ..., I_i\} \tag{1}$$

The objective function $w(\mathbf{x})$ (Eq. (2)) is the weight of the structure, in which L_i is the length, A_i is the cross-sectional area, and ρ_i is the specific mass of the ith member. 7850 kg/m^3 is the specific mass of the steel used in the numerical experiments presented in this chapter.

$$w(\mathbf{x}) = \sum_{i=1}^{N} \rho_i A_i L_i \tag{2}$$

The maximum horizontal displacement and the first natural frequency of vibration are the constraints written as

	Case 1			Case 2		
dv	**[19]**	**[21]**	**TS**	**[22]**	**[20]**	**TS**
A_1	29.2257	30.520	30.268	5.5713	5.4870	5.6593
A_2	0.1000	0.100	0.1018	2.4072	2.2475	2.2830
A_3	24.1821	23.200	23.1493	5.4692	5.5000	5.3987
A_4	14.9471	15.220	15.2456	2.3847	2.2320	2.3229
A_5	0.1000	0.100	0.1001	0.1004	0.1000	0.1000
A_6	0.3946	0.551	0.5546	0.7104	0.7285	0.7159
A_7	7.4958	7.457	7.4902	3.6596	3.7976	3.6969
A_8	21.9249	21.040	21.3433	3.6579	3.7820	3.7667
A_9	21.2909	21.530	21.3958	2.0703	1.9840	1.9386
A_{10}	0.1000	0.100	0.1001	1.9153	1.9065	1.9351
W	5069.09	5060.80	5061.45	532.390	532.124	532.03
nfe	28,0000	—	10,000	21,000	21,000	10,000

Table 1.
Comparison of results of the 10-bar truss.

$$\frac{\delta_{\max}(\mathbf{x})}{\bar{\delta}} - 1 \leq 0$$

$$1 - \frac{f_1(\mathbf{x})}{\bar{f}_1} \leq 0 \tag{3}$$

where δ_{max} is the maximum displacement at the top of the structure, $\bar{\delta}$ is the maximum allowable displacement, f_1 is the first natural frequency of vibration, and $\bar{f}_1$ is the minimum allowed frequency by the standard codes.

3. Differential evolution algorithm and the adaptive penalty scheme

The algorithm used in this study is the traditional DE algorithm, which was introduced in 1995 by Storn and Price [18]. It is based on evolution of population of vectors in the search space. This algorithm has been showing robustness in solving structural mono- and multi-objective optimization problems.

The first step of the algorithm consists of generating a pseudorandom population in the search space. Then, the evolution of the vectors is governed by Eq. (4):

$$\mathbf{x}_{j,i,G} \leftarrow \mathbf{x}_{j,r1,G} + F\left(\mathbf{x}_{j,r2,G} - \mathbf{x}_{j,r3,G}\right) \tag{4}$$

where $x_{j,i,G}$ represents the new individual of the new generation; $x_{j,r1,G}$, $x_{j,r2,G}$, and $x_{j,r3,G}$ represent, respectively, the base vector and two other vectors from the previous generation (both three vectors are randomly selected and different among them); and F represents the scale factor of the difference between vectors. This expression (Eq. 4) is illustrated in **Figure 1**.

Mutation and crossover operators are considered in the differential evolution, and there is a predetermined probability of crossover (Pcr) as well as a probability of mutation between the new and the old individual.
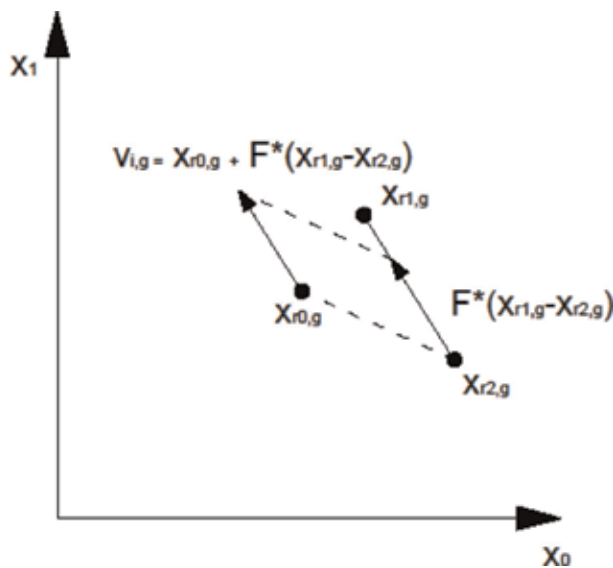
Figure 1.
Visual representation of DE scheme.

The following flowchart represents the scheme of DE:

Initialize pseudorandom population
For i = 1: NPOP
    Select randomly J ∈ {1,..., NPOP}
    For j = 1: NPOP
        Select randomly *rand* ∈ [0, 1]
        If rand < Pcr or j = J
            $\mathbf{x}_{j,i,G} \leftarrow \mathbf{x}_{j,r1,G} + F(\mathbf{x}_{j,r2,G} - \mathbf{x}_{j,r3,G})$
        Else
            $\mathbf{x}_{j,i,G} \leftarrow \mathbf{x}_{j,r1,G}$
        end if
    end For
end For

where NPOP represents the number of population.

To handle the constraints, the APM is adopted, proposed by Lemonge and Barbosa [19].

The fitness function $W(\mathbf{x})$ is defined by Eq. (5).

$$W(\mathbf{x}) = \begin{cases} w(\mathbf{x}), & \text{if } \mathbf{x} \text{ is feasible} \\ \overline{w}(\mathbf{x}) + \sum_{jj=1}^{n_c} k_{jj}v_{jj}(\mathbf{x}), & \text{otherwise} \end{cases} \quad (5)$$

where $w(\boldsymbol{x})$ is the objective function of the candidate solution without penalization Eq.(6)

$$\overline{w}(\mathbf{x}) = \begin{cases} w(\mathbf{x}), & \text{if } w(\mathbf{x}) > \langle w(\mathbf{x}) \rangle \\ \langle w(\mathbf{x}) \rangle, & \text{if } w(\mathbf{x}) \leq \langle w(\mathbf{x}) \rangle \end{cases} \quad (6)$$

where $\langle w(\boldsymbol{x}) \rangle$ is the average value of the objective function of the solutions of the current population. The penalty parameter k_{jj} is defined in Eq.(7):

$$k_{jj} = |\langle w(\mathbf{x}) \rangle| \frac{\langle v_{jj}(\mathbf{x}) \rangle}{\sum_{ll=1}^{n_c} [v_{ll}(\mathbf{x})]^2,} \quad (7)$$

where $\langle v_{jj}(\mathbf{x}) \rangle$ means the violation of the jj-th constraint averaged over the current population considering only infeasible individuals. The complete formulation of the APM can be found in [19].

4. Numerical examples

4.1 Preliminary experiment

To validate the proposed search mechanism, a well-known benchmark 10-bar truss, shown in **Figure 2**, is considered. Two cases are analyzed: in the first one, the problem consists of weight minimization considering displacements and stresses as constraints and, in the second case, minimization of its weight considering natural frequencies as constraints; for both cases the design variables are the cross-sectional areas of the bars (totalizing 10 variables). The truss has Young's modulus equal to
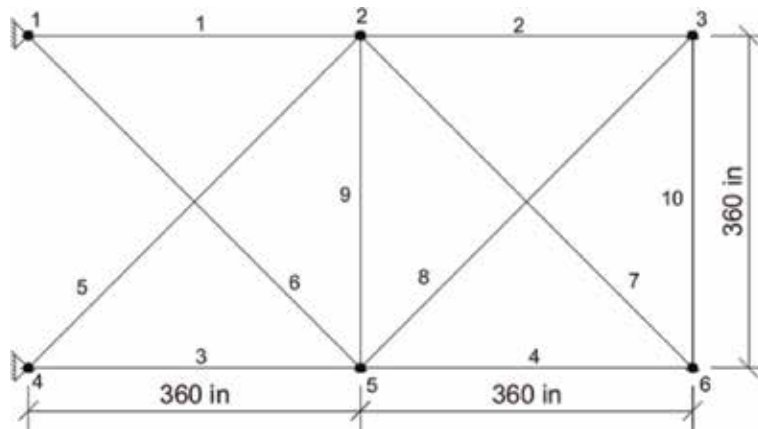
Figure 2.
The 10-bar truss.

10^4 ksi (68.95 GPa) and material density equal to 0.1 lb/in³ (2770 kg/m³). For case 1, the upper and lower bounds are equal to 0.1 and 33.50 in², and two loads of 100 kips (444.82 kN) each are applied at nodes 2 and 4; for case 2, the bounds are equal to 0.1 and 7.75 in², and an additional mass of 1000 lbs. (454.54 kg) is attached to free nodes (1–4). Constraints are set to ±25 ksi (for both compression and tension) and 2 inches for case 1, and also $f_1 \geq 7$ Hz, $f_2 \geq 15$ Hz, and $f_3 \geq 20$ Hz for case 2.

Table 2 shows the design variables (dv) (in² for case 1 and cm² for case 2), the optimum weights (W) (lb for case 1 and kg for case 2) obtained for both cases, as well as a comparison with some results found in the literature where TS means the results obtained with this study. For both cases, 50 independent runs were performed; the population size is 50 which evolved in 200 generations leading to 10,000 function evaluations (nfe).

4.2 Design loads

The first mutlistorey 3D steel frame is a simple three-storey steel frame, with 3 m of width, 6 m of length, and 9 m of height equally spaced. This 3D frame is subjected to lateral wind and gravity loads. The gravity and wind loads are defined based on the Brazilian technical codes NBR 6123 [2], detailed on the next subsections. The model in finite elements for the first 3D frame consists in 39 members and 24 joints depicted in **Figure 3**.

4.2.1 Wind loads

To define the forces due to the wind on the columns, it demands to determine the dynamic pressure (q) acting on the area of the larger façade. For this purpose, two parameters, the wind basic velocity (V_0) and the wind characteristic velocity (V_k), are necessary. The basic velocity V_0 is inherent of the region and assumed as the velocity of 3 s gust, exceeded in mean once in 50 years, 10 m above the ground on an open and plain field. For the city of Juiz de Fora, Minas Gerais State, Brazil, the basic velocity is equal to $V_0 = 35$ m/s. The characteristic velocity is defined by Eq. (8), where S_1 (topographic factor), S_2 (terrain roughness factor), and S_3 (statistic factor) are weighting coefficients resulting in 25.9 m/s as written in Eq. (9) ([2]).
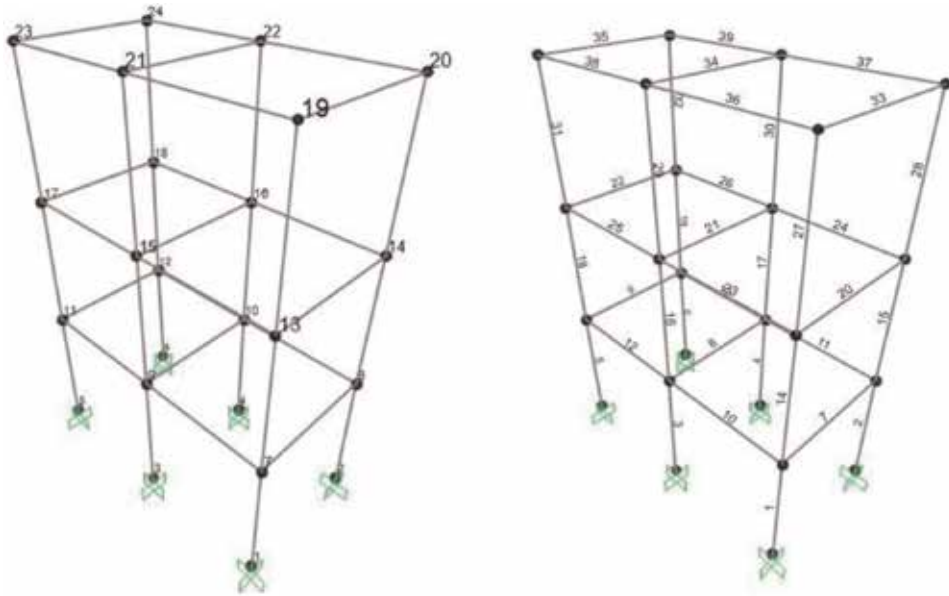
Figure 3.
The 39 members frame—joints and elements mapping.

$$V_k = V_0 S_1 S_2 S_3 \tag{8}$$

$$V_k = 35 \times 1.0 \times 0.74 \times 1.0 = 25.9 \text{ m/s} \tag{9}$$

With the characteristic velocity, it is possible to determine the dynamic pressure on the larger facade of the frame through Eq. (10).

$$q = 0.613 V_k^2 = 0.613 \times 25.9^2 = 411.21 \text{ N/m}^2 \tag{10}$$

The dynamic pressure acting on the frame's larger facade, q = 0.411 kN/m², must be transferred as a uniform load applied to the columns; to transfer the area loading to columns, the influence area of corner columns (CC) (red area = 13.5 m²) and middle columns (MC) (blue area 27 m²) are used; the steps are detailed in Eqs.(11) and (12) and **Figure 4**, where P_c and P_M are the uniform wind load on the corner columns and middle columns, respectively.

$$P_C = 0.411 \, \frac{\text{kN}}{\text{m}^2} \times \frac{13.5 \text{ m}^2}{9 \text{ m}} = 0.62 \text{ kN/m} \tag{11}$$

$$P_M = 0.411 \, \frac{\text{kN}}{\text{m}^2} \times \frac{27 \text{ m}^2}{9 \text{ m}} = 1.23 \text{ kN/m} \tag{12}$$

4.2.2 Gravity loads

Two different types of gravity loads are considered: dead loads and live loads. The first one refers to self-weight of the structural elements, such as, the concrete slabs, which was adopted with a thickness equal to 10 cm, and the second one corresponds to the occupation. The dead load acting on the floor is 3 kN/m², and the live is 2 kN/m². The inner beams (IB) would be more loaded (the largest influence area) than the outer beams (OB), as can be observed in **Figure 5**. The blue area (4.5 m²) transfers its weight to the inner beams, and the red area (2.25 m²) transfers
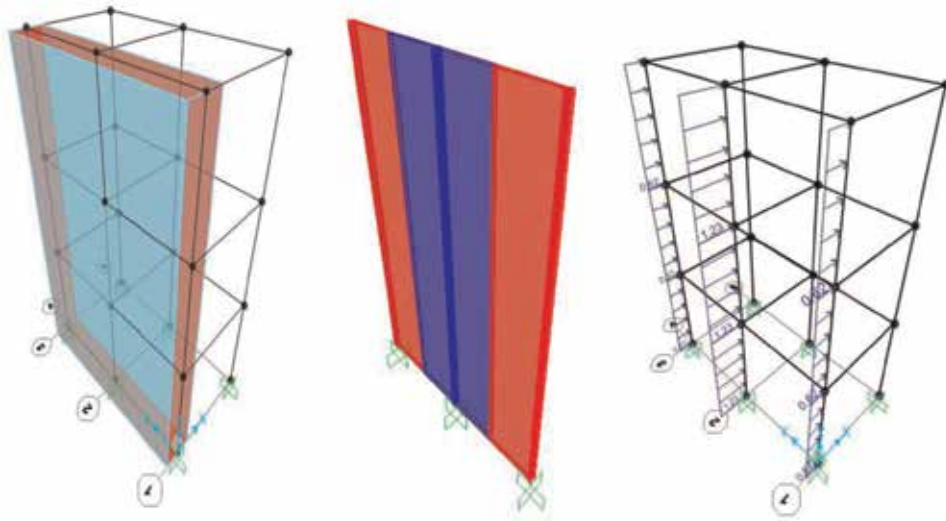
Figure 4.
Wind loads on columns.
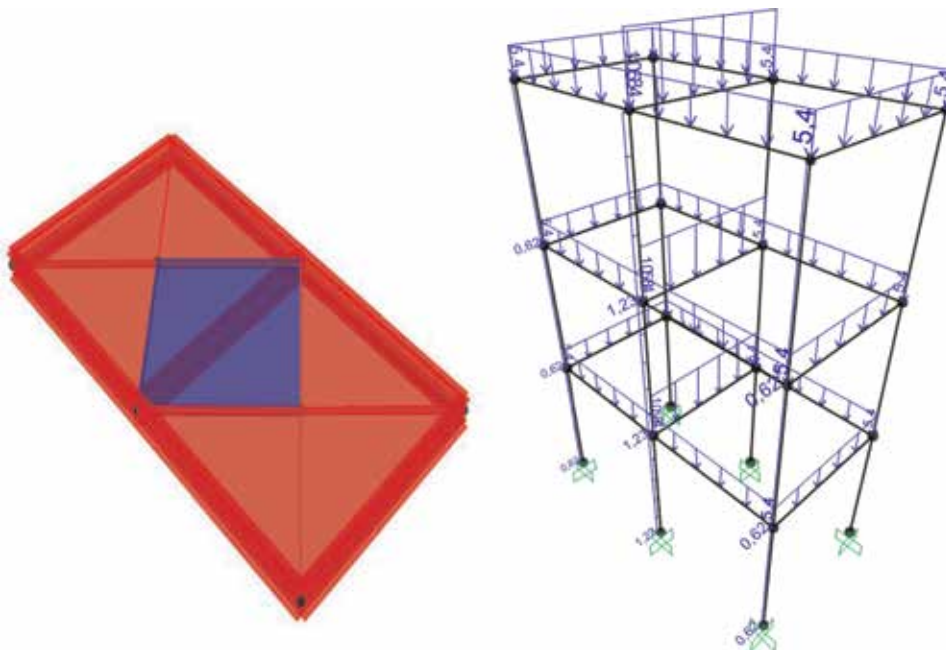
Figure 5.
Influence area for beams—design loads.

its weight to the outer beams. The design factor used for dead loads was 1.4 and for the live loads 1.5, according to the Brazilian Technical Standard code [2]. Eqs. (13) and (14) summarize the calculus of the design loads adopted in the experiments, according to the Brazilian Technical Standard code, where P_i and P_o are the uniform loading on inner beams and outer beams, respectively [3].

$$P_i = \left(1.4 \times 3\frac{\text{kN}}{\text{m}^2} + 1.5 \times 2\frac{\text{kN}}{\text{m}^2} \right) \times \frac{4.5\ \text{m}^2}{3\ \text{m}} = 10.8\ \text{kN/m} \tag{13}$$

Profiles for columns			Profiles for beams		
W 150 × 22.5	W 250 × 89	W 150 × 13	W 310 × 21	W 410 × 38.8	W 530 × 66
W 150 × 29.8	W 250 × 101	W 150 × 18	W 310 × 23.8	W 410 × 46.1	W 530 × 72
W 150 × 37.1	W 250 × 115	W 150 × 24	W 310 × 28.3	W 410 × 53	W 530 × 74
W 200 × 35.9	W 310 × 79	W 200 × 15	W 310 × 32.7	W 410 × 60	W 530 × 82
W 200 × 41.7	W 310 × 93	W 200 × 19.3	W 310 × 38.7	W 410 × 67	W 530 × 85
W 200 × 46.1	W 310 × 97	W 200 × 22.5	W 310 × 44.5	W 410 × 75	W 530 × 92
W 200 × 52	W 310 × 107	W 200 × 26.6	W 310 × 52	W 410 × 85	W 530 × 101
W 200 × 53	W 310 × 110	W 200 × 31.3	W 360 × 32.9	W 460 × 52	W 530 × 109
W 200 × 59	W 310 × 117	W 250 × 17.9	W 360 × 39	W 460 × 60	W 610 × 101
W 200 × 71	W 310 × 125	W 250 × 22.3	W 360 × 44	W 460 × 68	W 610 × 113
W 200 × 86	W 360 × 91	W 250 × 25.3	W 360 × 51	W 460 × 74	W 610 × 125
W 250 × 62	W 360 × 101	W 250 × 28.4	W 360 × 57.8	W 460 × 82	—
W 250 × 73	W 360 × 110	W 250 × 32.7	W 360 × 64	W 460 × 89	—
W 250 × 80	W 360 × 122	W 250 × 38.5	W 360 × 72	W 460 × 97	—
W 250 × 85	—	W 250 × 44.8	W 360 × 79	W 460 × 106	—

Table 2.
Discrete search spaces for columns and beams.

$$P_o = \left(1.4 \times 3\frac{kN}{m^2} + 1.5 \times 2\frac{kN}{m^2}\right) \times \frac{2.25\ m^2}{3\ m} = 5.4\ kN/m \qquad (14)$$

4.3 Experiment 1

The first experiment consists of the three-storey steel frame to minimize the weight as depicted in **Figure 3**, considering the loads discussed in the previous subsection subjected to the maximum horizontal displacements as the constraint that occur on the top of the frame. The frame has 9 m of height leading to an allowable displacement at the top equal to 22.5 mm as Eq. (15) shows:

$$\bar{\delta} = \frac{H}{400} = \frac{9000}{400} = 22.5\ mm \qquad (15)$$

Five independent runs and 100 generations with a population of 50 individuals are the parameters set for DE. The best solution found is detailed in **Figure 5**. It is possible to note that the algorithm reached both the lightest profile for beams and columns, which are W 150 × 13 (red) and W 150 × 22.5 (blue), respectively, leading to a final weight of 2050 kg. For the best solution found, rigorously feasible in the evolutionary process, the maximum displacement is 19.6 mm as can be observed in the scale of **Figure 6**.

4.4 Experiment 2

The second experiment has the same characteristics as the first one. However, a constraint concerning the first natural frequency of vibration is added (Eq. (16)) that must be at least 4 Hz, according to the dynamic comfort values prescribed by NBR 8800 [3]. The natural frequencies are obtained calculating the eigenvalues of the matrix $[(f_{nf}^2 \text{ x M} + K)]$ [23], where M and K are the mass and stiffness matrices,
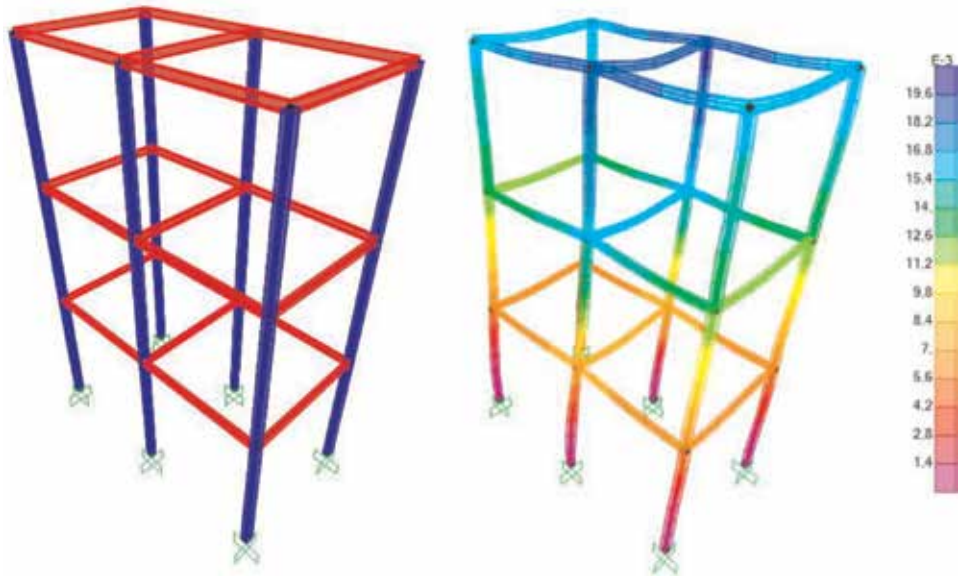
Figure 6.
The best solution and the displacement field for the Experiment 1.

respectively, and f_{nf} is the equivalent eigenvectors concerning the nf natural frequencies of vibration of the structure. Also a member grouping is adopted, considering the symmetry of structure. In optimized structures, it can be attractive to use a reduced number of distinct cross-sectional areas to minimize the costs of fabrication, transportation, storing, checking, and welding, thereby providing labor savings.

Thus, the member grouping is conducted such as corner columns, middle columns, outer beams, and inner beams (IB) form four different groups which each group will have the same profile as defined in **Figure 7** and **Table 3**.

$$\frac{\delta_{\max}(\mathbf{x})}{22.5} - 1 \leq 0$$
$$1 - \frac{f_1(\mathbf{x})}{4} \leq 0$$

(16)
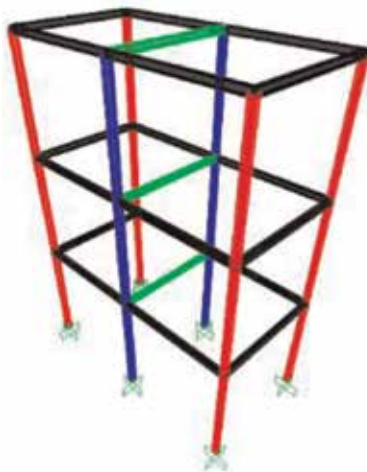
Figure 7.
Member grouping for the Experiment 2.

Group	Characteristics	Color
1	Corner columns	Red
2	Middle columns	Blue
3	Inner beams	Green
4	Outer beams	Black

Table 3.
Member grouping for the Experiment 2.

The DE parameters are the same in Experiment 1. The best solution found presented a final weight of 2587 kg, the maximum displacement of 12.9 mm, and the first natural frequency of vibration equal to 4.14 Hz corresponding, as expected, to a feasible solution. It is interesting to note that the algorithm distributed masses along the structure in a better way in order to satisfy the frequency constraint, in this case, decreasing the maximum displacement. **Figure 8** and **Table 4** show the detailed results.

4.5 Experiment 3

This numerical experiment consists in to minimize the weight of a 3D steel frame with six-storeys and 78 members, as illustrated in **Figure 9**, and it is subjected to wind load and a constraint concerning the maximum horizontal displacement at the top of the frame. In this experiment, distinct member groupings are adopted to show how the final weights decrease as more different profiles are used. In this sense, the members are grouped in two, four, and eight groups independently.

The wind and gravity loads are defined in the same way as the previous experiment, and the displacement constraint is written as (Eq. (17)):

$$\bar{\delta} = \frac{H}{400} = \frac{18000}{400} = 45\text{ mm} \qquad (17)$$

Figure 8.
The best solution and the displacement field for the Experiment 2.

Group	Characteristics	Color	Cross section
1	Corner columns	Red	W 150 × 22.5
2	Middle columns	Blue	W 200 × 46.1
3	Inner beams	Green	W 150 × 13
4	Outer beams	Black	W 200 × 15
Maximum displacement		—	12.9 mm
First natural frequency		—	4.14 Hz
Total weight		—	2587 kg

Table 4.
Optimum solution found for the Experiment 2.
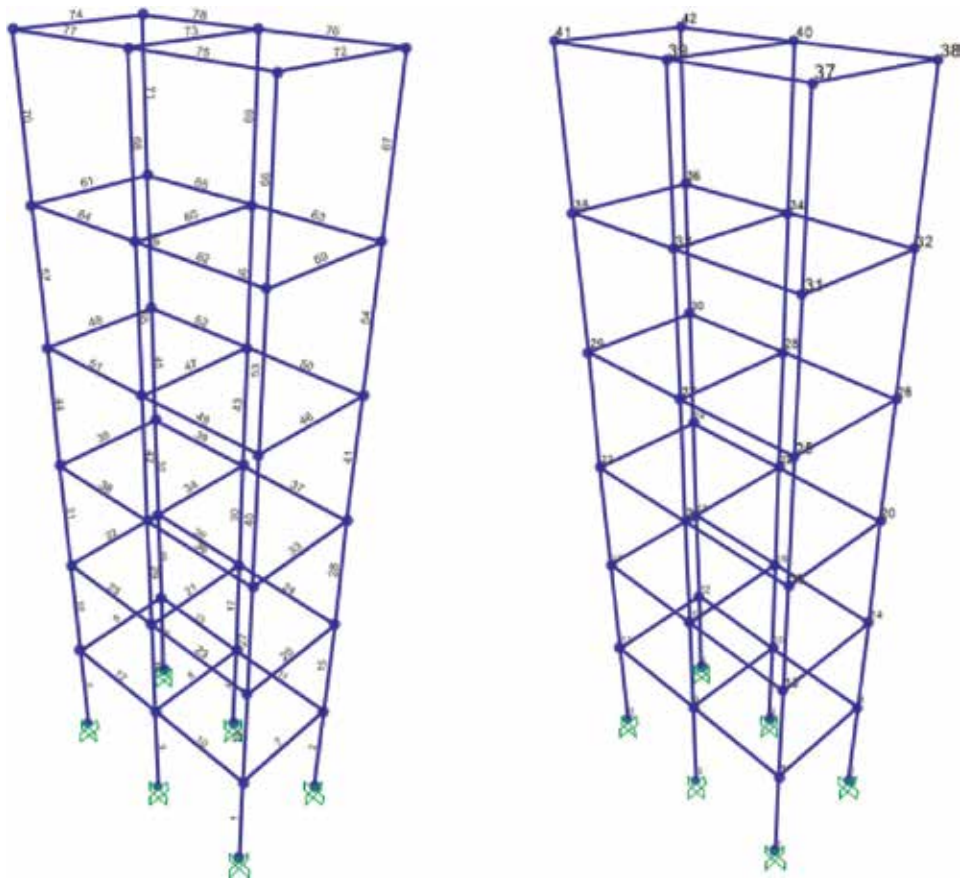
Figure 9.
The 78 members frame joints and elements mapping.

4.5.1 Members linked in two groups

Firstly, the problem considers the possibility of using only two distinct profiles, one for the columns and other for the beams. The member grouping adopted is described in the **Table 5** and in **Figure 10**.

The DE parameters are the same as Experiment 2, and best solution found is detailed in **Table 6** and in **Figure 11**.

Group	Characteristics	Color
1	Columns	Red
2	Beams	Blue

Table 5.
Experiment 3.1—members linked in two groups.
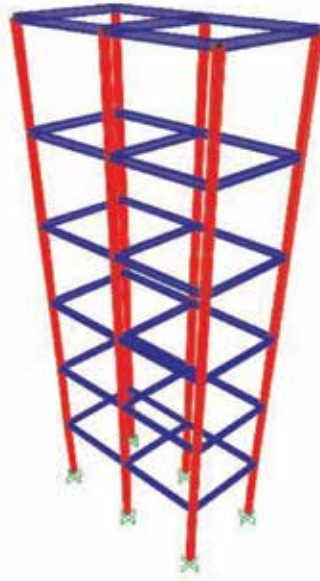
Figure 10.
Experiment 3.1—members linked in two groups according to **Table 5***.*

Group	Characteristics	Color	Cross section
1	Columns	Red	W 150 × 29.8
2	Beams	Blue	W 360 × 44
Maximum displacement			22.6 mm
Total weight			8971 kg

Table 6.
The best solution of Experiment 3.1.

4.5.2 Members linked in four groups

In the second analysis of Experiment 3, the members are linked in four distinct groups as described in **Table 7** and **Figure 12**, and the best result found is detailed in **Figure 13** and **Table 8**.

4.5.3 Members linked in eight groups

Finally, the same problem is optimized with the members linked in eight groups as shown in **Table 9** and **Figure 14**. **Table 10** and **Figure 15** show the best solution found for Experiment 3.3.
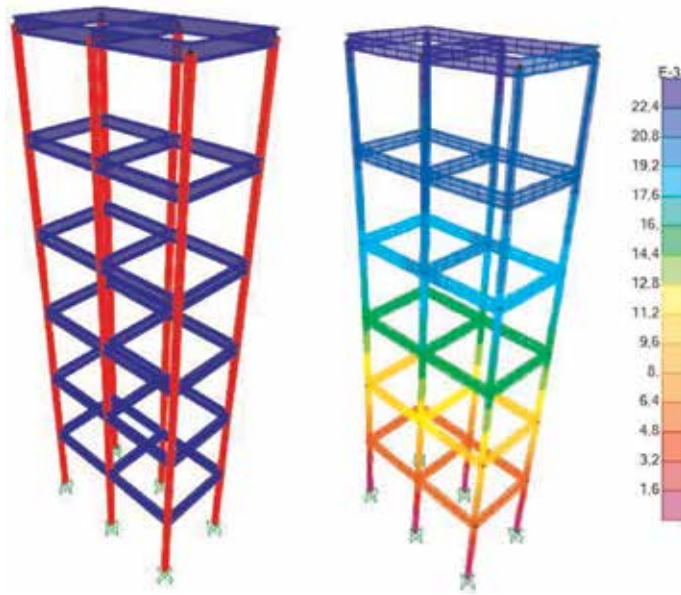
Figure 11.
The best solution and displacement field of Experiment 3.1.

Group	Characteristics	Color
1	Corner columns	Red
2	Middle columns	Black
3	Inner beams	Green
4	Outer beams	Blue

Table 7.
Experiment 3.2—members linked in four groups.
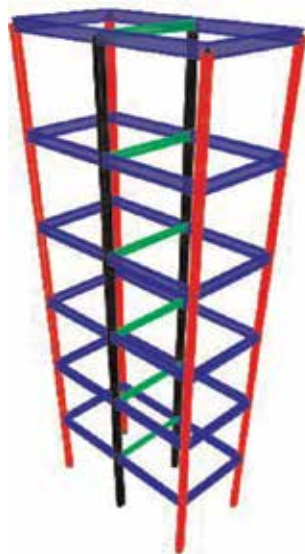
Figure 12.
*Experiment 3.2–members linked in four groups according to **Table 7**.*

Figure 13.
The best solution and displacement field of Experiment 3.2.

Group	Characteristics	Color	Cross section
1	Corner columns	Blue	W 200 × 35.9
2	Middle columns	Red	W 150 × 22.5
3	Inner beams	Black	W 150 × 13
4	Outer beams	Green	W 310 × 38.7
Maximum displacement			23 mm
Total weight			7851 kg

Table 8.
The best solution of Experiment 3.2.

Group	Characteristics	Color
1	Corner columns—floors 1, 2, and 3	Blue
2	Middle columns—floors 1, 2, and 3	Red
3	Inner beams—floors 1, 2, and 3	Green
4	Outer beams—floors 1, 2, and 3	Black
5	Corner columns—floors 4, 5, and 6	Cyan
6	Middle columns—floors 4, 5, and 6	Magenta
7	Inner beams—floors 4, 5, and 6	Yellow
8	Outer beams—floors 4, 5, and 6	Gray

Table 9.
Experiment 3.3—members linked in eight groups.

Figure 14.
Experiment 3.3—members linked in eight groups according to **Table 9**.

Group	Characteristics	Color	Cross section
1	Corner columns—floors 1, 2, and 3	Blue	W 200 × 46.1
2	Middle columns—floors 1, 2, and 3	Cyan	W 150 × 22.5
3	Inner beams—floors 1, 2, and 3	Red	W 150 × 13
4	Outer beams—floors 1, 2, and 3	Black	W 310 × 38.7
5	Corner columns—floors 4, 5, and 6	Cyan	W 150 × 22.5
6	Middle columns—floors 4, 5, and 6	Cyan	W 150 × 22.5
7	Inner beams—floors 4, 5, and 6	Red	W 150 × 13
8	Outer beams—floors 4, 5, and 6	Gray	W 250 × 32.7
Maximum displacement			26 mm
Total weight			7421 kg

Table 10.
The best solution of Experiment 3.3.

4.6 Experiment 4

This experiment considers the first natural frequency of vibration as an additional constraint (Eq. (18)) to the six-storey 3D frame. However, the DE did not find any feasible solution. Thus, a new frame presenting 114 members (**Figure 16**) with bracings is proposed to stiffen the candidate solutions, rising the chances of reaching feasible solutions.

Figure 15.
The best solution and displacement field of Experiment 3.3.
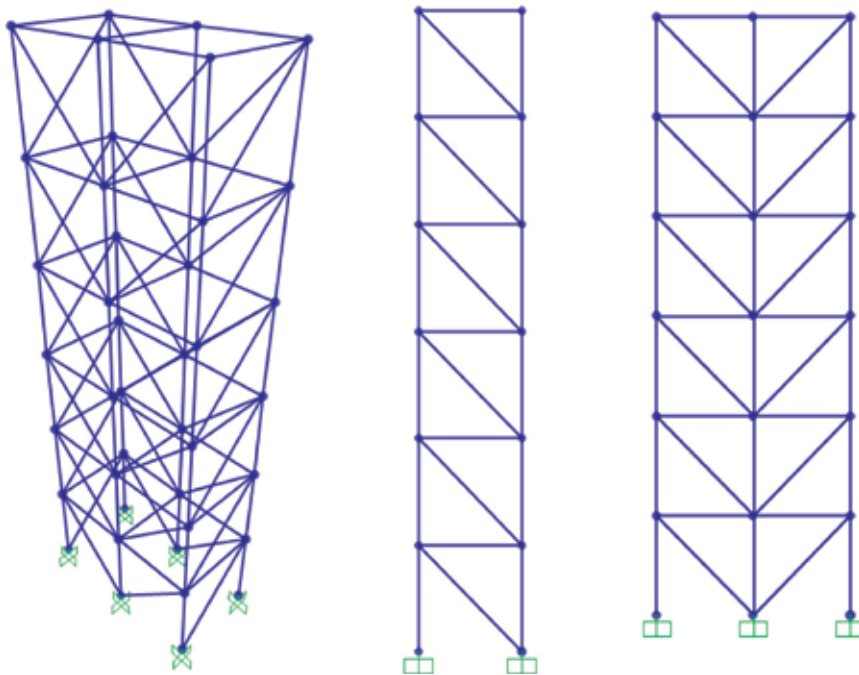
Figure 16.
One hundred fourteen members 3D frame—long and short façade.

$$\frac{\delta_{\max}(\mathbf{x})}{45} - 1 \leq 0$$

$$1 - \frac{f_1(\mathbf{x})}{4} \leq 0 \tag{18}$$

For this improved structure, the members are linked in five different groups described in **Table 11** and in **Figure 17**.

Group	Characteristics	Color
1	Corner columns	Red
2	Middle columns	Gray
3	Inner beams	Black
4	Outer beams	Blue
5	Bracers	Cyan

Table 11.
Experiment 4—members linked in five groups.
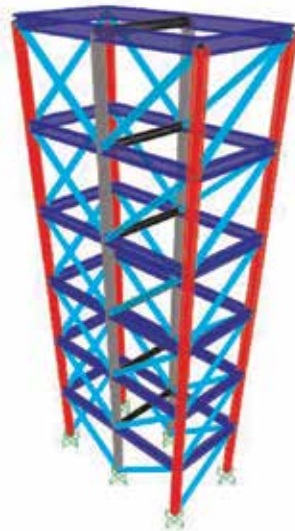
Figure 17.
Experiment 4—members linked in five groups according to **Table 11**.
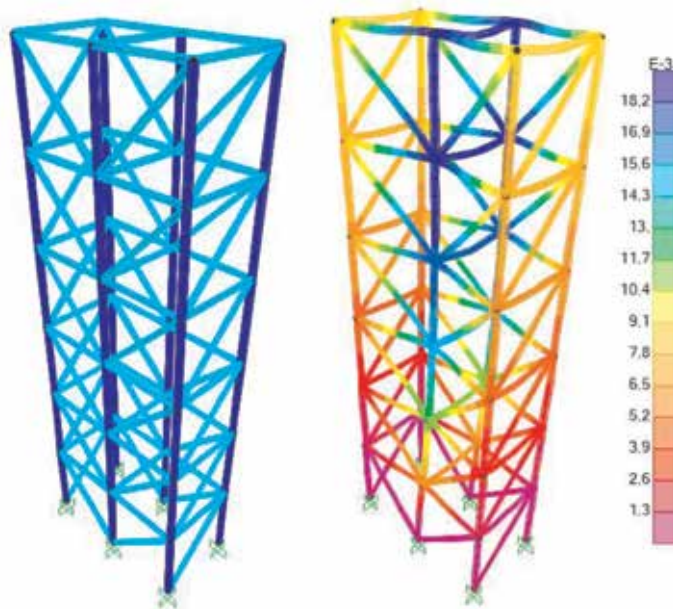
Figure 18.
The best solution and displacement field of Experiment 4.

Group	Characteristics	Color	Cross section
1	Corner columns	Blue	W 150 × 22.5
2	Middle columns	Blue	W 150 × 22.5
3	Inner beams	Cyan	W 150 × 13
4	Outer beams	Cyan	W 150 × 13
5	Bracers	Cyan	W 150 × 13
Maximum displacement		—	19 mm
First natural frequency		—	4.38 Hz
Total weight		—	6091 kg

Table 12.
The best solution of Experiment 4.

The best result found presented the lightest structure of this set of experiments, even though presenting a greater number of members than the previous structural configuration. The maximum displacement at the top of the frame is 19 mm, and the first natural frequency of vibration is 4.38 Hz, leading to a feasible solution. **Figure 18** and **Table 12** detail the best solution for this experiment.

5. Analysis of results

Two numerical experiments discussed concerning a three-storey 3D frame, in which it was possible to observe the importance of the natural frequency of vibration considered as a constraint. In general, it is neglected in the great majority of the structural optimization problems. The best solution found for Experiment 2 was heavier than the best solution found in Experiment 1. It can be justified since the first natural frequency of vibration was included in the problem formulation resulting in a heavier optimized structure.

A set of three experiments concerning a six-storey 3D frame were conducted with the members linked in three different groups. The constraints for these experiments are the maximum displacement at the top of the frame. The members were linked in two, four, and eight groups, and, as expected, the weights decrease as the number of linked bars increases. It is important to note from the results of the case where the members were linked in eight groups (Experiment 3.3) that the algorithm found only five distinct profiles.

Table 13 summarizes the results of Experiment 3, and the graphic in **Figure 19** is a curve of the tradeoff presenting a comparison of each one of the best solutions and their corresponding number of distinct profiles used.

Another important point was the fact that no feasible solutions were found for the six-storey frame with no bracings, considering the constraint concerning the first natural frequency of vibration. This fact indicated the conception of a new model increasing the stiffness of the structure to make possible a feasible optimized solution. Thus, bracings were considered in the new model increasing the total number of members. The result of Experiment 4 was very interesting leading to a lighter structure than the three other experiments (3.1, 3.2, and 3.3), even if presenting a more complex geometry with more members after the inclusion of the bracings in the model. The importance of the bracings in 3D steel frames was shown not only concerning their stability and stiffness but also improving its dynamic behavior.

Number of groups	Maximum displacement (mm)	Weight (kg)
2	22.6	8971
4	23	7851
8	26	7421

Table 13.
Analysis of results of Experiment 3.
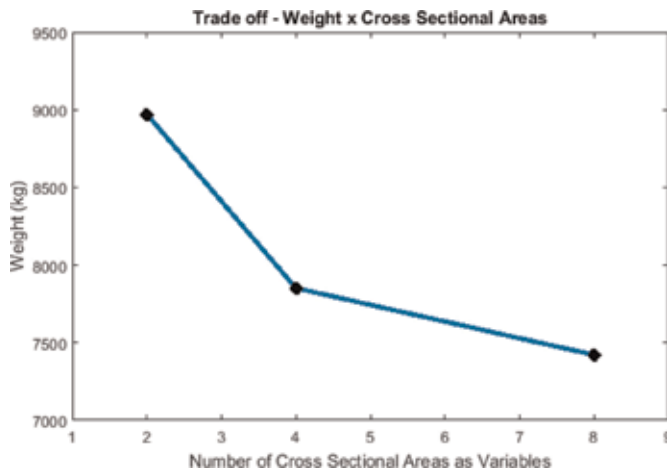
Figure 19.
Tradeoff curve of Experiment 3.

6. Conclusions and extensions

The study conducted in this chapter focused on the minimization of the weight of 3D steel frames, subjected to constraints concerning horizontal displacements and natural frequencies of vibration. It is interesting to note the importance of a structural optimization study before the design is conceived, which leads to more competitive and sometimes counterintuitive.

In the experiments addressed in this chapter, it is easy to conclude that the natural frequency of vibration is an essential characteristic to be considered in the formulation of the structural optimization problems.

As future works the approaches will extend to multi-objective optimization problems with more constraints, such as, stress, stability, geometry, and inter-storey drifts, introducing more real aspects to the optimization problems in engineering. Strategies should be considered for automatic grouping of members without the need for preliminary analysis by the designer. For this, special encodings will be used via cardinality constraints as can be seen in the structural optimization problems discussed in the references [20, 24, 25].

7. Remark

The codes used to solve the optimization problems presented in this chapter are written in Matlab® language, and the final results, as well as the figures, are checked by the SAP 2000®.

Acknowledgements

Conflict of interest

The authors declare that they have no conflicts of interest.

Author details

Cláudio H.B. Resende, José P.G. Carvalho, Afonso C.C. Lemonge*
and Patricia H. Hallak
Graduate Program in Civil Engineering, Federal University of Juiz de Fora,
Juiz de Fora, Brazil

*Address all correspondence to: afonso.lemonge@ufjf.edu.br

IntechOpen

References

[1] AISC-ASD. Manual of Steel Construction-Allowable Stress Design. 9th ed. Chicago, IL, USA: American Institute of Steel Construction; 1989

[2] NBR 6123. Forces due to the wind in buildings. Brazilian Association of Technical Standards; Rio de Janeiro; 1988. (In Portuguese)

[3] NBR 8800. Design of steel structures and mixed structures of steel and concrete of buildings. Brazilian Association of Technical Standards; Rio de Janeiro; 2008. (In Portuguese)

[4] Artar M, Daloğlu AT. Optimum weight design of steel space frames with semi-rigid connections using harmony search and genetic algorithms. Neural Computing and Applications. 2018; **29**(11):1089-1100

[5] Maheri MR, Talezadeh M. An enhanced imperialist competitive algorithm for optimum design of skeletal structures. Swarm and Evolutionary Computation. 2018;**40**: 24-36

[6] Aydoğdu İ, Akın A, Saka MP. Design optimization of real world steel space frames using artificial bee colony algorithm with levy flight distribution. Advances in Engineering Software. 2016;**92**:1-14

[7] Talatahari S, Gandomi AH, Yang XS, Deb S. Optimum design of frame structures using the eagle strategy with differential evolution. Engineering Structures. 2015;**91**:16-25

[8] Maheri MR, Shokrian H, Narimani MM. An enhanced honey bee mating optimization algorithm for design of side sway steel frames. Advances in Engineering Software. 2017;**109**:62-72

[9] Kaveh A, BolandGerami A. Optimal design of large-scale space steel frames using cascade enhanced colliding body optimization. Structural and Multidisciplinary Optimization. 2017; **55**(1):237-256

[10] Jalili S, Hosseinzadeh Y, Taghizadieh N. A biogeography-based optimization for optimum discrete design of skeletal structures. Engineering Optimization. 2016;**48**(9): 1491-1514

[11] Gholizadeh S, Poorhoseini H. Optimum design of steel frame structures by a modified dolphin echolocation algorithm. Structural Engineering and Mechanics. 2015;**55**(3): 535-554

[12] Gholizadeh S, Milany A. An improved fireworks algorithm for discrete sizing optimization of steel skeletal structures. Engineering Optimization. 2018;**50**(11):1829-1849

[13] Hasançebi O. Cost efficiency analyses of steel frameworks for economical design of multi-storey buildings. Journal of Constructional Steel Research. 2017;**128**:380-396

[14] Memari AM, Madhkan M. Optimal design of steel frames subject to gravity and seismic codes' prescribed lateral forces. Structural Optimization. 1999;**18**: 56-66

[15] Kameshki ES, Saka MP. Genetic algorithm based optimum bracing design of nonswaying tall plane frames. Journal of Constructional Steel Research. 2001;**57**:1081-1097

[16] Liang QQ, Xie YM, Steven GP. Optimal topology design of bracing systems for multi-storey steel frames. Journal of Structural Engineering. 2000; **126**(7):823-829

[17] Pavlovčič L, Krajnc A, Beg D. Cost function analysis in the structural

optimization of steel frames. Structural and Multidisciplinary Optimization. 2004;**28**(4):286-295

[18] Storn R, Price K. Differential evolution a simple and efficient adaptive scheme for global optimization over continuous spaces. Technical Report; Berkeley, CA: University of California; 1995. 95-012

[19] Lemonge ACL, Barbosa HJC. An adaptive penalty scheme for genetic algorithms in structural optimization. International Journal for Numerical Methods in Engineering. 2004;**59**(5): 703-736

[20] Carvalho JP, Lemonge AC, Carvalho ÉC, Hallak PH, Bernardino HS. Truss optimization with multiple frequency constraints and automatic member grouping. Structural and Multidisciplinary Optimization. 2018;**57**(2):547-577

[21] Haftka RT, Kamat MP. Elements of Structural Optimization. Dordrecht: Martinus Nighoff; 1985

[22] Kaveh A, Javadi S. Shape and size optimization of trusses with multiple frequency constraints using harmony search and ray optimizer for enhancing the particle swarm optimization algorithm. Acta Mechanica. 2014; **225**(6):1595-1605

[23] Bathe KJ. Finite Element Procedures. Watertown, MA, USA: Prentice Hall, Pearson Education Inc.; 2006

[24] Barbosa HJ, Lemonge AC, Borges CC. A genetic algorithm encoding for cardinality constraints and automatic variable linking in structural optimization. Engineering Structures. 2008;**30**(12):3708-3723

[25] Lemonge AC, Barbosa HJ, Coutinho AL, Borges CC. Multiple cardinality constraints and automatic member grouping in the optimal design of steel framed structures. Engineering Structures. 2011;**33**(2):433-444

Section 2

Mass-Saving in Structures

Chapter 4

Topology Optimization Applications on Engineering Structures

Aykut Kentli

Abstract

Over the years, several optimization techniques were widely used to find the optimum shape and size of engineering structures (trusses, frames, etc.) under different constraints (stress, displacement, buckling instability, kinematic stability, and natural frequency). But, most of them require continuous data set where, on the other hand, topology optimization (TO) can handle also discrete ones. Topology optimization has also allowed radical changes in geometry which concludes better designs. So, many researchers have studied on topology optimization by developing/using different methodologies. This study aims to classify these studies considering used methods and present new emerging application areas. It is believed that researchers will easily find the related studies with their work.

Keywords: topology optimization, finite element method

1. Introduction

Topology optimization (TO) is carried out to obtain an optimal structural layout [1]. It is one of the branches of optimization methods differing from size and shape optimization. As expected, as a type of optimization method, it has constant parameters, like applied loads, material type, etc., objective function and constraints which change for every problem, and lastly variable which are the parameters of the material layout. In shape optimization, it aimed to find the position of the member of the structure, while in size optimization, only finding the size of the members is enough. In both cases, there will be no change in the number of members. On the other hand, in topology optimization some part or member of the structure will be deleted and a new layout will be prepared [2]. It is generally preferred to use finite element method (FEM) as meshing eases to find the places to be deleted. But as an optimization algorithm, several kinds are used including both gradient-based such as optimality criteria methods and non-gradient-based algorithms such as genetic algorithm [3].

The topology optimization of structures has proven to be a valuable tool for the identification of the best concepts in early phases of the design process. It is widely used in lightweight design of structures in automotive and aerospace industry, as well as in civil engineering, material science, and biomechanics [1, 4, 5].

This chapter will give brief introduction on topology optimization and later give related studies under several classifications. There are several well-prepared and

intensely examined review studies in literature, but some of them are on specific application area (vibration problems [6], continuum structures [7]) or are on a specific methodology (evolutionary algorithms [8, 9], level-set methods [10]), or recent studies are not included [11, 12]. This study mostly aims to present recent studies while giving brief description on previous ones.

2. Topology optimization

During the twentieth century, architects and engineers have used innovative and novel methods to develop optimum forms of structures and sculptures. While the techniques employed by these innovators generated efficient and aesthetic forms, they shared a common limitation: reaching optimum structure. Although the purpose of applying topology optimization has never been a standard procedure, developments in finding optimum structure form let the researchers and designers be free to constructing better designs [13, 14].

Topology optimization offers conceptual design for lighter and stiffer structures. It helps to reach to efficient and aesthetic designs within a small time interval (**Figure 1**). The benefits are:

- Building weight-saving and complete designs.

- Decrease needed time to present and test product.

- By the help of FEM software, you are able to check your design from the perspective of:

    ○ Determining feasible design range.

    ○ Accurate checking for different loads and conditions.

    ○ Considering design and manufacturing constraints [15].

By the time, TO has shown its power and efficiency in the design of structures by the increase in advances on computational speed and power. Changes in computer hardware and software technology have also changed the approach to topology formation of structures. Nowadays, you could use a drawing software in forming different topologies as if it is a standard task, and so, you are able to alter
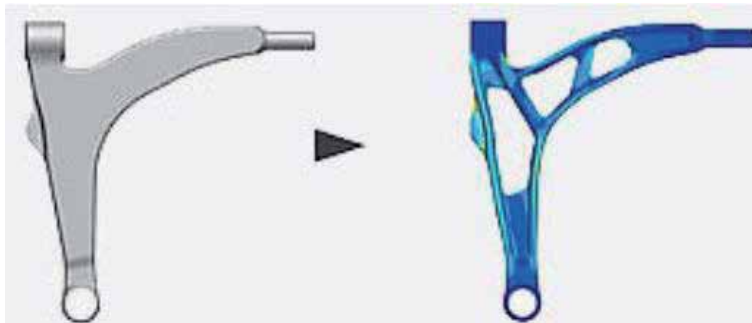
Figure 1.
Optimized unit by using topology optimization approach (Dassault) [15].

old designs and produce new alternative designs in virtual environment. Designers and engineers are pleased to have such a powerful tool in their work [16].

2.1 General form

A topology optimization problem can be written in the general form of an optimization problem as [3, 17]:

$$minimize_\rho\, F = F(u(\rho),\rho) = \int_\Omega f(u(\rho),\rho)dV$$
$$subject\ to\ G_0(\rho) = \int_\Omega \rho dV - V_0 \tag{1}$$
$$G_j(u(\rho),\rho) \le 0\ with\ j = 1,....,m$$

The problem statement includes the following:

- An objective function $F(u(\rho),\rho)$. Even though each problem could have different objective functions, generally the most used one is minimizing compliance, or in another word, maximizing the stiffness of the structure.

- Main design variable: material distribution. Here material density at each point of the members $\rho(u)$ could be this variable. 1 represents the places where density is described, and 0 is for the places where the material is deleted or there is none. On the other hand, u defines if the state is linear or nonlinear [11].

- The design space $u(\rho)$. This points out how much volume exists in design. There are many design factors such as manufacturing and handling that should be taken into account in determination of this value. Once this value is determined, then no need to change these places in the optimization stage.

- m constraints is a characteristic that the solution must satisfy $Gj(u(\rho),\rho) \le 0$. The examples are the maximum amount of material to be distributed (volume constraint) or maximum stress values.

- Evaluating $u(\rho)$ often includes solving a differential equation. This is most commonly done using the finite element method since these equations do not have a known analytical solution [3].

2.2 Structural topology optimization

The topology of a structure is defined as a spatial arrangement of structural members and joints or internal boundaries. For both discrete and continuum structures, topology optimization helps to arrange association form of members as can be realized in **Figure 2** [18].

The conceptual process is shown in **Figure 3**.

Structural optimization is concerned with maximizing the utility of a fixed quantity of resources to fulfill a given objective. In structural optimization the best "structural" design is selected regarding three categories: size optimization, shape optimization, and topology optimization [19]. The application of topology optimization to structures to reveal the best position and size of the parts in a continuum is the most favorite one. Michell presented the first solutions as seen in **Figure 4**. Today much more advanced techniques are used, and by the help of finite element method, it could be applied to complex problems. Weight savings are managed by engineers in several structures as a consequence of utilization of these
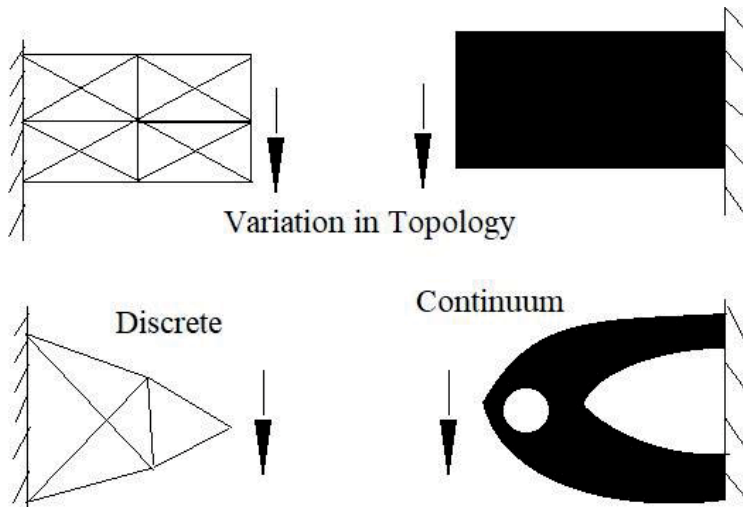
Figure 2.
Variation of topology [18].
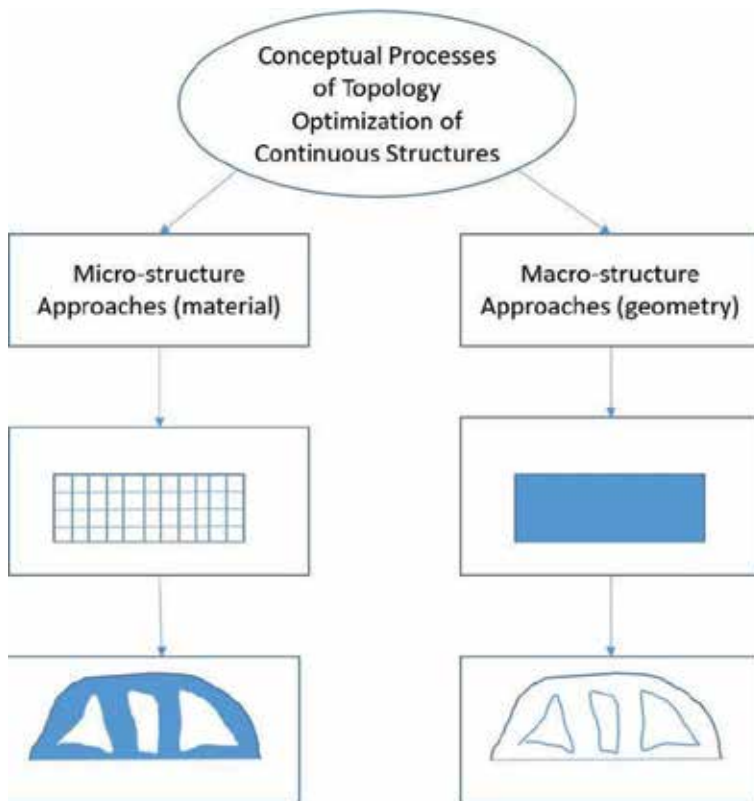
Figure 3.
Conceptual process [18].

methods. There are many examples in literature on the application of these methods [13, 20, 21]. Today, many commercial finite element software has an optimization module (Altair OptiStruct, Simulia Tosca, OPTISHAPE-TS, etc.) to obtain lighter
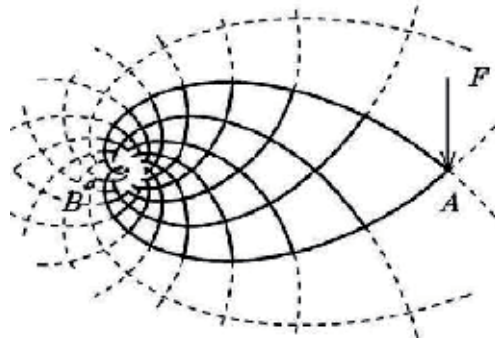
Figure 4.
One of the first proposed solutions to a structural topology optimization problem [13].
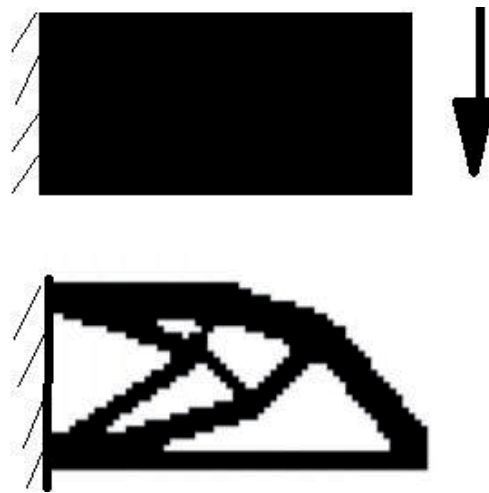
Figure 5.
Initial and optimized unit structure of a short cantilever.

structure, but several researchers have generated their codes [22, 23] or developed scripts [24] using these software's programming languages.

Structural optimization concerns on getting the required task of the mechanical system and maximizing its efficiency by an ordered procedure. At the beginning the design variables should be selected carefully. Then, limitations of these variables and system performance factors will be defined. By changing variable values, it is possible to see the change in these factors so we are able to determine the best combination among the design space. As design variables, the size of the members or mechanical properties of materials could be selected similar to size optimization, and the configuration of members is also another possible parameter as in shape optimization. Material distribution and layout are the parameter that is concerned in topology optimization. As the objective function, the most used one is cost function (related to total weight) to be minimized. Stress and buckling conditions are mostly used constraints in literature [18]. The aim is to optimize parts or units for specific load cases and extreme situations.

Figure 5 shows a sample application of topology optimization in finding the best material distribution. Minimizing objective function is acquired by checking different structure forms step by step. Each time design is narrowed down by selecting the best form among feasible sets.

3. Classification of methodologies

Topology optimization methods are mathematical techniques/approaches, and they can be programmed using different algorithms. These algorithms could be classified as follows: the criterion algorithm, the mathematical programming algorithm, and the intelligent algorithm.

The criterion algorithm obtains the optimality condition by the perceptual knowledge or the rational derivation. Result geometry will be gained by checking constraint violations and objective function value in an iterative way.

The perceptual criterion is usually the extension of the optimality condition of the full stress criterion of the size optimization. The rational criterion is derived usually by the Lagrange multiplier method of equality constraint. The ESO method is the typical criterion method.

Common mathematical programming algorithms like linear programming (LP) and nonlinear programming methods are also used in topology optimization of structures. The first attempts begin with using LP and successive LP methods later continued with sequential quadratic programming methods. Similar too criterion algorithm, mathematical programming algorithms are solved iteratively. Both stability and sensitivity of the structure are checked in each iteration. Of course it means that more calculation should be done for large-scale systems, and consequently low performance is observed for these cases. Fleury discussed the relationship between the criteria method and the mathematical programming method of size optimization. Fleury found that they both have given approximate results. This study refers still to the basics of the topology optimization [25, 26].

Genetic algorithm, simulated annealing algorithms, and particle swarm are the frequently used algorithms for topology optimization as the intelligent algorithm. The advantage of these algorithms is to keep it from too much calculations. The main idea is to search the optimum topology by checking only the objective function and constraints without calculating any gradients. On the contrary, solution speed can be slow, especially for large-scale system; finding optimum could take longer times [27, 28]. Several algorithms are also developed to combine topology optimization with additive manufacturing [29].

Two classes of approaches, the so-called material or micro-approaches and the geometrical or macro-approaches, are available [30, 31]. For the areas such as MEMS or biomaterial applications, classical continuum mechanics theories sometimes could not give accurate results. So, there are essential conceptual differences between these two types of approaches because of size effect.

Furthermore, another most commonly used classification merit of methodologies is if its discrete elements are used or not. The mainly used methods using discrete elements can be regarded, such as [18] ground structure approach (GSA) [21, 32], solid isotropic material with penalization (SIMP) method [33], homogenization method (HM) [34], evolutionary structural optimization (ESO) [35], and level-set method (LSM) [35]. On the other hand, the mainly used meshless methods are element-free Galerkin (EFG) [36], moving particle [37], and peridynamics [38]. Here, some of the studies post 2010 using these methodologies and their hybrids will be given under different headings.

3.1 Ground structure approach

Sokol and Rozvany [39] applied a hybrid method of linear programming and GSA to multi-load truss systems. Zhang et al. [40] combined GSA with simulated annealing to apply truss systems. Xu et al. [41] combined GSA with mixed integer

linear programming for topology optimization of tensegrity structures. Zhang et al. [42] compared two different ground structure approach (macroelement and macropatch) on a skyscraper and arch bridge. Chun et al. [43] used a discrete filtering scheme in which thin bars are eliminated during reliability-based topology optimization. Gao et al. [44] considered principal stress trajectories to find the suitable nodal points to decrease the computational cost in building ground structure. Ha and Guest [45] applied the method to find the optimum 3D woven material structure and, in a later study, with their colleagues tested this structure [46]. Kosaka et al. [47] applied hybrid method of GSA and ESO to frame structures. Ramos and Paulino [48] considered the materials' nonlinear behavior to solve several topology optimization benchmarking problems. Shakya et al. [49] combined particle swarm optimization (PSO) algorithm with GSA in order to detect and remove useless elements of truss systems. Sokol [50] used GSA in the optimization of large-scale pin-jointed frames considering a new member adding strategy. Wang and Zhang [51] proposed a new approach, parallel optimization tactic, in topology optimization of multi-material compliant mechanism. Zegard and Paulino provided a code for 2D [52] and 3D [53] domains to prevent creating members not intersecting with others. Zhang et al. [54] worked on arranging optimum structure of multi-material composite material using Zhang-Paulino-Ramos design variable update scheme with Karush-Kuhn-Tucker conditions. Zhang et al. [21] used a different filtering scheme for the optimization of multi-materials (hyperelastic Ogden-based and bilinear materials).

3.2 Solid isotropic material with penalization method

Shao [55] has combined BESO with SIMP considering 3D printing applications. Lógó [56] has solved a continuum-type topology optimization problem considering uncertainties in load positions. Garcia-Lopez et al. [57] combined simulated annealing with SIMP to eliminate gray areas resulted by SIMP. Gebremedhen et al. [58] used SIMP to solve 3D stress-constrained topology optimization problems. Jantos et al. [59] used a new approach based on thermodynamics material modeling and not containing any filter and compared the results with SIMPs'. Jiao et al. [60] combined ESO with SIMP and used strain energy in their filtering function as sensitivity number. Kandemir et al. [61] proposed a new approach to define intermediate densities (gray areas) with new penalization factor. Marck et al. [62] applied SIMP to solve a multiobjective conductivity problem while using finite volume method (FVM) to solve the energy equation. Ospald and Herzog [63] used projected gradient method with SIMP to solve the structure problem of mold where short-fiber-reinforced polymer material is used in injection molding. Qiao et al. [64] applied the hybrid method of SIMP and BESO to a MBB beam and a cantilever beam and compared the results with literature. Schlinquer et al. [65] applied SIMP to design a mechanism used to amplify the displacement of a piezoelectric actuators. Tsai and Cheng [66] employed SIMP to design flywheel rotor having maximum stiffness. Wang et al. [67] combined topology and size optimization for a folding wing structural design. Yang et al. [68] accomplished topology optimization of an electric vehicle body by SIMP. Yang et al. [69] used SIMP for topology optimization of a hard disk drive. Yunfei et al. [70] applied SIMP to design a robot's upper arm. Zhang and Ren [71] proposed a new optimality criterion method concerning minimum compliance. Zhang et al. [72] presented a new approach to control the length scale of structural members. Zhang et al. [73] presented a method for cellular structures with multiple types of microstructures. Zuo and Saitou [74] introduced power functions with scaling and translation coefficients and the cost properties for multiple materials.

3.3 Homogenization method

Allaire et al. applied HM to structures made of periodically perforated material in 2D [75] and 3D [76]. Zhang and Khandelwal [77] presented a nonlinear homogenization method to be able to design metamaterials. Lee et al. [78] proposed asymptotic homogenization method to solve topology optimization problem of magnetic composite materials. El-Kahlout and Kiziltas [79] used together MATLAB code to integrate material model derived using homogenization theory with COMSOL and solved several design problems where periodic dielectric materials with desired properties are aimed. Noguchi et al. [80] proposed a level-set-based topology optimization method for the design of hyperbolic acoustic metamaterials using a high-frequency homogenization method. Larsen et al. [81] proposed a new approach based on HM extracting discrete structure from the continuum model. Milani and Bruggi [82] used an adaptive meshing algorithm with HM to optimize multistory masonry wall loaded up to failure. Groen and Sigmund [83] presented a projection method to get better meshes during topology optimization. Xia and Breitkopf [84] implemented a MATLAB code which uses energy-based homogenization approach rather than the asymptotic approach. Bruggi and Milani [85] arranged strut-and-tie models in reinforced concrete structures. Kaminakis et al. [86] used hybrid algorithm based on evolutionary algorithms in the design of microstructures having auxetic behavior.

3.4 Evolutionary structural optimization

Martínez-Frutos and Herrero-Pérez [87] used evolutionary algorithm to increase the efficiency of GPU and enable to solve with smaller amount of device memory. Daróczy and Jármai [88] proposed a new bidirectional evolutionary structural optimization (BESO) algorithm based on fluid dynamics analogy. Tomšič and Duhovnik [89] discussed simultaneous topology and size optimization of trusses. Abdi et al. [90] used a combination of ESO with XFEM which uses isoline design approach. Ansola et al. [91] used ESO to optimize compliant mechanism under concentrated and thermal loads. Aulig and Olhofer [92] combined a neuro-evolution algorithm with a gradient-based optimizer and later proposed another algorithm considering state-based representation [93]. Azamirad and Arezoo [94] combined programming environment with Abaqus FEM software to optimize die components. Bureerat and Sriworamas [95] proposed multiobjective real-code population-based incremental learning (RPBIL) and a hybrid algorithm of RPBIL with differential evolution (DE) (termed RPBIL-DE) to solve water distribution network. Chen et al. [96] used ESO to optimize the rotary lobe of root vacuum pumps. Chen [97] used modified ESO algorithm for the optimization of plate structure under harmonic loading. Cho et al. [98] obtained optimum topology for the inner reinforcement of a vehicle's hood having uncertainties in variables. Finotto et al. [99] used an algorithm combination of ground structure approach, nonlinear finite element analysis, and quantum-inspired evolutionary algorithms. Garcia-Lopez et al. [100] used multiobjective evolutionary algorithm handling uncertainties and also giving the Pareto frontier solutions to let user select the best solution. Greiner and Hajela [101] used multiobjective evolutionary algorithm using reunification criterion to increase search efficiency. Huang and Xie [102] used BESO utilizing an alternative material interpolation scheme. Huang et al. [103] used BESO to optimize the topology of PBC made of two-phase composites. Zuo and Xie [104] used ESO letting limiting displacement. Jantos et al. [105] added a control mechanism for growth factor where at each step Lagrange multiplier is used to find optimum. Jia et al. [106] used hybrid of ESO with LSM. Kaminakis et al. [107]

proposed hybrid method of Particle Swarm Optimization and differential evolution in the design of microstructures. Kunakote and Bureerat [108] compared Pareto archive evolution strategy (PAES), population-based incremental learning (PBIL), non-dominated sorting genetic algorithm (NSGA), strength Pareto evolutionary algorithm (SPEA), and multiobjective particle swarm optimization (MPSO). Li et al. [109] used a combination of SIMP and ESO. Li et al. [110] used BESO method in the design of hinge-free compliant mechanisms. Maleki Jebeli and Shariat Panahi [111] used GA as evolutionary algorithm to optimize the material property distribution in FG structures. Okamoto et al. [112] enhanced genetic algorithm, immune algorithm, additional search in the restricted design space with enabling island, and void distribution during FEM analysis to solve a typical magnetic circuit problem. Picelli et al. [113] used BESO to free vibration problems of acoustic-structure systems. Riehl and Steinmann [114] employed the traction method to define descent directions for shape variation. Shi et al. [115] used APDL and UIDL to implement BESO in ANSYS to improve results. Sun et al. [116] applied BESO a cantilever composite laminate under uniform in-plane pressure. Tominaga et al. [117] used GA algorithms for magnetostatic shielding to minimize the magnetic flux intensity in a specified region. Wang et al. [118] used to optimize constrained damping layer structure. Fritzen et al. [119] taken nonlinear elastoviscoplastic microscopic RVE into account at all points of the macroscopic design domain by using BESO. Later, Xia et al. [120] introduced a damping scheme on sensitivity numbers to the same approach. Zhu et al. [121] used bidirectional evolutionary level-set method allowing automatic hole generation. Zuo et al. [27] enhanced the BESO method to multiple constraints of displacement and frequency in addition to the amount of material usage.

3.5 Level-set method (LSM)

Allaire et al. [122] applied LSM with enabling local mesh modifications. Chen and Chen [123] considered geometric uncertainty and related problems. Van Dijk et al. [124] used uses a direct steepest-descent update of the design variables in a LSM. Dunning and Alicia Kim [125] developed a third dimension for 2D problems to adjust new hole positions and to prevent violations with boundaries. Emmendoerfer and Fancello [126] minimized mass under stress constraints using an augmented Lagrangian approach. Gomes et al. [127] interested in the reduction of the design space dimension by the help of a GUI. Guo et al. [128] used LSM in stress-related topology optimization problems. Otomori et al. applied LSM to the design of electromagnetic cloaks using a ferrite material [129] and a light-scattering layer for solar cell applications [130]. Guo et al. [131] developed a local and explicit feature control scheme. James et al. [132] used isoparametric finite element, and James and Martins [133] used a body-fitted, nonuniform finite element mesh to overcome irregular shape problems. Jang et al. [134] considered geometric uncertainties in the production of microsystems. Lim et al. [135] applied to magnetic actuator design problems. Liu et al. [136] adopted extended finite element method (XFEM) with unified structural optimization model help to cover the topology, shape, and sizing optimization at the same time. Luo et al. [137] combined meshless Galerkin method with LSM. Makhija and Maute [138] applied a generalized Heaviside enrichment strategy with XFEM formulation. Mohamadian and Shojaee [139] combined binary level-set method and Merriman-Bence-Osher scheme. Otomori et al. [140] used LSM in the design of negative permeability dielectric metamaterials. Shojaee and Mohammadian [141] combined piecewise constant level-set (PCLS) method with a MBO scheme. Shu et al. [142] used LSM to minimize frequency response which results in the reduction in the vibration of structure.

Shu et al. [143] used LSM in the design of coupled structural-acoustic system with a focus on interior noise reduction. Suresh and Takalloozadeh [144] used LSM considering stress constraints. Xia et al. [145] used LSM to maximize the simple or repeated first eigenvalue of structure vibration. Xia et al. [146] built a strict 0–1 model considering stress to be minimized. Xia et al. [147] optimized both structure and support using traction free and Dirichlet boundaries separately. Yamasaki et al. [148] proposed a method combined application of boundary element mesh with LSM. Zhu and Zhang [149] used LSM without re-initialization for the optimization of compliant mechanisms. Zhu et al. [150] combined projection Lagrangian method with piecewise constant level-set functions to manage the optimization for elliptic boundary value problems. Zhu et al. [151] used LSM to optimize hinge-free compliant mechanisms with multiple outputs. Zhu and Zhang [152] developed an accelerated level-set evolution algorithm by adding an extra energy function to be able to optimize the distributed compliant mechanisms. Zhu et al. [153] developed a new LSM to manage multiobjective optimization of hinge-free compliant mechanisms.

3.6 Meshless methods

Lin et al. [154] generated a method mimicking leaf venation and using element-free Galerkin method to design heat conduction channels. Wang and Luo [155] proposed a meshless Galerkin level-set method using compactly supported radial basis functions to construct the meshless shape functions. Cui et al. [156] proposed a new method based on SIMP and using EFG method for multi-material optimization problems. Zhao [157] developed a new approach based on Pareto frontier solutions using EFG method. He et al. [158] combined density variable approach with EFG to optimize geometrically nonlinear structures. Evgrafov [159] proposed a method based on SIMP combined with Petrov-Galerkin methods based on minimizing the squared residual. Khan et al. [160] used EFG with LSM and also implemented sensitivity analysis. Gong et al. [161] developed a new method, particle moving, based on EFG considering density gradient and combined it with SIMP. Hur et al. [162] used a Spline-based meshfree method where nonuniform rational B-spline functions are used to smooth trimmed boundaries. Ren et al. [163] used a method combination of EFG and SIMP to design a two-material micro-compliant mechanism under stress constraints. Zhang et al. [164] applied a combined method of SIMP and direct coupling method of FE and EFG methods to decrease computational cost of meshless methods. Ai and Gao [165] integrated a parametric level-set method with a meshless method based on compactly supported radial basis functions. Wang et al. [166] applied EFG to the design of large displacement compliant mechanisms having geometrical nonlinearity. Yang et al. [167] applied EFG to the design of continuum structures under displacement constraints. Kefal et al. [38] combined BESO with a new meshless method peridynamics. Zheng et al. [168] used a combination of SIMP and EFG to optimize free vibrating continuum structures. Zhang et al. [169] used a directly coupled FE and EFG to optimize nonlinear hyperelastic structures. Luo et al. [36] used dual-level point-wise density approximation with EFG. Wu et al. [170] improved EFG by adding moving least squares approximation. Zheng et al. [171] used EFG to optimize geometrically nonlinear continuum structures. Zhao [172] combined BESO with EFG.

4. Emerging areas and recommendations

Sigmund and Maute [11] drawn a good framework on the classification of methodologies, and they pointed an important spot that differences between topology

optimization approaches become small and an approach evolves into the other by the time such as evolutionary methods are converging towards discrete SIMP schemes. However, this trend has gone forward using hybrid approaches rather than becoming similar techniques to keep all the approaches having their advantages and limitations. There are many studies using hybrid methodologies given before under different headings, but there is still room for new applications. Especially from evolutionary algorithms perspective, using new optimization algorithms will enable to improve methodologies advanced up to now.

Another important area to work on is how uncertainties are handled. Topology optimization of small sized systems brings researchers to the position where small changes should be taken into account as todays' technology is covering nano-sized systems beyond MEMS. In any case when changes are formed either because of manufacturing errors or that applied loads has caused comparatively large deformations on members, it will not be possible to use precise geometry and crisp size values in the optimization stage. So, handling uncertainties such as using fuzzy systems is still an open field to study.

Lastly, another rapidly growing area at the last decade is rapid prototyping. Even though there are abundant studies in literature (over a hundred studies could be easily found [173]), new algorithms on the application of BESO, handling composite/functionally graded materials, and considering support and structure in the meantime are the promising areas to study.

In addition to the aforementioned emerging areas, researchers are encouraged to study (1) to develop the efficiency of standard methods; (2) to construct new benchmarking problems; (3) to consider several constraints rather than buckling, stress, or displacement of such natural frequency; (4) to adapt meshes to nonlinear geometries with a more accurate way; (5) to develop GUIs to help researcher to observe/interfere the optimization stage; and (6) to implement new meshless methods rather than EFG such as peridynamics.

Author details

Aykut Kentli
Marmara University Engineering Faculty, Istanbul, Turkey

*Address all correspondence to: akentli@marmara.edu.tr

IntechOpen

References

[1] Zhu J, Gao T. Topology Optimization in Engineering Structure Design. London: ISTE Press - Elsevier; 2016

[2] Banichuk NV. Introduction to Optimization of Structures. New York: Springer Science & Business Media; 2013

[3] Querin OM, Victoria M, Gordoa CA, Ansola R, Martí P. Topology Design Methods for Structural Optimization. London: Academic Press; 2017

[4] Bujny M, Aulig N, Olhofer M, Duddeck F. Evolutionary Crashworthiness Topology Optimization of Thin-walled Structures. Munich, Germany: ASMO UK; 2016

[5] Zhang X, Zhu B. Topology Optimization of Compliant Mechanisms. Singapore: Springer; 2018

[6] Zargham S, Ward TA, Ramli R, Badruddin IA. Topology optimization: A review for structural designs under vibration problems. Structural and Multidisciplinary Optimization. 2016;**53**(6):1157-1177

[7] Eschenauer HA, Olhoff N. Topology optimization of continuum structures: A review. Applied Mechanics Reviews. 2001;**54**(4):331-390

[8] Huang X, Xie YM. A further review of ESO type methods for topology optimization. Structural and Multidisciplinary Optimization. 2010;**41**(5):671-683

[9] Munk DJ, Vio GA, Steven GP. Topology and shape optimization methods using evolutionary algorithms: A review. Structural and Multidisciplinary Optimization. 2015;**52**(3):613-631

[10] van Dijk NP, Maute K, Langelaar M, Van Keulen F. Level-set methods for

structural topology optimization: A review. Structural and Multidisciplinary Optimization. 2013;**48**(3):437-472

[11] Sigmund O, Maute K. Topology optimization approaches. Structural and Multidisciplinary Optimization. 2013;**48**(6):1031-1055

[12] Rozvany GI. A critical review of established methods of structural topology optimization. Structural and Multidisciplinary Optimization. 2009;**37**(3):217-237

[13] Kingman J, Tsavdaridis KD, Toropov VV. Applications of topology optimization in structural engineering: High-rise buildings and steel components. Jordan Journal of Civil Engineering,. Leeds; 2015;**159**(3097):1-23

[14] Bendsoe MP, Olhoff N, Sigmund O, editors. IUTAM Symposium on Topological Design Optimization of Structures, Machines and Materials: Status and Perspectives. Vol. 137. Netherlands: Springer Science & Business Media.; 2006

[15] Dassault Systems. Tosca structure: Optimize with ABAQUS, ANSYS, or MSC NASTRAN. 2019. Available from: https://www.3ds.com/productsservices/simulia/products/tosca/structure/topology-optimization/

[16] Bruggi M, Taliercio A. Topology optimization for the development of eco-efficient masonry units. In: Eco-Efficient Masonry Bricks and Blocks. Cambridge: Woodhead Publishing; 2015. pp. 425-445

[17] Dems K. First-and second-order shape sensitivity analysis of structures. Structural Optimization. 1991;**3**(2):79-88

[18] The Constructor: Civil Engineering Home. Topology Optimization of

Structures. 2019. Available from: https://theconstructor.org/structural-engg/topology-optimizationof-structures/5721/

[19] Bendsoe M, Sigmund O. Topology optimization: Theory, methods and applications. Berlin: Springer; 2003

[20] Jung D, Gea HC. Topology optimization of nonlinear structures. Finite Elements in Analysis and Design. 2004;**40**(11):1417-1427

[21] Zhang X, Ramos AS, Paulino GH. Material nonlinear topology optimization using the ground structure method with a discrete filtering scheme. Structural and Multidisciplinary Optimization. 2017;**55**(6):2045-2072

[22] Aage N, Andreassen E, Lazarov BS. Topology optimization using PETSc: An easy-to-use, fully parallel, open source topology optimization framework. Structural and Multidisciplinary Optimization. 2015;**51**(3):565-572

[23] Suresh K. A 199-line Matlab code for Pareto-optimal tracing in topology optimization. Structural and Multidisciplinary Optimization. 2010;**42**(5):665-679

[24] Bochenek B, Tajs-Zielińska K. GHOST—Gate to Hybrid Optimization of Structural Topologies. Materials. 2019;**12**(7):1152

[25] Atrek E. SHAPE: A structural shape optimization program. In: Software Systems for Structural Optimization. Basel: Birkhäuser; 1993. pp. 229-249

[26] Eschenauer HA, Geilen J, Wahl HJ. SAPOP. In: Software Systems for Structural Optimization. Basel: Birkhäuser; 1993. pp. 207-227

[27] Zuo ZH, Xie YM, Huang X. Evolutionary topology optimization of structures with multiple displacement and frequency constraints.

Advances in Structural Engineering. 2012;**15**(2):359-372

[28] Abdi M, Ashcroft I, Wildman R. Topology optimization of geometrically nonlinear structures using an evolutionary optimization method. Engineering Optimization. 2018;**50**(11):1850-1870

[29] Sigmund O, Clausen A, Groen JP, Wu J. Topology optimization of structures and infill for additive manufacturing. In: 1st ECCOMAS Thematic Conference on Simulation for Additive Manufacturing; Munich, Germany. 2017

[30] Li L. Topology optimization of structures with microstructural and elastoplastic-damage effects [PhD thesis]. University of Notre Dame; 2018

[31] Luo Y, Li Q, Liu S. A projection-based method for topology optimization of structures with graded surfaces. International Journal for Numerical Methods in Engineering. 2019;**118**(11):654-677

[32] Shieh RC. Massively parallel structural design using stochastic optimization and mixed neural net/finite element analysis methods. Computing Systems in Engineering. 1994;**5**(4-6):455-467

[33] Bendsøe MP. Optimal shape design as a material distribution problem. Structural Optimization. 1989;**1**(4):193-202

[34] Bendsøe MP, Kikuchi N. Generating optimal topologies in structural design using a homogenization method. Computer Methods in Applied Mechanics and Engineering. 1988;**71**(2):197-224

[35] Jiang C, Jia H. Evolutionary based intelligent algorithm for topology optimization of structure. In: Sixth International Conference on Intelligent

Systems Design and Applications. Vol. 1. California: IEEE; 2006. pp. 897-902

[36] Luo Z, Zhang N, Wang Y, Gao W. Topology optimization of structures using meshless density variable approximants. International Journal for Numerical Methods in Engineering. 2013;**93**(4):443-464

[37] Liu WK, Jun S, Li S, Adee J, Belytschko T. Reproducing kernel particle methods for structural dynamics. International Journal for Numerical Methods in Engineering. 1995;**38**(10):1655-1679

[38] Kefal A, Sohouli A, Oterkus E, Yildiz M, Suleman A. Topology optimization of cracked structures using peridynamics. Continuum Mechanics and Thermodynamics. 2019;**31**(6):1645-1672

[39] Sokół T, Rozvany GIN. On the adaptive ground structure approach for multi-load truss topology optimization. In: Tenth World Congress on Structural and Multidisciplinary Optimization, Orlando, FL. 2013. pp. 20-24

[40] Zhang XS, de Sturler E, Paulino GH. Stochastic sampling for deterministic structural topology optimization with many load cases: Density-based and ground structure approaches. Computer Methods in Applied Mechanics and Engineering. 2017;**325**:463-487

[41] Xu X, Wang Y, Luo Y. An improved multi-objective topology optimization approach for tensegrity structures. Advances in Structural Engineering. 2018;**21**(1):59-70

[42] Zhang X, Maheshwari S, Ramos AS Jr, Paulino GH. Macroelement and macropatch approaches to structural topology optimization using the ground structure method. Journal of Structural Engineering. 2016;**142**(11):04016090

[43] Chun J, Paulino GH, Song J. Reliability-based topology optimization by ground structure method employing a discrete filtering technique. Structural and Multidisciplinary Optimization. 2019;**60**(3):1035-1058

[44] Gao G, Liu ZY, Li YB, Qiao YF. A new method to generate the ground structure in truss topology optimization. Engineering Optimization. 2017;**49**(2):235-251

[45] Ha S, Guest JK. Topology optimization of 3D woven micro-lattices using a projection-based ground structure approach. In: 17th AIAA/ISSMO Multidisciplinary Analysis and Optimization Conference. 2016. p. 3214

[46] Ha SH, Lee HY, Hemker KJ, Guest JK. Topology optimization of three-dimensional woven materials using a ground structure design variable representation. Journal of Mechanical Design. 2019;**141**(6). DOI: 061403

[47] Kosaka K, Matsumoto S, Fujii D. Topology optimization of frame structures using ESO method and ground structure method. Journal of Structural and Construction Engineering. 2016;**81**(721):547-553

[48] Ramos AS, Paulino GH. Convex topology optimization for hyperelastic trusses based on the ground-structure approach. Structural and Multidisciplinary Optimization. 2015;**51**(2):287-304

[49] Shakya A, Nanakorn P, Petprakob W. A ground-structure-based representation with an element-removal algorithm for truss topology optimization. Structural and Multidisciplinary Optimization. 2018;**58**(2):657-675

[50] Sokół T. Topology optimization of large-scale trusses using ground structure approach with selective subsets of active bars. In: 19th

International Conference on Computer Methods in Mechanics (CMM), Warsaw, Poland. 2011. pp. 9-12

[51] Wang N, Zhang X. Multi-material topology optimization of complaint mechanism using ground structure approach. In: 2014 International Conference on Manipulation, Manufacturing and Measurement on the Nanoscale (3M-NANO). New York: IEEE; 2014. pp. 249-254

[52] Zegard T, Paulino GH. GRAND—Ground structure based topology optimization for arbitrary 2D domains using MATLAB. Structural and Multidisciplinary Optimization. 2014;**50**(5):861-882

[53] Zegard T, Paulino GH. GRAND3—Ground structure based topology optimization for arbitrary 3D domains using MATLAB. Structural and Multidisciplinary Optimization. 2015;**52**(6):1161-1184

[54] Zhang XS, Paulino GH, Ramos AS Jr. Multimaterial topology optimization with multiple volume constraints: Combining the ZPR update with a ground-structure algorithm to select a single material per overlapping set. International Journal for Numerical Methods in Engineering. 2018;**114**(10):1053-1073

[55] Shao G. Comparison of BESO and SIMP to do structural topology optimization in discrete digital design, and then combine them into a hybrid method. In: The International Conference on Computational Design and Robotic Fabrication. Singapore: Springer; 2019. pp. 199-209

[56] Lógó J. SIMP type topology optimization procedure considering uncertain load position. Periodica Polytechnica Civil Engineering. 2012;**56**(2):213-219

[57] Garcia-Lopez NP, Sanchez-Silva M, Medaglia AL, Chateauneuf A. A hybrid topology optimization methodology combining simulated annealing and SIMP. Computers & Structures. 2011;**89**(15-16):1512-1522

[58] Gebremedhen HS, Woldemicahel DE, Hashim FM. Three-dimensional stress-based topology optimization using SIMP method. International Journal for Simulation and Multidisciplinary Design Optimization. 2019;**10**:A1

[59] Jantos DR, Riedel C, Hackl K, Junker P. Comparison of thermodynamic topology optimization with SIMP. Continuum Mechanics and Thermo-dynamics. 2019;**31**(2):521-548

[60] Jiao H, Zhou Q, Fan S, Li Y. A new hybrid topology optimization method coupling ESO and SIMP method. In: Proceedings of China Modern Logistics Engineering. Berlin, Heidelberg: Springer; 2015. pp. 373-384

[61] Kandemir V, Dogan O, Yaman U. Topology optimization of 2.5 D parts using the SIMP method with a variable thickness approach. Procedia Manufacturing. 2018;**17**:29-36

[62] Marck G, Nemer M, Harion JL, Russeil S, Bougeard D. Topology optimization using the SIMP method for multiobjective conductive problems. Numerical Heat Transfer, Part B: Fundamentals. 2012;**61**(6):439-470

[63] Ospald F, Herzog R. SIMP based topology optimization for injection molding of SFRPs. In: World Congress of Structural and Multidisciplinary Optimisation. Cham: Springer; 2017. pp. 850-861

[64] Qiao H, Wang S, Zhao T, Tang H. Topology optimization for lightweight cellular material and structure simultaneously by combining SIMP with BESO. Journal of Mechanical Science and Technology. 2019;**33**(2):729-739

[65] Schlinquer T, Mohand-Ousaid A, Rakotondrabe M. Displacement amplifier mechanism for piezoelectric actuators design using SIMP topology optimization approach. In: 2018 IEEE International Conference on Robotics and Automation (ICRA). New Jersey: IEEE; 2018. pp. 1-7

[66] Tsai TD, Cheng CC. Topology optimization of flywheel rotors using SIMP method: A preliminary study. In: Advanced Materials Research. Vol. 579. Switzerland: Trans Tech Publications; 2012. pp. 427-434

[67] Wang X, Lin Z, Xia R. SIMP based topology optimization of a folding wing with mixed design variables. In: Proceedings of the 2013 IEEE 17th International Conference on Computer Supported Cooperative Work in Design (CSCWD). New Jersey: IEEE; 2013. pp. 417-421

[68] Yang S, Qi C, Hu P, Wei ZY, Wang YL. Topology optimization of electric vehicle body in white based on SIMP method. In: Advanced Materials Research. Vol. 308. Switzerland: Trans Tech Publications; 2011. pp. 606-609

[69] Yang SY, Li H, Ou YB. Topology optimization of suspension of the hard disk drive based on SIMP method. In: Advanced Materials Research. Vol. 819. Switzerland: Trans Tech Publications; 2013. pp. 356-361

[70] Yunfei B, Ming C, Yongyao L. Structural topology optimization for a robot upper arm based on SIMP method. In: Advances in Reconfigurable Mechanisms and Robots II. Cham: Springer; 2016. pp. 725-733

[71] Zhang H, Ren XH. Topology optimization of continuum structures based on SIMP. In: Advanced Materials Research. Switzerland: Trans Tech Publications; 2011. pp. 255, 14-219

[72] Zhang W, Zhong W, Guo X. An explicit length scale control approach in SIMP-based topology optimization. Computer Methods in Applied Mechanics and Engineering. 2014;**282**:71-86

[73] Zhang Y, Xiao M, Li H, Gao L, Chu S. Multiscale concurrent topology optimization for cellular structures with multiple microstructures based on ordered SIMP interpolation. Computational Materials Science. 2018;**155**:74-91

[74] Zuo W, Saitou K. Multi-material topology optimization using ordered SIMP interpolation. Structural and Multidisciplinary Optimization. 2017;**55**(2):477-491

[75] Allaire G, Geoffroy-Donders P, Pantz O. Topology optimization of modulated and oriented periodic microstructures by the homogenization method. Computers & Mathematics with Applications. 2019;**78**(7):2197-2229

[76] Geoffroy-Donders P, Allaire G, Pantz O. 3-d topology optimization of modulated and oriented periodic microstructures by the homogenization method. Journal of Computational Physics. 2019;**401**:108994

[77] Zhang G, Khandelwal K. Computational design of finite strain auxetic metamaterials via topology optimization and nonlinear homogenization. Computer Methods in Applied Mechanics and Engineering. 2019;**356**:490-527

[78] Lee J, Yoo J, Min S, Yoon M. Topology optimization of anisotropic magnetic composites in actuators using homogenization design method. Structural and Multidisciplinary Optimization. 2019;**60**(4):1423-1436

[79] El-Kahlout Y, Kiziltas G. Inverse synthesis of electromagnetic materials

using homogenization based topology optimization. Progress in Electromagnetics Research. 2011;**115**:343-380

[80] Noguchi Y, Yamada T, Izui K, Nishiwaki S. Topology optimization for hyperbolic acoustic metamaterials using a high-frequency homogenization method. Computer Methods in Applied Mechanics and Engineering. 2018;**335**:419-471

[81] Larsen SD, Sigmund O, Groen JP. Optimal truss and frame design from projected homogenization-based topology optimization. Structural and Multidisciplinary Optimization. 2018;**57**(4):1461-1474

[82] Milani G, Bruggi M. Simple homogenization-topology optimization approach for the pushover analysis of masonry walls. International Journal of Architectural Heritage. 2018;**12**(3):395-408

[83] Groen JP, Sigmund O. Homogenization-based topology optimization for high-resolution manufacturable microstructures. International Journal for Numerical Methods in Engineering. 2018;**113**(8):1148-1163

[84] Xia L, Breitkopf P. Design of materials using topology optimization and energy-based homogenization approach in Matlab. Structural and Multidisciplinary Optimization. 2015;**52**(6):1229-1241

[85] Bruggi M, Milani G. Optimal FRP reinforcement of masonry walls out-of-plane loaded: A combined homogenization-topology optimization approach complying with masonry strength domain. Computers & Structures. 2015;**153**:49-74

[86] Kaminakis NT, Drosopoulos GA, Stavroulakis GE. Design and verification of auxetic microstructures using topology optimization and homogenization. Archive of Applied Mechanics. 2015;**85**(9-10):1289-1306

[87] Martínez-Frutos J, Herrero-Pérez D. GPU acceleration for evolutionary topology optimization of continuum structures using isosurfaces. Computers & Structures. 2017;**182**:119-136

[88] Daróczy L, Jármai K. From a quasi-static fluid-based evolutionary topology optimization to a generalization of BESO. Engineering Optimization. 2015;**47**(5):689-705

[89] Tomšič P, Duhovnik J. Simultaneous topology and size optimization of 2D and 3D trusses using evolutionary structural optimization with regard to commonly used topologies. Advances in Mechanical Engineering. 2014;**6**:864807

[90] Abdi M, Wildman R, Ashcroft I. Evolutionary topology optimization using the extended finite element method and isolines. Engineering Optimization. 2014;**46**(5):628-647

[91] Ansola R, Veguería E, Canales J, Alonso C. Electro-thermal compliant mechanisms design by an evolutionary topology optimization method. Engineering Computations. 2013;**30**(7):961-981

[92] Aulig N, Olhofer M. Neuro-evolutionary topology optimization of structures by utilizing local state features. In: Proceedings of the 2014 Annual Conference on Genetic and Evolutionary Computation. New York: ACM; 2014. pp. 967-974

[93] Aulig N, Olhofer M. State-based representation for structural topology optimization and application to crashworthiness. In: 2016 IEEE Congress on Evolutionary Computation (CEC). New Jersey: IEEE; 2016. pp. 1642-1649

[94] Azamirad G, Arezoo B. Topology optimization of stamping die components using evolutionary structural optimization method. Proceedings of the Institution of Mechanical Engineers, Part B: Journal of Engineering Manufacture. 2017;**231**(4):690-698

[95] Bureerat S, Sriworamas K. Simultaneous topology and sizing optimization of a water distribution network using a hybrid multiobjective evolutionary algorithm. Applied Soft Computing. 2013;**13**(8):3693-3702

[96] Chen XM, Lai XD, Zhang X, Zhou X. Evolutionary topology optimization design of rotary lobe of roots vacuum pumps. In: Advanced Materials Research. Vol. 798. Switzerland: Trans Tech Publications; 2013. pp. 365-368

[97] Chen LY. Structural-acoustic topology analysis based on evolutionary structural optimization. In: Applied Mechanics and Materials. Vol. 575. Switzerland: Trans Tech Publications; 2014. pp. 343-349

[98] Cho KH, Park JY, Ryu SP, Han SY. Reliability-based topology optimization based on bidirectional evolutionary structural optimization using multi-objective sensitivity numbers. International Journal of Automotive Technology. 2011;**12**(6):849-856

[99] Finotto VC, Lucena DS, da Silva WL, Valášek M. Quantum-inspired evolutionary algorithm for topology optimization of modular cabled-trusses. Mechanics of Advanced Materials and Structures. 2015;**22**(8):670-680

[100] Garcia-Lopez NP, Sanchez-Silva M, Medaglia AL, Chateauneuf A. An improved robust topology optimization approach using multiobjective evolutionary algorithms. Computers & Structures. 2013;**125**:1-10

[101] Greiner D, Hajela P. Truss topology optimization for mass and reliability considerations—Co-evolutionary multiobjective formulations. Structural and Multidisciplinary Optimization. 2012;**45**(4):589-613

[102] Huang X, Xie YM. Evolutionary topology optimization of continuum structures including design-dependent self-weight loads. Finite Elements in Analysis and Design. 2011;**47**(8):942-948

[103] Huang X, Xie YM, Jia B, Li Q, Zhou SW. Evolutionary topology optimization of periodic composites for extremal magnetic permeability and electrical permittivity. Structural and Multidisciplinary Optimization. 2012;**46**(3):385-398

[104] Zuo ZH, Xie YM. Evolutionary topology optimization of continuum structures with a global displacement control. Computer-Aided Design. 2014;**56**:58-67

[105] Jantos DR, Junker P, Hackl K. An evolutionary topology optimization approach with variationally controlled growth. Computer Methods in Applied Mechanics and Engineering. 2016;**310**:780-801

[106] Jia H, Beom HG, Wang Y, Lin S, Liu B. Evolutionary level set method for structural topology optimization. Computers & Structures. 2011;**89**(5-6):445-454

[107] Kaminakis NT, Stavroulakis GE. Topology optimization for compliant mechanisms, using evolutionary-hybrid algorithms and application to the design of auxetic materials. Composites Part B: Engineering. 2012;**43**(6):2655-2668

[108] Kunakote T, Bureerat S. Multi-objective topology optimization using evolutionary algorithms. Engineering Optimization. 2011;**43**(5):541-557

[109] Li YD, Kuang B, Liu J. SIMP-based evolutionary structural optimization method for topology optimization. In: Applied Mechanics and Materials. Vol. 651. Switzerland: Trans Tech Publications; 2014. pp. 2237-2240

[110] Li Y, Huang X, Xie YM, Zhou SW. Evolutionary topology optimization of hinge-free compliant mechanisms. International Journal of Mechanical Sciences. 2014;**86**:69-75

[111] Maleki Jebeli S, Shariat Panahi M. An evolutionary approach for simultaneous optimization of material property distribution and topology of FG structures. Engineering Computations. 2015;**32**(2):234-257

[112] Okamoto Y, Tominaga Y, Wakao S, Sato S. Topology optimization of magnetostatic shielding using multistep evolutionary algorithms with additional searches in a restricted design space. The International Journal for Computation and Mathematics in Electrical and Electronic Engineering. 2014;**33**(3): 894-913

[113] Picelli R, Vicente WM, Pavanello R, Xie YM. Evolutionary topology optimization for natural frequency maximization problems considering acoustic–structure interaction. Finite Elements in Analysis and Design. 2015;**106**:56-64

[114] Riehl S, Steinmann P. A staggered approach to shape and topology optimization using the traction method and an evolutionary-type advancing front algorithm. Computer Methods in Applied Mechanics and Engineering. 2015;**287**:1-30

[115] Shi DY, Han JS, Kong LC, Lin L. Research on evolutionary topology optimization in ANSYS. In: Key Engineering Materials. Vol. 572. Switzerland: Trans Tech Publications; 2014. pp. 547-550

[116] Sun XF, Yang J, Xie YM, Huang X, Zuo ZH. Topology optimization of composite structure using bi-directional evolutionary structural optimization method. Procedia Engineering. 2011;**14**:2980-2985

[117] Tominaga Y, Okamoto Y, Wakao S, Sato S. Binary-based topology optimization of magnetostatic shielding by a hybrid evolutionary algorithm combining genetic algorithm and extended compact genetic algorithm. IEEE Transactions on Magnetics. 2013;**49**(5):2093-2096

[118] Wang BQ, Wang BL, Huang ZY. Topology optimization for constrained layer damping plates using evolutionary structural optimization method. In: Advanced Materials Research. Vol. 894. Switzerland: Trans Tech Publications; 2014. pp. 158-162

[119] Fritzen F, Xia L, Leuschner M, Breitkopf P. Topology optimization of multiscale elastoviscoplastic structures. International Journal for Numerical Methods in Engineering. 2016;**106**(6):430-453

[120] Xia L, Fritzen F, Breitkopf P. Evolutionary topology optimization of elastoplastic structures. Structural and Multidisciplinary Optimization. 2017;**55**(2):569-581

[121] Zhu B, Zhang X, Fatikow S, Wang N. Bi-directional evolutionary level set method for topology optimization. Engineering Optimization. 2015;**47**(3):390-406

[122] Allaire G, Dapogny C, Frey P. A mesh evolution algorithm based on the level set method for geometry and topology optimization. Structural and Multidisciplinary Optimization. 2013;**48**(4):711-715

[123] Chen S, Chen W. A new level-set based approach to shape and topology optimization under

geometric uncertainty. Structural and Multidisciplinary Optimization. 2011;**44**(1):1-18

[124] Van Dijk NP, Langelaar M, Van Keulen F. Explicit level-set-based topology optimization using an exact Heaviside function and consistent sensitivity analysis. International Journal for Numerical Methods in Engineering. 2012;**91**(1):67-97

[125] Dunning PD, Alicia Kim H. A new hole insertion method for level set based structural topology optimization. International Journal for Numerical Methods in Engineering. 2013;**93**(1):118-134

[126] Emmendoerfer H Jr, Fancello EA. A level set approach for topology optimization with local stress constraints. International Journal for Numerical Methods in Engineering. 2014;**99**(2):129-156

[127] Gomes MA, Henriques B, Couto M, Carvalho A. A new tool for topology optimization with gradient-guided spectral level set methodology. In: 52nd AIAA/ASME/ASCE/AHS/ASC Structures, Structural Dynamics and Materials Conference 19th AIAA/ASME/AHS Adaptive Structures Conference 13t. 2011. p. 2092

[128] Guo X, Zhang WS, Wang MY, Wei P. Stress-related topology optimization via level set approach. Computer Methods in Applied Mechanics and Engineering. 2011;**200**(47-48):3439-3452

[129] Otomori M, Yamada T, Andkjær J, Izui K, Nishiwaki S, Kogiso N. Level set-based topology optimization for the design of an electromagnetic cloak with ferrite material. IEEE Transactions on Magnetics. 2013;**49**(5):2081-2084

[130] Otomori M, Yamada T, Izui K, Nishiwaki S, Kogiso N. Level

set-based topology optimization for the design of light-trapping structures. IEEE Transactions on Magnetics. 2014;**50**(2):729-732

[131] Guo X, Zhang W, Zhong W. Explicit feature control in structural topology optimization via level set method. Computer Methods in Applied Mechanics and Engineering. 2014;**272**:354-378

[132] James KA, Lee E, Martins JR. Stress-based topology optimization using an isoparametric level set method. Finite Elements in Analysis and Design. 2012;**58**:20-30

[133] James KA, Martins JR. An isoparametric approach to level set topology optimization using a body-fitted finite-element mesh. Computers & Structures. 2012;**90**:97-106

[134] Jang GW, van Dijk NP, van Keulen F. Topology optimization of MEMS considering etching uncertainties using the level-set method. International Journal for Numerical Methods in Engineering. 2012;**92**(6):571-588

[135] Lim S, Yamada T, Min S, Nishiwaki S. Topology optimization of a magnetic actuator based on a level set and phase-field approach. IEEE Transactions on Magnetics. 2011;**47**(5):1318-1321

[136] Liu T, Wang S, Li B, Gao L. A level-set-based topology and shape optimization method for continuum structure under geometric constraints. Structural and Multidisciplinary Optimization. 2014;**50**(2):253-273

[137] Luo Z, Zhang N, Gao W, Ma H. Structural shape and topology optimization using a meshless Galerkin level set method. International Journal for Numerical Methods in Engineering. 2012;**90**(3):369-389

[138] Makhija D, Maute K. Numerical instabilities in level set topology optimization with the extended finite element method. Structural and Multidisciplinary Optimization. 2014;**49**(2):185-197

[139] Mohamadian M, Shojaee S. Binary level set method for structural topology optimization with MBO type of projection. International Journal for Numerical Methods in Engineering. 2012;**89**(5):658-670

[140] Otomori M, Yamada T, Izui K, Nishiwaki S, Andkjær J. A topology optimization method based on the level set method for the design of negative permeability dielectric metamaterials. Computer Methods in Applied Mechanics and Engineering. 2012;**237**:192-211

[141] Shojaee S, Mohammadian M. Piecewise constant level set method for structural topology optimization with MBO type of projection. Structural and Multidisciplinary Optimization. 2011;**44**(4):455-469

[142] Shu L, Wang MY, Fang Z, Ma Z, Wei P. Level set based structural topology optimization for minimizing frequency response. Journal of Sound and Vibration. 2011;**330**(24):5820-5834

[143] Shu L, Wang MY, Ma Z. Level set based topology optimization of vibrating structures for coupled acoustic–structural dynamics. Computers & Structures. 2014;**132**:34-42

[144] Suresh K, Takalloozadeh M. Stress-constrained topology optimization: A topological level-set approach. Structural and Multidisciplinary Optimization. 2013;**48**(2):295-309

[145] Xia Q, Shi T, Wang MY. A level set based shape and topology optimization method for maximizing

the simple or repeated first eigenvalue of structure vibration. Structural and Multidisciplinary Optimization. 2011;**43**(4):473-485

[146] Xia Q, Shi T, Liu S, Wang MY. A level set solution to the stress-based structural shape and topology optimization. Computers & Structures. 2012;**90**:55-64

[147] Xia Q, Wang MY, Shi T. A level set method for shape and topology optimization of both structure and support of continuum structures. Computer Methods in Applied Mechanics and Engineering. 2014;**272**:340-353

[148] Yamasaki S, Yamada T, Matsumoto T. An immersed boundary element method for level-set based topology optimization. International Journal for Numerical Methods in Engineering. 2013;**93**(9):960-988

[149] Zhu BL, Zhang XM. Topology optimization of compliant mechanisms using level set method without re-initialization. In: Applied Mechanics and Materials. Vol. 130. Switzerland: Trans Tech Publications; 2012. pp. 3076-3082

[150] Zhu S, Wu Q, Liu C. Shape and topology optimization for elliptic boundary value problems using a piecewise constant level set method. Applied Numerical Mathematics. 2011;**61**(6):752-767

[151] Zhu B, Zhang X, Wang N. Topology optimization of hinge-free compliant mechanisms with multiple outputs using level set method. Structural and Multidisciplinary Optimization. 2013;**47**(5):659-672

[152] Zhu B, Zhang X. A new level set method for topology optimization of distributed compliant mechanisms. International Journal for Numerical

Methods in Engineering. 2012;**91**(8):843-871

[153] Zhu B, Zhang X, Wang N, Fatikow S. Topology optimization of hinge-free compliant mechanisms using level set methods. Engineering Optimization. 2014;**46**(5):580-605

[154] Lin Q, Wang J, Hong J, Liu Z, Wang Z. A biomimetic generative optimization design for conductive heat transfer based on element-free Galerkin method. International Communications in Heat and Mass Transfer. 2019;**100**:67-72

[155] Wang Y, Luo Z. A meshless level set method for shape and topology optimization. In: Advanced Materials Research. Vol. 308. Switzerland: Trans Tech Publications; 2011. pp. 1046-1049

[156] Cui M, Chen H, Zhou J, Wang F. A meshless method for multi-material topology optimization based on the alternating active-phase algorithm. Engineering with Computers. 2017;**33**(4):871-884

[157] Zhao F. A meshless Pareto-optimal method for topology optimization. Engineering Analysis with Boundary Elements. 2013;**37**(12):1625-1631

[158] He Q, Kang Z, Wang Y. A topology optimization method for geometrically nonlinear structures with meshless analysis and independent density field interpolation. Computational Mechanics. 2014;**54**(3):629-644

[159] Evgrafov A. Discontinuous Petrov-Galerkin methods for topology optimization. In: International Conference on Engineering Optimization. Cham: Springer; 2018. pp. 260-271

[160] Khan W, Islam S, Ullah B. Structural optimization based on meshless element free Galerkin and level set methods. Computer Methods

in Applied Mechanics and Engineering. 2019;**344**:144-163

[161] Gong SG, Wei YB, Xie GL, Zhang JP. Study on topology optimization method of particle moving based on element-free Galerkin method. International Journal for Computational Methods in Engineering Science and Mechanics. 2018;**19**(5):305-313

[162] Hur J, Kang P, Youn SK. Topology optimization based on spline-based meshfree method using topological derivatives. Journal of Mechanical Science and Technology. 2017;**31**(5):2423-2431

[163] Ren L, Yang R, Zhang W. Topology optimization design for two-material micro compliant mechanism with stress constraint. In: 2011 Second International Conference on Mechanic Automation and Control Engineering. New Jersey: IEEE; 2011, July. pp. 1843-1846

[164] Zhang Y, Ge W, Zhang Y, Zhao Z. Topology optimization method with direct coupled finite element–element-free Galerkin method. Advances in Engineering Software. 2018;**115**:217-229

[165] Ai L, Gao XL. Topology optimization of 2-D mechanical metamaterials using a parametric level set method combined with a meshfree algorithm. Composite Structures. 2019;**229**:111318

[166] Wang Y, Luo Z, Wu J, Zhang N. Topology optimization of compliant mechanisms using element-free Galerkin method. Advances in Engineering Software. 2015;**85**:61-72

[167] Yang X, Zheng J, Long S. Topology optimization of continuum structures with displacement constraints based on meshless method. International Journal of Mechanics and Materials in Design. 2017;**13**(2):311-320

[168] Zheng J, Long S, Li G. Topology optimization of free vibrating continuum structures based on the element free Galerkin method. Structural and Multidisciplinary Optimization. 2012;**45**(1):119-127

[169] Zhang Y, Ge W, Zhang Y, Zhao Z, Zhang J. Topology optimization of hyperelastic structure based on a directly coupled finite element and element-free Galerkin method. Advances in Engineering Software. 2018;**123**:25-37

[170] Wu Y, Ma YQ, Feng W, Cheng YM. Topology optimization using the improved element-free Galerkin method for elasticity. Chinese Physics B. 2017;**26**(8):080203

[171] Zheng J, Yang X, Long S. Topology optimization with geometrically non-linear based on the element free Galerkin method. International Journal of Mechanics and Materials in Design. 2015;**11**(3):231-241

[172] Zhao F. Topology optimization with meshless density variable approximations and BESO method. Computer-Aided Design. 2014;**56**:1-10

[173] Liu J, Gaynor AT, Chen S, Kang Z, Suresh K, Takezawa A, et al. Current and future trends in topology optimization for additive manufacturing. Structural and Multidisciplinary Optimization. 2018;**57**(6):2457-2483

Light-Weight Structures: Proposals of Resource-Saving Supporting Structures

Chichulina Kseniia and Chichulin Viktor

Abstract

The article will present resource-saving constructions and nodes of steel beams with a double profiled trapezoidal wall with intermittent weld seams, welded t-zones, t-zones from rolling, roll-formed channels, filling between the walls with polystyrene foam with diagonal and cross-lattice, a lattice in the form arched elements and single arched element; steel beams with a single transversally profiled wall of sinusoidal and trapezoidal outline with channel belts; resource-saving combined steel structures of frames and arches; assembly units of steel frames with spatial elements of square and round pipes. It is determined that the corrugation provides a reduction in material consumption, and the use of profiled sheets allows you to vary the size of corrugations, leads to a significant loss of weight of the structure under the condition of strength and stability. The advantages of the proposed resource-saving combined structures, namely: saving construction height (at the same time performs the function of the enclosing structure), transport and installation costs, there is no need to install transverse ribs (except in support areas and areas of concentration of significant loads), the emergence of opportunities for the use of modern technological equipment, a wide variety of applications, esthetics and many other advantages.

Keywords: beams, profiled trapezoidal wall, truss, arch, closed profiles, light steel structures, composite structures

1. Introduction

In the conditions of modern construction, the reduction of material consumption with simultaneous increase in reliability and ensuring favorable indicators of economic efficiency is one of the priorities of designers. The main of the many ways to improve the efficiency of construction is the development and improvement of new progressive lightweight structural forms, which significantly improve the technical and economic performance. Recently, a large popularization received various combined systems, which include elements of different stress-strain state. Research of new constructive forms with application of progressive technologies and materials, new algorithms of calculation by numerical methods opened ways of wide distribution of the combined systems abroad. Robot welding line gave the possibility of making resource-saving structures with corrugated walls (beams, columns, arches) and complex light metal structures made of profile pipes an alternative to traditional

constructive solution. A comprehensive solution to this problem requires the development of new resource-efficient designs. With the aim of developing constructive solutions resource consuming structures presents a series resource consuming constructive solutions. The use of such solutions leads to a significant reduction in material consumption with sufficient performance indicators. The light beams can be used in truss structures of beam cages and other beam structures in the construction of residential and public buildings, attics, superstructures, hangars and extensions.

Theoretical and experimental studies of steel beams with corrugated walls are presented in scientific papers [1–3]. In [1] it is noted that in recent years light profiled steel beams (CWSBs) are gaining increasing popularity. The bearing capacity of such structures is lower than the beams with a flat wall and trusses. The existence of three types of failures, namely local, General and mixed, is determined on the basis of experimental studies. Let us consider in detail the results of nonlinear finite element analysis. It is revealed that the shear stress is at the maximum and the same throughout the wall until swelling. Also experimental beams had a margin of carrying capacity, about half of the limit. In the course of the analysis it is proved that the shear stress is the same throughout the low-profile wall and has a maximum value. The authors confirmed the feasibility of using 1993-1-5 for beams with corrugated wall. In [2] the authors consider the theory of stocky beams and propose a new method of nodal lines. This method applies to thin-walled or thick-walled stocky beams. The paper presents the results of solving the problem of delay shift box girder of different thickness. Also, the values of the normal stress of the box beam due to the restrained torsion are obtained. As a result of the research, the authors obtained the values of shear stresses of the box beam due to shear forces. The results of mathematical modeling of transverse shear effect for sandwich beams with sinusoidal corrugated cores are presented in [3]. The authors studied the bending and bending of two sandwich beams, identified trends and the main problem points, presented theoretical models. The possibilities of influence of transverse shear effect on deflections and critical loads of such structures are shown. The results were confirmed by numerical analysis. The main advantages of truss structures are presented. The author's approaches to the variability of use and layout of farms are presented in [4]. In [5] the authors investigate tabular structures. The article calculates the optimal size of the welded tubular truss, analyzes the structural constraints, especially on the strength, stress elements, and geometric parameters of the nodes of the trusses. This optimization makes it possible to notice that the optimal height is determined by a geometric restriction that prescribes the minimum angle of inclination of the diagonals. The authors have calculated the cost parameters of such structures. After comparing the costs of a reinforced pipe and a larger pipe, it was found that the cost of the first is much lower. In work [6] it is noted that in the conditions of modern construction the metal frame becomes gaining popularity and has an esthetic appearance, safe connections, an opportunity to reduce sections of elements, belongs to fast-built designs. The authors highlighted the advantages and disadvantages of aluminum and steel, the analysis of the cost of these materials. Patent developments closest on design features are presented in [7–9]. In [7] represented Beam I-section with a corrugated wall comprising a shelf and welded to them a wall of corrugated metal sheet with a transverse arrangement of corrugations of arbitrary shape, characterized in that the wall consists of two or more parallel connected corrugated sheets, and the shelves are made of steel-concrete, consisting of rigid reinforcement in the form of corrugated sheet metal and reinforcement cage, including longitudinal reinforcement and transverse reinforcement, which embraces the longitudinal reinforcement, connected to it, its ends with a bend inside are welded to a corrugated sheet of metal with a space from the beam wall. In [8] the authors developed a metal beam with a corrugated wall comprising a belt connected

to each other by a corrugated wall with a transverse arrangement of the corrugations by welding, characterized in that it is provided with angles arranged in pairs in the center of the belts parallel to their longitudinal axes, with the outer surfaces of the shelves of the corners are rotated to each other and welded straight weld with a gap between the shelves sufficient to install the corrugated wall, which is fixed by means of an adhesive composition. The beam with a corrugated asymmetric profile wall [9] contains a compressed and stretched belt and wall. The wall, at least in some areas, is traditionally or variably corrugated with transverse corrugations. The profile of the corrugations is asymmetric with respect to the plane passing through the top of the corrugation and normal to the longitudinal axis.

2. Proposals of resource-efficient beam structures of buildings

In General, this section is aimed at presenting improved structural forms of resource—economic beams, arches, trusses, the introduction of which will give a significant economic effect, high characteristics of bearing capacity and architectural expressiveness, minimize material and labor costs and provide the possibility of using modern technological equipment of the European level, a wide range of applications in construction, esthetics and many other advantages.

The proposed beams with cross-profiled wall of trapezoidal (sinusoidal) shape with belts of channels on self-tapping screws are shown in **Figure 1**. The structure of such structures includes a single profiled wall (1), trapezoidal (sinusoidal) shape, which is fixed by screws (4) belt (2) (bent or rolled channels). With the help of welding (3) support ribs (5) (welded brands) are adjacent to the belts, and the wall is attached by means of a lamella screws (4). The proposed design of a steel beam with a cross-profiled box-section wall with uneven pitch of corrugations is shown in **Figure 2**. The profiled wall (2) of the beam has a trapezoidal shape, consists of long (4) and short (3) horizontal sections of the profiled sheet, as well as an inclined section of the corrugation (5). The corrugations of the presented beam have uneven steps that can be adjusted, which is not possible for wavy walls.

The wall of the beam is two cold-formed profiled sheets (2), fixed to the belts and ribs (6) around the perimeter, or in this case using lamellas (8), by welding (7). The beam ends have support ribs (6) and the I-beam shelves (1) are made of sheets. The main feature of the work is that the action of the bending moment is perceived by the shelves, and the transverse force is the wall of the beam.

Represented a modified form suggested above I-beam, steel beam from a transversely profiled wall of the box section with unevenly-spaced corrugations and intermittent welds (**Figure 3**). The structure of such a beam includes a trapezoidal profiled wall (2), which is welded on both sides intermittently (6) only on horizontal sections (3, 4) parallel to the longitudinal axis of the beam. The wall of the beam consists of two profiled sheets, which are attached to the edges (5) by continuous welding, and to the belts (1) by means of broken welds, which distinguishes it from the previous one, while providing savings in weld metal. The peculiarity of the beam is that the sections of corrugations are not transmitted longitudinal deformation, which provides a more uniform loading of the beam wall from the shelves.

Intermittent welds provide a uniform redistribution of forces in the shelves on the wall of the beam, as in the continuous seams forces quickly fall to a minimum. This occurs without action in the operation of most of the wall. In this case, intermittent welds (length of individual sections from 50 to 150 mm, and the distance between the sections, usually 1.5–2.5 times the length of the site) give some savings in production costs and provide sufficient stability of the wall, which does not perceive the efforts of the beam plane.
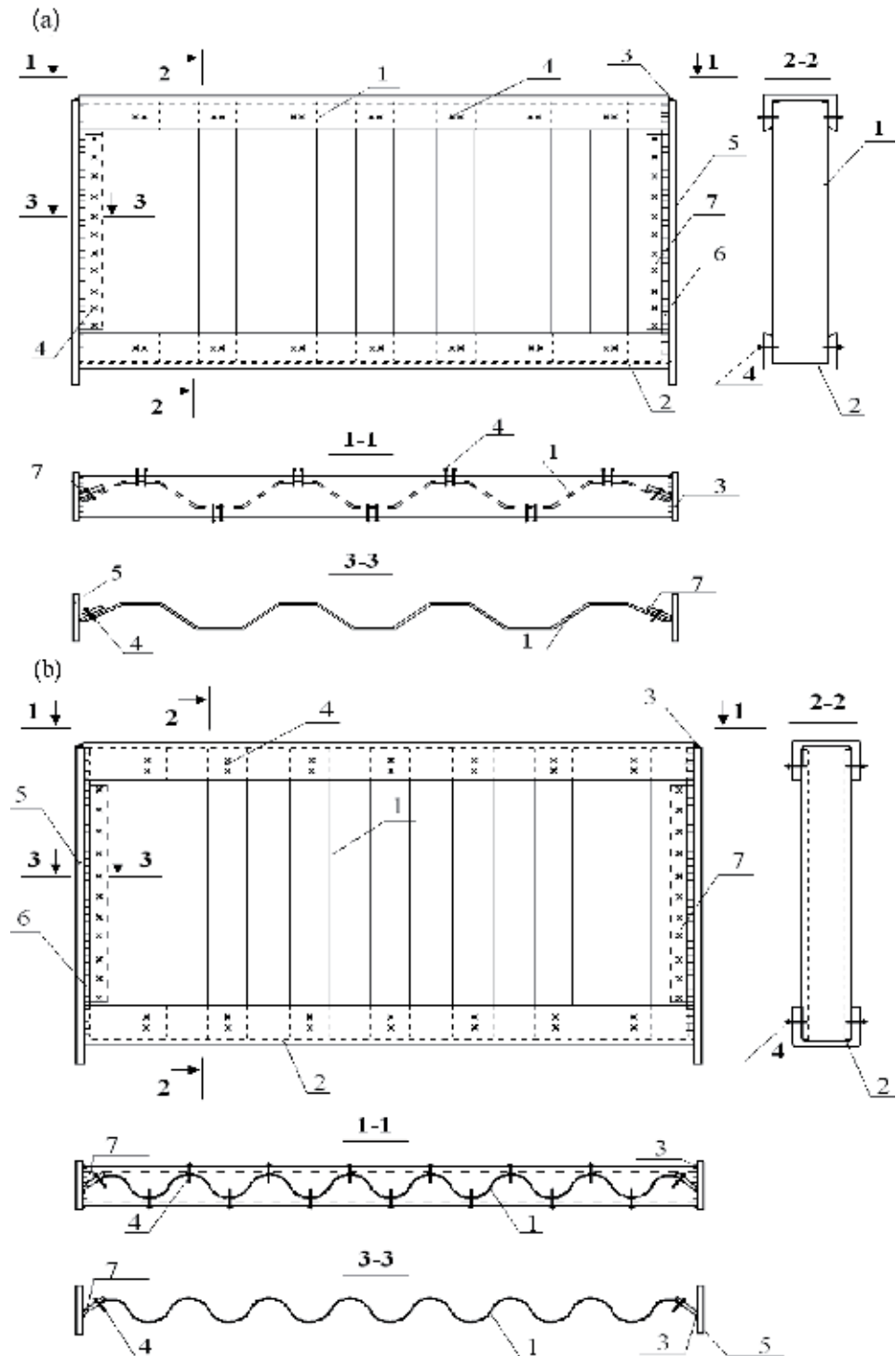
Figure 1.
Beam with cross-profiled wall with belts of channels on self-tapping screws: (a) trapezoidal wall [10];
(b) sinusoidal wall [11].

New designs of steel beams with cross-profiled box-section wall with welded-brand belts are proposed (**Figure 4**) and with the t-belt from rolling- (**Figure 5**). The profiled wall (2) of the beam has a trapezoidal shape, which is formed from the
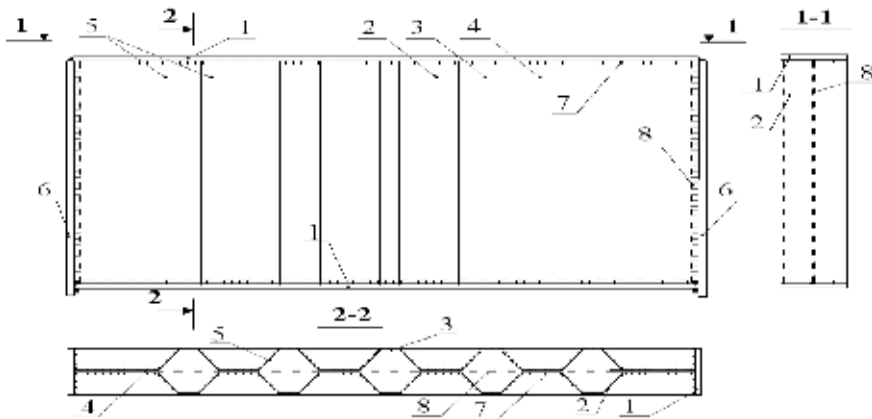
Figure 2.
Beam with a cross-profiled box-section wall with uneven pitch of corrugations [12].
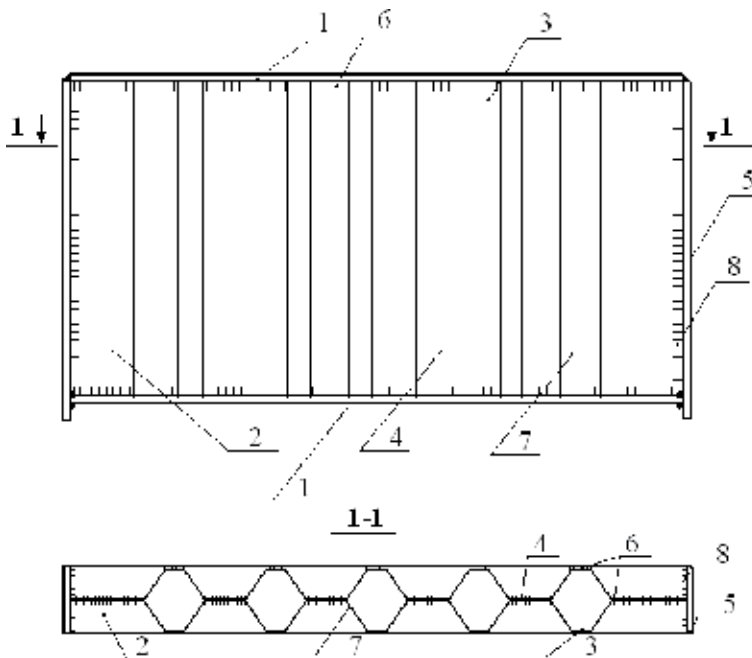
Figure 3.
Beam with cross-profiled box-section wall with intermittent welds [13].

inclined section of the corrugation (7), long (4) and short (3) horizontal sections of the profiled sheet. The wall of the beam consists of two profiled sheets (2), fixed by spot welding (6) belt (1), which consist of welded or rolled brands parallel to the axis of the beam. The wall in the support ribs (5) is attached by continuous welding (8). In this case, spot welds are used to attach the t-belts and the wall, which leads to the elimination of complex stress state. Attachment of the wall sections, which are close to the belt by spot welding, gives some flexibility to the wall along the beam and provides rigidity of the beam as a whole, as well as reversible perception of local stresses in the beam wall.

The wall does not reach the shelf and does not perceive normal forces, but only transverse force (shear stresses). The normal stresses are perceived only t-belts, as in an ideal I-beam. On the support parts of the beam, composite welded t-bar
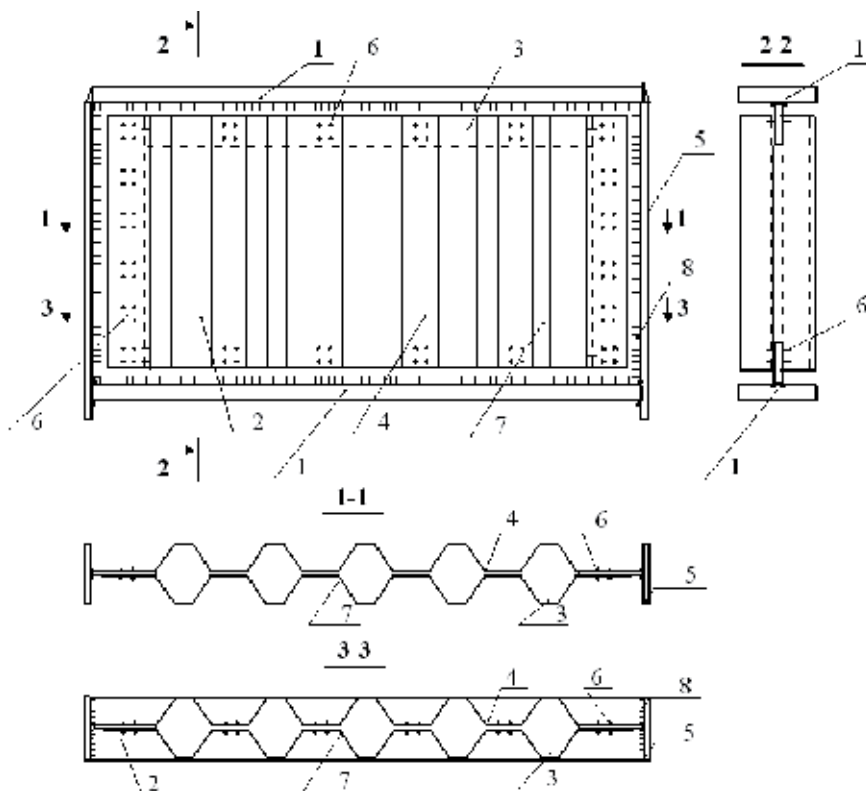
Figure 4.
Beam with cross-profiled box-section wall with welded-brand belts [14].

support ribs are used, which provide stability. The main advantage of such structures is that the belts from the brands perceive the action of the bending moment in the beam and work on tension and compression as an ideal I-beam, and the wall perceives the transverse force. In the areas of connection of the wall and shelves in the form of brands there is no zonal normal stresses in the upper and lower parts of the wall. In addition, the installation of t-bearing ribs provides stability and elimination of wall buckling in the area of the support unit. The wall of the rolling brand has a significant height, which ensures the strength of the belt and the upper part of the beam wall at normal stresses. The change in normal stresses is indicated by a hyperbolic dependence, which has maximum values at the top of the wall. Small local loads on the upper beam belt are more evenly distributed on the beam wall due to the t-belt.

A steel beam with profiled box-section wall with polystyrene foam is shown in **Figure 6**.

This construction (**Figure 6**) consists of profiled sheets (walls) (7) and support ribs (3). The space between them is filled with polystyrene foam (5). Belts (1) and guides (4) are made of square tubes, which are attached by solid welding. The wall is attached to the guides with self-tapping screws (2). The production of the beam begins with welding the initial billet. The wall of the beam is performed first by installing the profile on one side of the beam. In the future, the beam is in a horizontal position, where the polystyrene is applied in layers with subsequent installation of the upper profiled sheets.

The attachment of the profiled sheets is performed by self-tapping screws and installation through the mounting guides to prevent wall buckling. This course provides the opportunity to use a profiled wall of a smaller thickness (galvanized
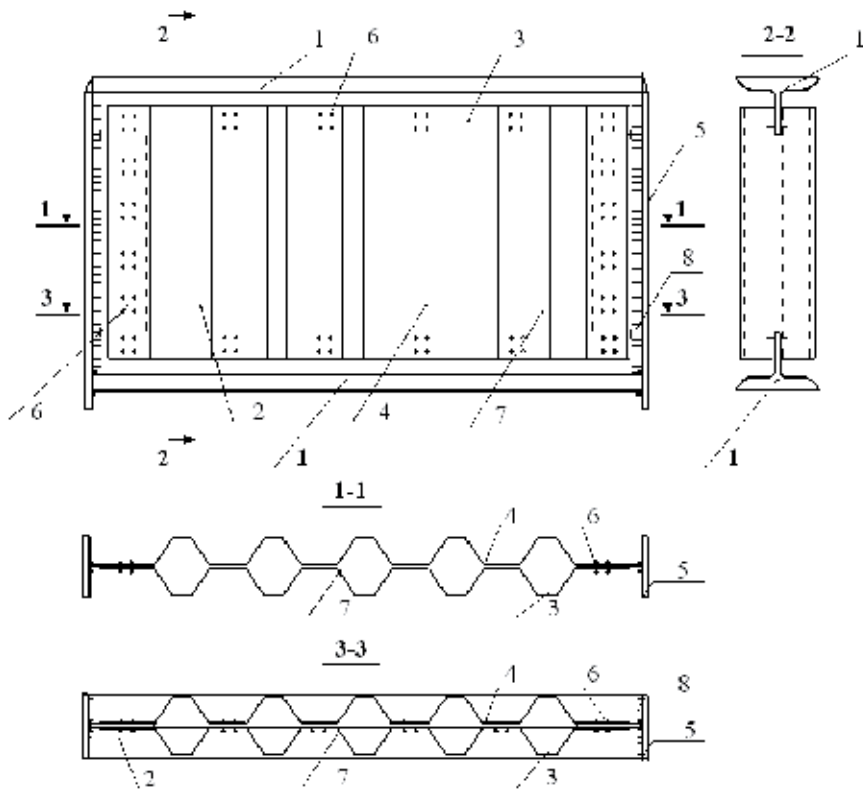
Figure 5.
Beam with cross-profiled box-section wall with the t-belt from rolling [15].

sheets), which is impossible or very difficult to weld. The sheets are joined together and fixed with screws. The use of polystyrene filling allows the use of this design with high thermal protection and sound insulation characteristics.

A new form is a beam with cross-profiled box-section wall and with belts of bent channels (fastening on screws) (**Figure 7**). This design allows the use of thin belts profiled sheets from 1 to 2 mm (welding is difficult). The structure of this design includes a profiled wall (1), which has a trapezoidal shape and consists of two profiled sheets, which are fixed to the belts (2) in the form of bent or rolled channels with screws (4). Profiles can be fastened together with self-tapping screws. The support ribs (5) are welded marks that are attached to the belts by welding (3) and to the wall by screws (4). The wall of this design can be single and have a wavy outline.

Below are steel beams with transversely profiled box-section wall, unfastened by diagonal lattice (**Figure 8**) and cross lattice (**Figure 9**), lattice in the form of arch elements (**Figure 10**).

In these structures, the profiled wall (7) of the beams is trapezoidal and consists of two profiled sheets, which are fixed in the guides (4) in the form of square pipes with self-tapping screws (2). The guides are attached to the belts (1), which consist of square tubes, by means of continuous welding (6). The support ribs (8) are made of sheets taking into account the work of crushing and cutting. The grate (3) is attached to the profiled sheets by self-tapping screws (2). Holes can be made to attach beams to a possible column (5).

Initial blanks for this type of structures, as well as for the following are performed at the beginning of the manufacture of beams. The location of the diagonal of the lattice must match the local load on the top chord of the beam. If you are
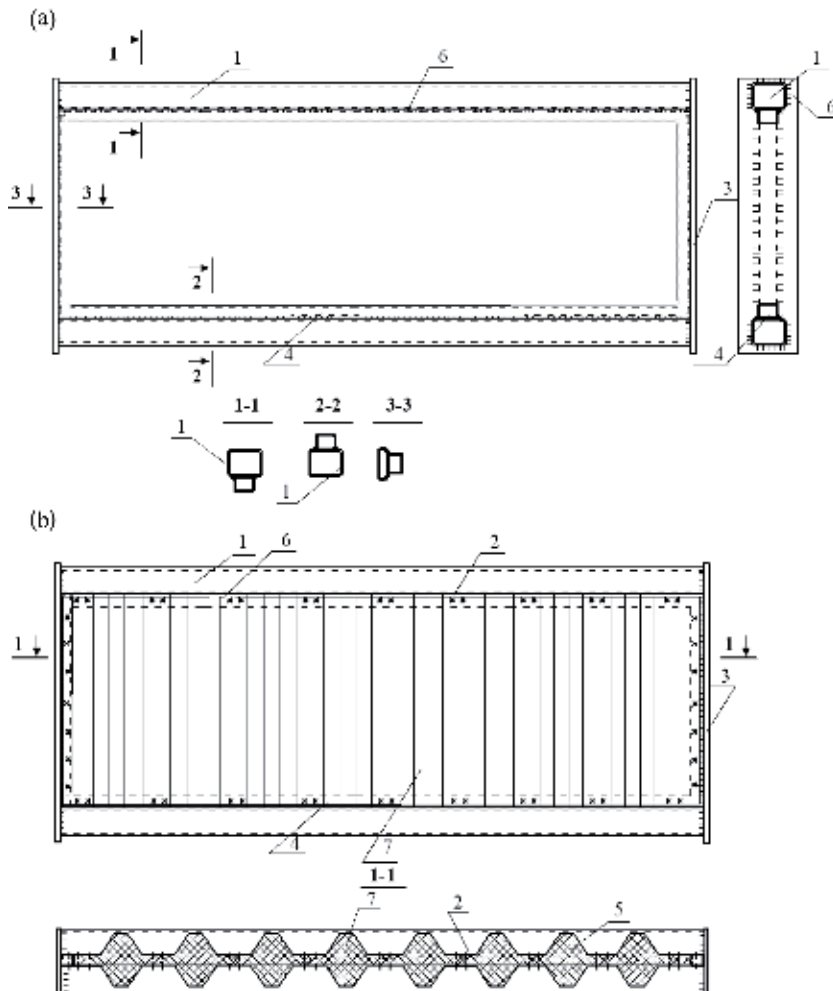
Figure 6.
Beam with profiled box-section wall with polystyrene foam [16]: (a) initial blank; (b) ready compartment.

installing a diagonal lattice, you can avoid using stiffeners under local load. Another feature of this type of construction is that the elements of the lattice in combination with the profiled wall provide greater stability than the individual struts of the lattice and the wall. Considering the cross lattice (**Figure 9**), it is possible to note its superiority in rigidity of a wall and ensuring stability of a wall on all height of a beam. Cross grid distributes the action of bending moment along the length of the span and unfastened profiled sheet to ensure sustainability.

Lattice of arched elements (**Figure 10**) and their shape reproduce the plot points and take some of the action. In areas close to the supports, the arches intersect and perceive additional forces in the zone of inclined cross-sections of the beam. In the span, the cross-section of the I-beam is close to the "ideal I-beam", which is the optimal cross-section for the perception of bending moment. In order to obtain less metal-nitrate structures, it is rational to use an arched lattice, which can be both double and single.

The calculation of combined beams from sheet or tubular belts is performed on a PC using a full-dimensional continuous description in the calculation complexes or on models with a breakdown into separate systems taking into account the physical and geometric nonlinearity. The use of the presented structures is not limited to truss structures, but extends to floor beams, crossbars of single—and multistory
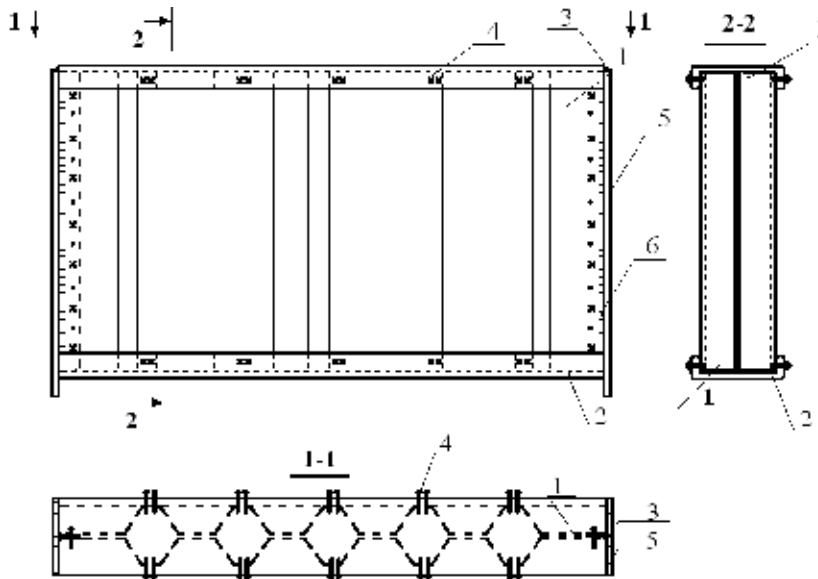
Figure 7.
Beam with cross-profiled box-section wall with belts of bent channels [17].

buildings, arches, galleries, technological platforms, span structures of bridges and the like. There is a possibility of application of the presented designs in beam systems with static loading.

The use of this type of beams provides a number of advantages in comparison with conventional ones, namely esthetic appearance, strength and reliability, durability of structures, low operating costs, but their main advantage is ease and stability.

One of the ways to improve light load-bearing structures, in our opinion, is the use of structural elements of closed profiles, which can have different sections, in particular square, rectangular and oval. Considering the technological features of manufacturing, we note that the pipe section is primarily round, and eventually deformed by various methods (hot and cold), acquiring different shapes.

New design solutions of combined resource-efficient metal structures of trusses and arches are proposed (**Figures 11–14**). In particular, **Figure 11** shows the combined metal structure of the truss with belts in the form of rectangular pipes, the lower belt in the form of a curved down arch that works on tension. This lower belt design is more economical than compressed belt. The upper belt in the form of two compressed rectangular pipes and unfastened by Breweries works as a whole system and can perform additional functions of fencing. This design feature provides an opportunity to reduce the material consumption and generally improve the efficiency of the whole structure.

So, the composition of the proposed combined metal truss structure include (**Figure 11**): (1, 3) to the upper belt in the form of two rectangular pipes (section pipe size from 120 to 200 mm); (2) the lower zone of the rectangular pipes in the form of an arched element (section pipe size from 120 to 200 mm); (4, 5) bearing edges of the continuous sheet (thickness from 6 to 10 mm); (6) reference sheet (thickness from 10 to 20 mm); (7) retaining wall (thickness from 8 to 12 mm); (8) lattice (section pipe size from 80 to 100 mm); (9) element of the lattice of the upper belt and at the same time enclosing structure (half arches, section pipe size from 40 to 60 mm).

The combined metal structure of the truss is proposed due to the paired upper arched belt and the lower belt, which works on tension, provides multivariance of application and significantly reduces material costs. The load from the coating in the
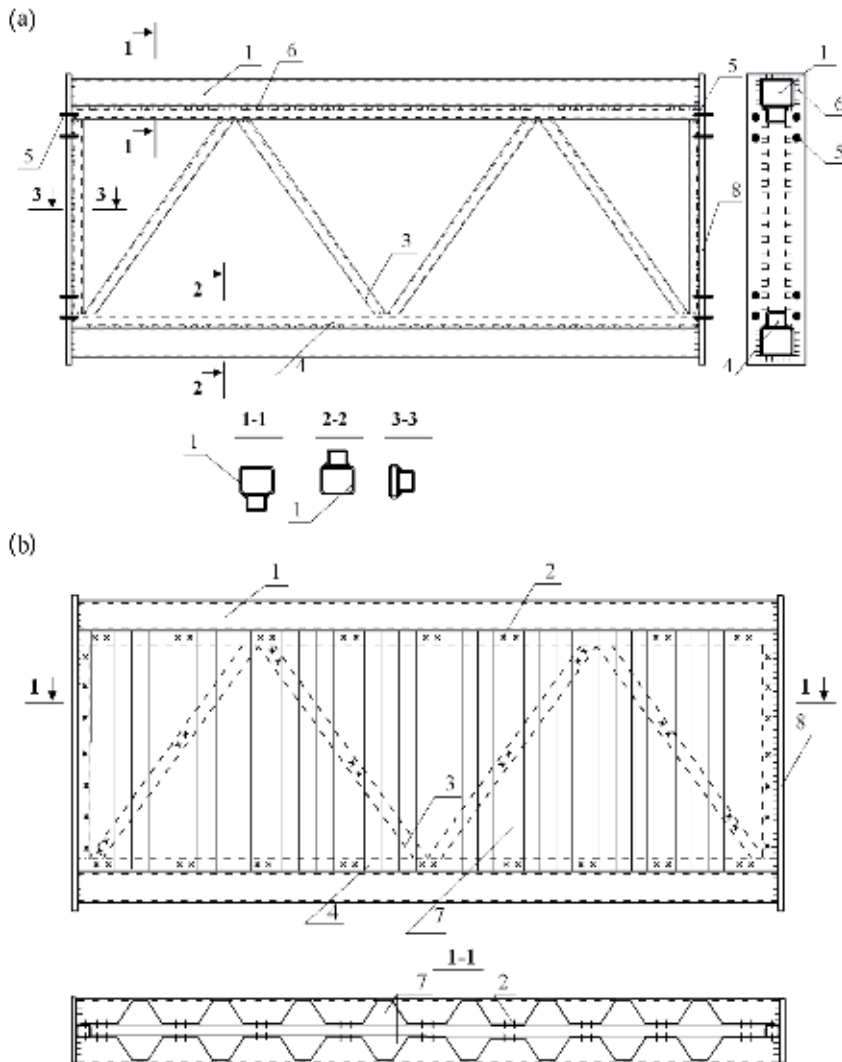
Figure 8.
Beam with transversely profiled box-section wall, unfastened by diagonal lattice [18]: (a) initial blank; (b) ready compartment.

form of transverse beams (beam cage) is transmitted to the lower part of the upper belt, which is unfastened from the plane of the farm and works with the flooring as a spatial system. The upper part of the upper belt, if necessary, can be unfastened from the plane by triangular dual-purpose supports for communications (pipelines, etc.). The rational use of the proposed structures for spans of 24–36 m is recommended.

The development of combined structures in the form of trusses can occur through the use of spatial triangular rod elements for the upper belt, which will increase the stability of the truss plane and reduce the cost of the structure by weight compared to solid sections. Note that the complexity of such structures is growing, so you need to evaluate these projects at the given cost.

Considering the traditional forms of arched structures, we note that their solid elements work as compressed curved and additionally perceive transverse forces. For this type of compressed curved arches optimal design solution is considered to be I-section with a solid wall. In our opinion, the use of corrugated walls in the arches of the composite I-section is quite controversial, since the corrugated wall
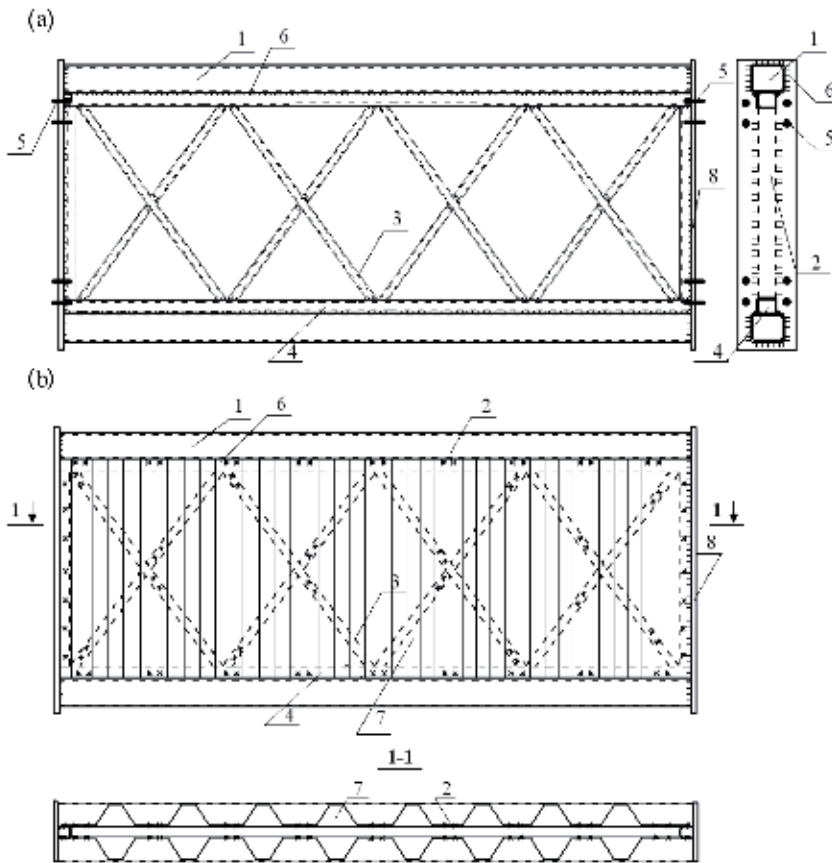
Figure 9.
Beam with transversely profiled box-section wall, unfastened by cross lattice [19]: (a) initial blank; (b) ready compartment.

perceives the transverse force, and for the perception of the longitudinal force there is a constructive need for the use of additional elements, for example, cross lattice. Such a constructive move increases the cost of arches, increases the metal consumption and the complexity of manufacturing such types of structures. Consequently, the use of continuous wall corrugation, both in arches and columns will not provide the necessary technical and economic effect and as a result, is not very rational.

If we consider the design of the truss, the lower belt which works as a stretched curved element, and the upper belt works on compression (for the case without a wall—Central compression, and in General, off-center compression), it is possible to use in these structures corrugated wall, which would perceive the transverse load. For this type of construction, the stiffness of the corrugated wall in the longitudinal direction will be minimal, however, these efforts will only perceive the belt, and a significant proportion of the transverse forces will be perceived corrugated wall compatible with the belts. Corrugated wall also loosens the belt in the plane of the structure.

The combined structure with the upper and lower belts in the form of square pipes is presented. The latter works as an arched element (**Figure 12**): (1) the upper belt of rectangular pipes (section pipe size from 120 to 200 mm); (2) the lower belt of rectangular pipes in the form of an arched element; (3) ribs (thickness from 6 to 8 mm); (4) the wall of a single sheet (thickness from 6 to 8 mm); (5) corrugated wall wavy shape (possible thickness from 2 to 3 mm); (6) support sheet (thickness
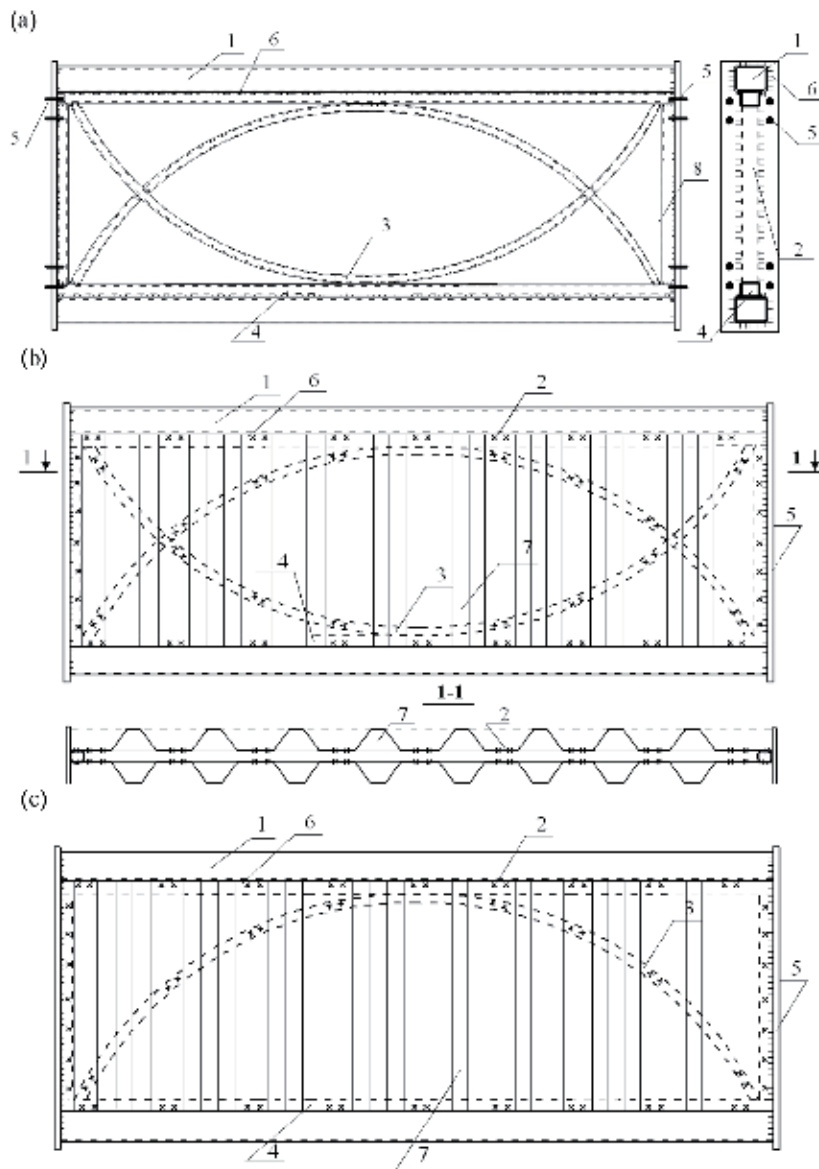
Figure 10.
Beam with transversely profiled box-section wall, unfastened by lattice in the form of arch elements: (a) initial blank with double arched elements; (b) ready compartment with double arched elements [20]; (c) ready compartment with one arched element [21].

from 8 to 10 mm); (7) support edge (thickness from 10 to 12 mm); (8) angular welding (thickness from 4 to 6 mm).

There is a possibility of performing the supporting sections of such structural solutions with the use of steel sheets, which will provide greater bearing capacity under the action of transverse forces. In turn, the corrugation must be performed in the span areas. It should be noted that under the condition of perception of local concentrated loads by the design, there is a need to install stiffeners both in traditional composite beams and in the above structures, since they perform the functions of ensuring the stability of the wall. The combined design is shown
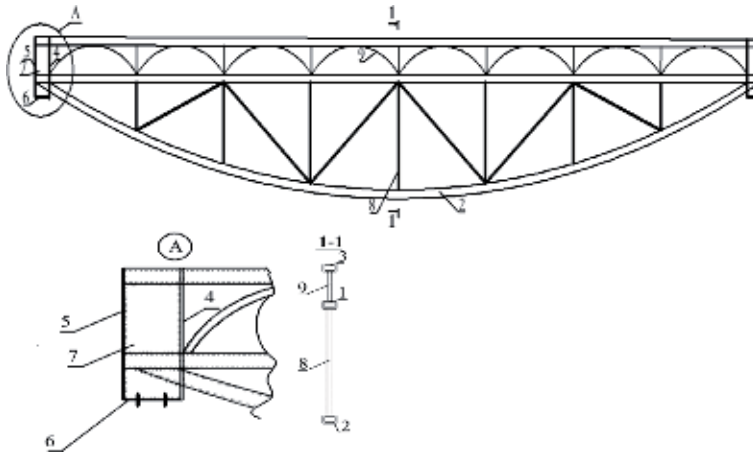
Figure 11.
Truss combined metal structure [22].
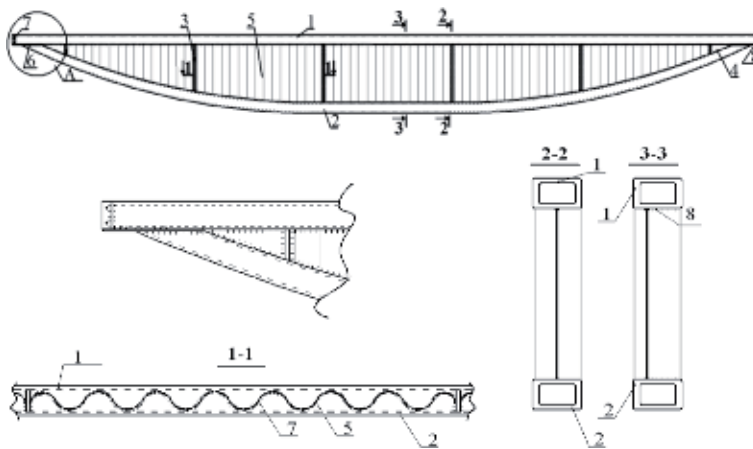
Figure 12.
Resource-saving combined metal structure (length from 8 to 30 m) [23].
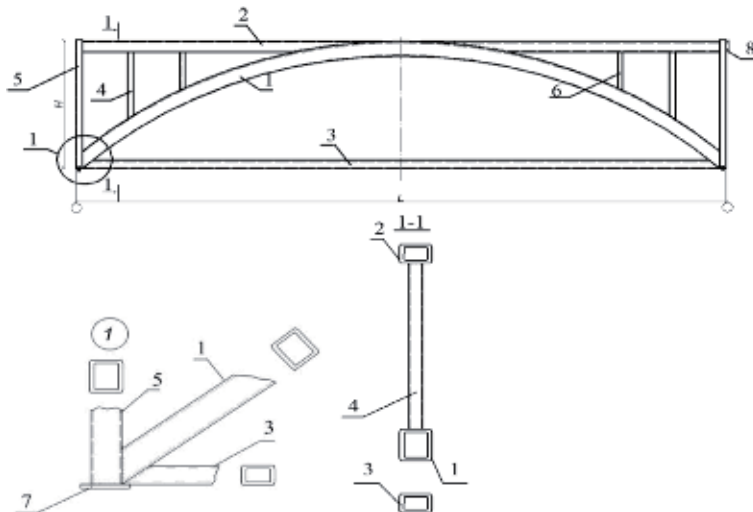
Figure 13.
Combined structure of a metal arch with racks [24].
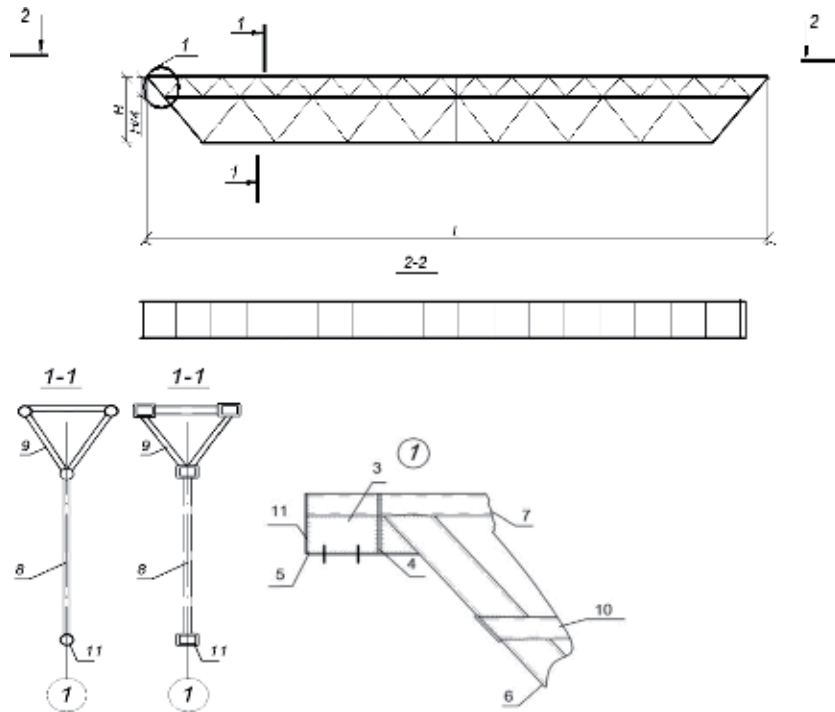
Figure 14.
Combined structure of metal trusses with upper spatial zone [25].

(**Figure 12**) are an alternative to conventional beams and trusses, which provides a reduction in the construction height (can simultaneously perform the function of the enclosing structure), transport and installation costs.

The combined structure of metal trusses with upper spatial zone is presented (**Figure 13**). This design solution can be used as a single-arched system, reinforced with a system of racks with optimal performance, in particular, with an optimal ratio of height and span of the supporting structure. The design feature of this type of structures is the use of elements in the form of rectangular pipes and cantilever arch support system.

The main elements of the presented design are: (1) the main element of the arch- a rectangular pipe (section pipe size from 120 to 200 mm); (2) the upper belt of a rectangular pipe (section pipe size from 120 to 200 mm); (3) the lower belt of a rectangular pipe (section pipe size from 80 to 100 mm); (4, 5, 6) racks (section pipe size from 80 to 100 mm); (7) the base plate of the sheet (thickness from 6 to 10 mm); (8) the support edge of the sheet (thickness from 10 to 20 mm). Considering the technological advantages of such a structural form, we note that it is possible to use reduced corrosion-resistant sections of the optimal shape (rectangular pipes) to obtain resource-economic structures with a minimum weight. Outlining the stages of manufacturing this welded arch with racks, a necessary step is to secure the installation with bolts of high strength. The authors recommended the rational use of combined structures of metal arches with racks for spans 12–36 m.

With the aim of obtaining optimal performance constructive solutions have been proposed combined structure metal truss with upper spatial zone (**Figure 14**): (1) runs; (2) ties; (3) longitudinal edge of a solid sheet (thickness from 8 to 12 mm); (7, 10) branches of the upper belt in the form of three round (rectangular) pipes (section pipe size from 80 to 100 mm); (4, 11) transverse support ribs of a solid sheet (thickness from 6 to 10 mm); (5) support sheet (thickness from

10 to 20 mm); (6) lattice element; (9) struts of the through belt of the truss (section pipe size from 80 to 100 mm); (8) element of the truss lattice (section pipe size from 100 to 160 mm).

This design form can be used in light load-bearing coating structures with profiled steel flooring. For this type of structures span can vary from small (24 m) to significantly large (more than 36 m). The recommended slope designs may be a standard 1.5%, and a large (as per design assignment). It is possible to use the arched shape of the truss for the corresponding spans. For this type of structures, the height of the truss is determined by the stiffness and depends on the span. Considering the design features of the combined structure of the truss with a spatial upper belt, it should be noted that the installation parts of the farms are performed according to the standards for the transportation of goods. It is recommended to connect the mounting elements of the trusses with flanges on bolts, as well as by welding, using pipes of larger diameter, which significantly reduces the metal content of the connections. Runs between truss are made of rolling profiles and fixed according to the continuous scheme, due to the wide upper belt of the farm. It should be noted that the use of this type of structures is due to economic calculations according to the above costs compared to standard coating structures.

3. Conclusion

The increase in the complexity of the manufacture of spatial structures is overlapped by a decrease in the material intensity of structures, which makes it possible to obtain more economical designs. The proposed new constructive solutions of steel space trusses, arches and frames which have the characteristics of high bearing capacity and the architectural expression, to minimize the indicators of material and labor costs. Structures of this type have increased characteristics of the overall stability of the individual elements and the system as a whole both in the plane and from the plane. As a result of the study, a number of design solutions of light combined structures are presented, which have a wide range of applications in construction. The advantages of the proposed solutions are ease, industry and great rigidity. Numerical calculations of frame structures allowed to bring the efficiency of these design solutions and track a significant reduction in effort in the racks.

Author details

Chichulina Kseniia* and Chichulin Viktor
Poltava National Technical Yuri Kondratyuk University, Poltava, Ukraine

*Address all correspondence to: chichulinak@ukr.net

References

[1] Zanzoni A, Montecchi-Palazzi L, Quondam MX. Shear buckling and stress distribution in trapezoidal web corrugated steel beams. Thin-Walled Structures, Elsevier. 2017;**113**:13-26. DOI: 10.1016/j.tws.2017.01.002

[2] Cheng X, Chen H, Gong Y, Yang YB. Stocky thin- or thick-walled beams: Theory and analysis. Engineering Structures, Elsevier. 2018;**159**:55-65. DOI: 10.1016/j.engstruct.2017.12.027

[3] Magnucka-Blandzi E, Magnucki K, Wittenbeck L. Mathematical modeling of shearing effect for sandwich beams with sinusoidal corrugated cores. Applied Mathematical Modelling, Elsevier. 2015;**39**(9):2796-2808. DOI: 10.1016/j.apm.2014.10.069

[4] James L, Moody ED, Dexter P. Lighting trusses. In: Concert Lighting. 3rd ed. Oxford, UK: Elsevier, Focal Press; 2010. pp. 131-142. DOI: 10.1016/B978-0-240-80689-1.00013-1

[5] Farkas J, Jarmai K. Tubular structures. In: Design and Optimization of Metal Structures. 1st ed. Cambridge: Elsevier, Woodhead Publishing; 2008. pp. 225-251. DOI: 10.1533/9781782420477.225

[6] Holloway J. Metal frame construction. In: Illustrated Theatre Production Guide. 2nd ed. Oxford, UK: Elsevier, Focal Press; 2008. pp. 339-364. DOI: 10.1016/B978-0-240-81204-5.00021-1

[7] Lukin AO. Patent RU166510U1. I-Beam with Corrugated Web. Russia: Lukin Aleksey Olegovich; 2016. 4 p

[8] Lukin AO. Patent RU162845U1. Metal Beams with Corrugated Wall. Russia: Lukin Aleksey Olegovich; 2016. 4 p

[9] Rybkin IS. RU2492301C1 Beam with Corrugated Asymmetric Profile Wall. Russia: Rybkin Ivan Sergeevich; 2013. 4 p

[10] Pichugin SF, Chichulin VP, Chichulina KV. Patent 92503 Ukraine: Steel Single Beam with Cross-Profiled Wall of Trapezoidal Shape, with Belts of Channels. Ukraine: Poltava National Technical Yuri Kondratyuk University; 2014. 4 p

[11] Pichugin SF, Chichulin VP, Chichulina KV. Patent 92502 Ukraine: Steel Single Beam with Cross-Profiled Wall of Sinusoidal Shape, with Belts of Channels. Ukraine: Poltava National Technical Yuri Kondratyuk University; 2014. 4 p

[12] Pichugin SF, Chichulin VP, Chichulina KV. Patent 45328 Ukraine: Steel Beam with Cross-Profiled Box-Section Wall with Uneven Pitch of Corrugations. Ukraine: Poltava National Technical Yuri Kondratyuk University; 2009. 4 p

[13] Pichugin SF, Chichulin VP, Chichulina KV. Patent 51629 Ukraine: Steel Beam with Cross-Profiled Box-Section Wall with Intermittent Welds. Ukraine: Poltava National Technical Yuri Kondratyuk University; 2010. 4 p

[14] Pichugin SF, Chichulin VP, Chichulina KV. Patent 66810 Ukraine: Steel Beam with Cross-Profiled Box-Section Wall with Welded-Brand Belts. Ukraine: Poltava National Technical Yuri Kondratyuk University; 2012. 4 p

[15] Pichugin SF, Chichulin VP, Chichulina KV. Patent 64444 Ukraine: Steel Beam with Cross-Profiled Box-Section Wall with the t-belt from Rolling. Ukraine: Poltava National Technical Yuri Kondratyuk University; 2011. 4 p

[16] Pichugin SF, Chichulin VP, Chichulina K V. Patent 64443 Ukraine: Steel Beam with Cross-Profiled Box-Section Wall with Polystyrene Foam. Ukraine: Poltava National Technical Yuri Kondratyuk University; 2011. 4 p

[17] Pichugin SF, Chichulin VP, Chichulina K V. Patent 80648 Ukraine: Steel Beam with Cross-Profiled Box-Section Wall with Belts of Bent Channels. Ukraine: Poltava National Technical Yuri Kondratyuk University; 2013. 4 p

[18] Pichugin SF, Chichulin VP, Chichulina K V. Patent 64445 Ukraine: Steel Beam with Cross-Profiled Box-Section Wall, Unfastened by Diagonal Lattice. Ukraine: Poltava National Technical Yuri Kondratyuk University; 2011. 4 p

[19] Pichugin SF, Chichulin VP, Chichulina K V. Patent 79707 Ukraine: Steel Beam with Cross-Profiled Box-Section Wall, Unfastened by Cross Lattice. Ukraine: Poltava National Technical Yuri Kondratyuk University; 2013. 4 p

[20] Pichugin SF, Chichulin VP, Chichulina KV. Patent 80802 Ukraine: Steel Beam with Cross-Profiled Box-Section Wall, Unfastened by Lattice of Arched Elements. Ukraine: Poltava National Technical Yuri Kondratyuk University; 2013. 4 p

[21] Pichugin SF, Chichulin VP, Chichulina KV. Patent 80166 Ukraine: Steel Beam with Cross-Profiled Box-Section Wall, Unfastened by Lattice of One Arched Element. Ukraine: Poltava National Technical Yuri Kondratyuk University; 2013. 4 p

[22] Pichugin SF, Chichulin VP, Chichulina KV. Patent 98331 Ukraine: Truss Combined Metal Structure. Ukraine: Poltava National Technical Yuri Kondratyuk University; 2015. 4 p

[23] Pichugin SF, Chichulin VP, Chichulina KV. Patent 98332 Ukraine: Resource-Saving Combined Metal Structure. Ukraine: Poltava National Technical Yuri Kondratyuk University; 2015. 4 p

[24] Pichugin SF, Chichulin VP, Chichulina KV. Patent 111247 Ukraine: Combined Structure of a Metal Arch with Racks. Ukraine: Poltava National Technical Yuri Kondratyuk University; 2016. 4 p

[25] Pichugin SF, Chichulin VP, Chichulina KV. Patent 111248 Ukraine: Combined Structure of Metal Trusses with Upper Spatial Zone. Ukraine: Poltava National Technical Yuri Kondratyuk University; 2016. 4 p

Research of Lightweight Structures for Sandwich Core Model

Jeongho Choi

Abstract

The objective of this chapter is to focus on finding mechanical properties for two models defined as core-filled model (Type 1) and core-spaced model (Type 2) created by direct metal laser sintering (DMLS). Applied material is aluminum alloy AlSi10Mg powder and each model is created as a vertical additive manufacturing with DMLS. After quasi-static compression, Type 1 showed 19% higher elastic modulus, 12% higher compressive yield strength, and 51.6% higher elongation than Type 2. By uniaxial compressive test, there found two issues that can be the reasons to make weaker models by 3D printing were found: melted metals by DMLS are not connected with each other preciously and a space in additive layer when additive manufacturing makes a shape of specimen. In addition, anisotropy is the significant factor to decide stiffness or strength. In nearby future, various kinds of unit models such as core-filled or core-spaced model hope to be made a sandwich core structure and to be investigating more deeply about bending or shear properties continuously. In the near future, it is hoped that we see more upgraded 3D printing techniques for making aerospace materials.

Keywords: cellular solids, open cell unit model, closed cell unit model, honeycomb, stiffness, strength

1. Introduction

Generally, solid is composed of stereoscopic structure. The stereoscopic structure is a model based on two-dimension, three-dimension, and four-dimension in a space. The two-dimension is two axis like horizontal direction and vertical direction in a plane. The three-dimensional structure has three axes such as x, y, and z coordination, for instance, a vector. The four-dimensional structure has four axes such as optical illusion, for example, a cubic box. If the box is torn at every corner, then it can make a two-dimensional plane. If it is folded up, it can make a cubic box. This is called as tesseract, hypercube, or 8-cell regular octachoron. These are based on a geometrical concept in mathematics. It is the four-dimensional object called as hypercube or tesseract shown in **Figure 1**.

Applications of the hypercube were shape or size optimization for non-probabilistic description of uncertainty as computer aided optimum design of structure [1], optimal communication algorithms for hypercubes [2], parallel computing on a hypercube [3], structure connectivity [4], and so on.

It is interested in to create a unit cell model like honeycomb or open-cell in a sandwich core structure.
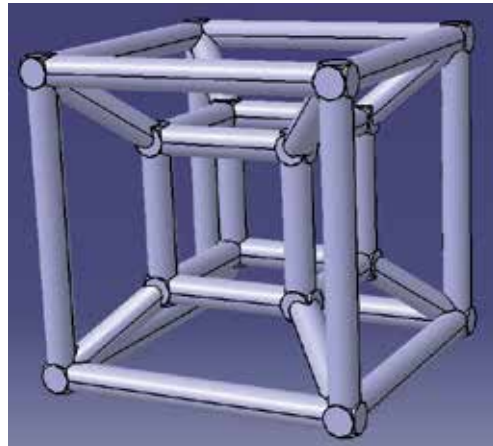
Figure 1.
Schematic of a hypercube.

Hypercube originates from a point, which is a hypercube of dimension zero [5, 6]. If the point moves to another point, it makes a line, which is a unit hypercube of dimension one. If the line moves out in a perpendicular direction, it makes a square, which is a unit hypercube of dimension two. If the square moves to a perpendicular direction, it makes a cube, which is a unit hypercube of dimension three. And if the cube moves to the fourth dimension, it is called a four-dimensional hypercube as a unit tesseract.

In the engineering material field, one of the simplest lightweight truss model is truss cubic, which is defined by Gibson and Ashby [7]; it is a model of hexagonal truss to define an ideal solution for honeycomb, open cell, or closed cell model. This is based on the three-dimensional stereoscopic structure. It can create a model which is hypercube truss model composed of a hexagonal truss inside and a hexagonal truss inside. Thus, this paper is focused on studying the hypercube concept to make a unit model to apply for a sandwich core structure.

If tesseract is composed of two regular hexahedrons, i.e., one is for outer structure and the other is for inner structure, with or without diagonal truss, then two types of model can be defined such as the core-filled or the core-spaced shape. That is, it depends with or without a truss in a diagonal direction. Therefore, this paper is focused on studying two models defined as Type 1 and Type 2.

According to the reported papers on the mechanical properties of structures that are 3D printed with powders recently, there are advantages and disadvantages.

The merits are to make a shape easily, to save time, to create a complex shape without any limited shape, and to make a high-quality part for the application in the aerospace or biomedical industry. Demerits are a high cost to create a product, a limited space to make a product, a limited materials such as metal powders, a required high quality equipment to produce high quality product, a need to hire a professional engineers to take control the equipment, etc.

Three-dimensional printing skill is not a magic to create anything; it requires techniques to be used with materials. The most important is what the application is. Thus, depending on the skills of the materials, the quality of a product is decided. Recently, 3D printing skill is announced as a revolution in manufacturing technique and it has been developed more and more. From the beginning of the skill, it is defined various techniques like fused deposition modeling (FDM) [8, 10], selective laser sintering (SLS) [9], direct light processing (DLP) [7, 8, 12], stereolithography (SLA) [11, 13], laminated object manufacturing (LOM) [11, 14], stereolithography (SL) [14], mask projection stereolithography (MPSL) [14], three-dimensional printing (3DP) [14], droplet

deposition manufacturing (DDM) [14], and fused filament fabrication (FFF) [15, 16]. Based on these techniques, new skills are currently being developed and announced.

Nowadays, a common skill of the 3D printing is direct metal laser sintering (DMLS) [17, 18]. It uses laser with metal powders, which is Laser beam melt metal powders to be droplet as liquid status. The drip metal is added layer by layer to make a shape.

To validate mechanical properties, tension and compression with a specimen made by ASTM standard are required. Many researchers found a specimen made by 3D printing have anisotropy and they shows mechanical properties are not shown in constant. They carried out experiments with different materials and with 3D printing. However, they show different properties depending on the 3D skill, equipment, applying material, additive manufacturing speeding, and so on. There are many kinds of effective variables [19–24].

This chapter concentrated on the investigation of stiffness or strength for unit cell models made by DMLS 3D printing. And it is hope to find mechanical properties of various unit models to make a sandwich core structure.

2. Hypercube models

For designed models, it is defined as an ideal mathematical solution. Based on the previous researchers, lattice or truss model defined as open cell model may have a correlation between relative elastic modulus as a function of relative density or between relative compressive yield strength as a function of relative density. Thus, **Figure 2** shows Type 1 and Type 2 shape. The next section shows details on stiffness or strength for both the models. Type 1 is core-filled model and Type 2 is a core-spaced model. Each model is created by the DMLS technique. And then both models are tested by compression. Before experimental testing for Type 1 and Type 2, they are checked for material properties of a specimen based on ASTM E8/E8M [25]. The specimen is made by DMLS and then tested by tension and compression to check the material properties.
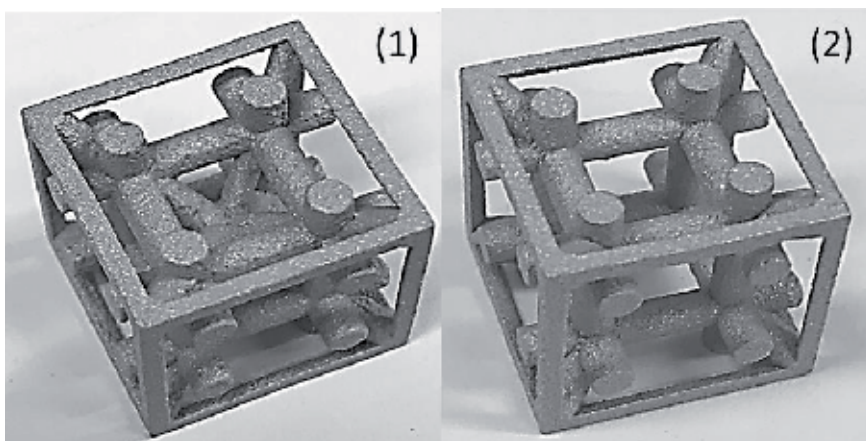
Figure 2.
Samples made by the 3D printing DMLS skill: (1) is Type 1 and (2) is Type 2.

3. 3D printing equipment (DMLS)

It used 3D printing machine which is defined as EOS M290. This is the DMLS (Direct Metal Laser Sintering) skill to make a specimen. It has a property summarized in **Table 1**. It shows more detailed information for the equipment. Among

Technical data EOS M290	
Building volume (mm)	**250 × 250 × 325**
Laser type (W)	Yb fiber laser; 40
Precision optics	F-theta lens; high-speed scanner
Scanning speed (m/s)	Up to 7.0
Focus diameter (μm)	100
Power supply (A/V)	32/400
Power consumption (kW)	Max. 8.5/average 2.4/with platform heating up to 3.2
Inert gas supply (hPa)	7000
Dimensions	W × D × H
System (mm)	2500 × 1300 × 2190
Recommended installation space (mm)	Min 4800 × 3600 × 2900
Weight(kg)	In approx. 1250
Software	EOSTATE Everywhere, EOSPRINT incl. EOS PArameterEditor
Materials	EOS Aluminum AlSi10Mg, EOS CobaltChrome MP1, EOS Maraging Steel MS1, EOS NickelAlloy HX, EOS NickelAlloy IN625, EOS NickelAlloy IN718, EOS StainlessSteel CX, EOS StainlessSteel PH1, EOS StainlessSteel 17-4PH, EOS StainlessSteel 316 L, EOS Titanium Ti64, EOS Titanium Ti64ELI, EOS Titanium TiCP Grade2
Optional accessories	EOSTATE Monitoring Suite (EOSTATE Laser, EOSTATE PowerBed, EOSTATE MeltPool, EOSTATE Exposure OT). Comfort Power Module, IPCM-M extra, IPCM-M pro, wet separator blasting cabinet

Table 1.
Technical data of DMLS equipment.

these, one of the most important factors is building volume and power supply for the laser. Maximum size of volume to make a model is 250 mm × 250 mm × 325 mm. To make a good quality model, volume size must be 200 mm × 200 mm × 300 mm at least. And laser type is Yb fiber laser with 40 Watt, scanning speed is up to 7.0 m/s, and power supply is 32 ampere with 400 Volt. In addition, more information for the equipment such as dimensions, weight, software, applying materials, etc., is described in the table, especially, materials that have been developing continuously. Now they can obtain materials like aluminum alloy, cobalt chrome, nickel alloy, stainless steel, and titanium alloy. These are based on powder type.

Technical data for aluminum alloy is shown in **Table 1** and **3D** printing machine, EOS M290, based on DMLS skill.

4. Material properties (powder)

Applied material properties in this paper is aluminum alloy, which is AlSi10Mg. Based on ASTM E8M, specimens for compression and tension are made by the DMLS (direct metal laser sintering) 3D printing technique. **Figure 3** shows specimens after tensile test.
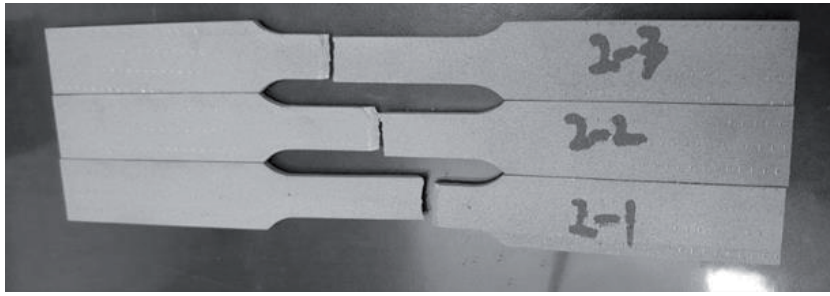
Figure 3.
Specimens made by aluminum alloy (AlSi10Mg) after tension test.

		As built	Heat treated
Typical achievable part accuracy (µm)		±100	
Smallest wall thickness (mm)		Approx. 0.3–0.4	
Surface roughness, as built, cleaned (µm)		Ra 6–10, Rz 30–40	
-after micro shot-peening (µm)		Ra 7–10, Rz 50–60	
Volume rate (mm^3/s)		7.4	
Physical and chemical properties of the parts			
Material composition (wt%)		Al (balance), Si (9.0–11.0), Fe($\leq$0.55), Cu($\leq$0.05), Mn($\leq$0.45), Mg(0.2–0.45), Ni($\leq$0.05), Zn($\leq$0.10), Pb($\leq$0.05), Sn($\leq$0.05), Ti($\leq$0.15)	
Relative density (%)		Approx. 99.85	
Density (g/cm^3)		2.67	
Mechanical properties of the parts			
		As built	Heat treated
Tensile strength (MPa)	In horizontal direction (XY)	460 ± 20	345 ± 10
	In vertical direction (Z)	460 ± 20	350 ± 10
Yield strength, Rp0.2%(MPa)	In horizontal direction (XY)	270 ± 20	230 ± 20
	In vertical direction (Z)	240 ± 20	230 ± 20
Modulus of elasticity (GPa)	In horizontal direction (XY)	75 ± 10	70 ± 10
	In vertical direction (Z)	70 ± 10	60 ± 10
Elongation at break (%)	In horizontal direction (XY)	9 ± 2	12 ± 2
	In vertical direction (Z)	6 ± 2	11 ± 2
Hardness (HBW)		Approx. 119 ± 5	—
Fatigue strength (MPa)	In vertical direction (Z)	Approx. 97 ± 7	—

Table 2.
Technical data for aluminum alloy AlSi10Mg powder (wt = weight, approx. = approximately).

AlSi10Mg is a casting alloy and powder type. It can be used in the field for the combination of good thermal properties and low weight. **Table 2** contains technical data for AlSi10Mg powder. It shows general process, geometrical data, physical and chemical properties of the parts, mechanical properties of the parts, and thermal properties of parts.

5. Experimental setup

A mechanical type-universal test machine (UTM) is obtained for the tension or compression test. UTM is DTU-900MHA and a mechanical type with a digital signal processor (DSP) system as shown in **Figure 4**. For the tension test, **Figure 5** shows experimental setup in the UTM. It shows uniaxial tensile test with specimen made by aluminum ally, AlSi10Mg. **Figure 5(1)** is a specimen before tensile test and **Figure 5(2)** shows a specimen after the tensile test. **Figure 5(2)** shows a circle which means zoom-out as the right figure. The right figure shows a good tested result in the specimen, because it is broken in middle area in the specimen

Figure 4.
Universal test machine (UTM) with data collector system.
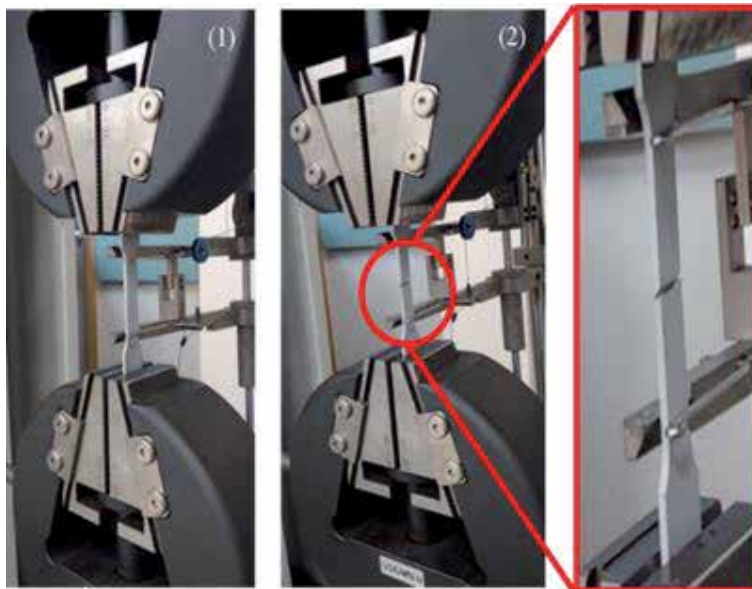
Figure 5.
Uniaxial tensile test with specimen made by aluminum alloy AlSi10Mg. Test speeding is set up as 1 mm/min: (1) shows a specimen before testing; (2) shows a specimen after testing.

as setup with mechanical extensometer. Test speeding in the UTM is setup as 1 mm per a minute.

6. Tension

Making a tensile specimen is based on ASTM E8M standard. The specimens were obtained by AlSi10Mg power with the DMSL technique. Each section defined as a letter which shows dimensions on **Table 3**. **Table 3** shows rectangular shape of tension test specimens with detail dimensions like the gauge length, width, thickness, radius of fillet, overall length, length of reduced section, a length of grip section, and an approximate width of grip section. Thus, DMLS made specimens for the tension test.

Totally, three samples made by aluminum alloy (AlSi10Mg) marked as 2–1, 2–2, 2–3 were ready for the tension test, and they were tested by uniaxial tensile testing.

Figure 6 shows specimens after tensile test and results with (a) engineering stress-engineering strain for all specimens and (b) stress-strain for 2-2 specimen. As you can see, 2–2 specimen shows clearly that the middle point was broken. Others were broken in an area of top point or bottom point. Thus, tested data were selected for 2–2 specimen because it shows a good fracture.

From the tension test, engineering stress-strain and true stress-strain can be defined as shown in **Figure 6**. **Figure 6** shows a comparison between engineering stress-strain and true stress-strain for aluminum alloy AlSi10Mg.

Dimensions of standard specimens, sheet-type [mm]	
Gauge length	50.0 ± 0.10
Thickness	3.0
Radius of fillet, min	12.5
Overall length, min	200
Length of reduced section, min	57
Length of grip section, min	50
Width of grip section, approximate	20

Table 3.
Rectangular tension test specimens based on ASTM E8M.
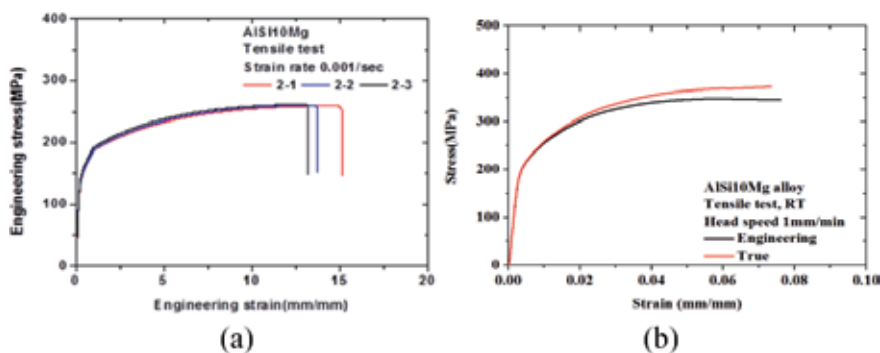
Figure 6.
Stress as a function of Stain for Aluminum alloy specimen after tensile test; (a) Engineering stress - Engineering strain for all specimens, and (b) Stress-strain for 2-2 specimen.

Material	Properties	Value
AlSi10Mg	Young's modulus (GPa)	71.8
	Yield strength (MPa)	155.5
	Ultimate tensile strength (MPa)	348.3
	Elongation (%)	8.0

Table 4.
Mechanical properties of AlSi10Mg by tension.

In order to do the tension test for AlSi10Mg, it is defined material properties are as follows: Young's modulus is 71.81GPa, yield strength is 155.52 MPa, and ultimate tensile strength is 348.32 MPa approximately. These are summarized in **Table 4**. When the Young's modulus value is compared in **Table 2**, they almost matched in vertical direction. That is, it is proved that tensile specimen is created in vertical direction by DMLS.

7. Compression

Specimens for uniaxial compression test are made by the 3D printing DMLS technique as shown in **Figure 7**. It was made by the same equipment as EOS M290 and the same material as aluminum alloy, AlSi10Mg. The sample size is designed as diameter is 10 mm and height is 15 mm as shown in **Figure 7**. The figure also shows real specimens made by aluminum alloy. For the compression test, three specimens are ready.

Two specimens are used for the compression test because both samples are almost matched in the stress-strain plot shown in **Figure 8**. Thus, material properties for the compression test with Al alloy, AlSi10Mg, are defined as follows: Young's modulus is 0.316GPa, yield compressive yield strength is 6.35 MPa, and ultimate compressive strength is 179.72 MPa. **Figure 8** shows the crushing 6 steps within a range of 0–0.6, strains and each step is defined as: ① is elastic range,
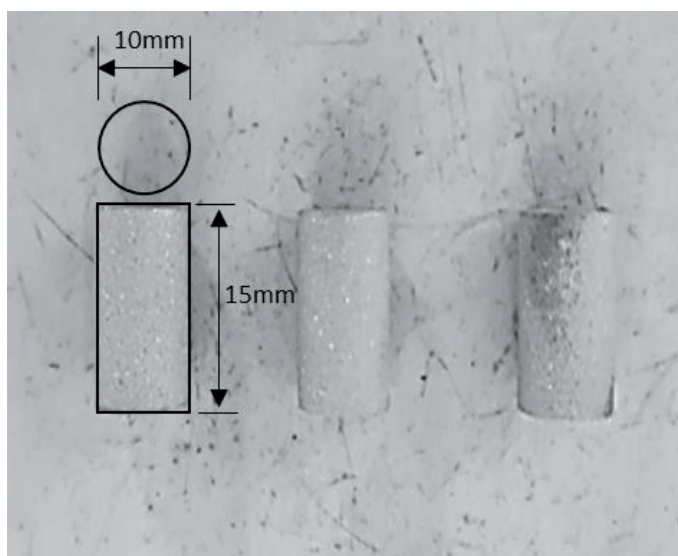
Figure 7.
Designation and AlSi10Mg specimens for compression test.
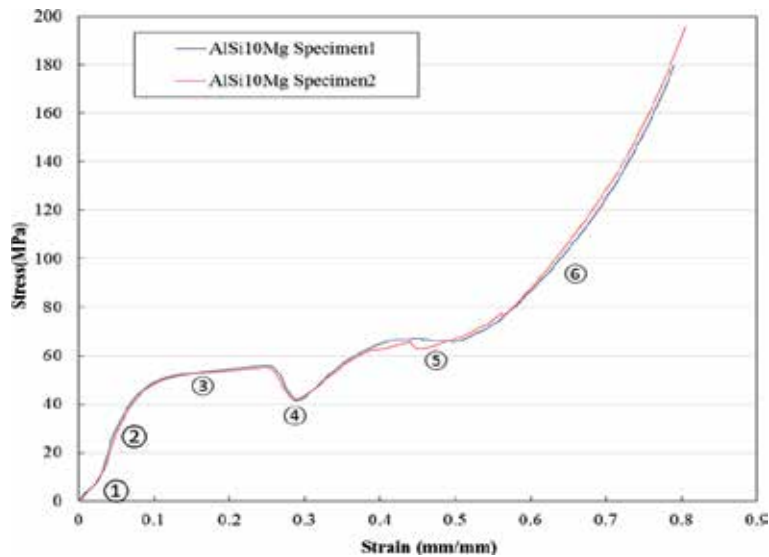
Figure 8.
Crushing steps such as ① elastic range, ② linear, ③ 1st plateau, ④ valley, ⑤ 2nd plateau, and ⑥ densification.

② linear, ③ the 1st plateau, ④ valley, ⑤ the 2nd plateau, and ⑥ densification. Thus, Young's modulus is checked in elastic range ①. Linear ② shows increasing loads. Then, 1st plateau shows in ③. In here, loading slowly increase. Valley ④ shows as being abruptly dropped, because belly phenomenon happened in the middle of 15 mm height specimen. It means endurance of applied loading in specimen is over. Then, it shows the 2nd plateau as ⑤ where applied loads slowly decreased. This means applied stress is distributed in specimen. At the end, densification ⑥ is shown.

8. 4D cube mechanical test

There are two types of model for mechanical testing. The two models are core-spaced model defined as Type 1 and core-filled model defined as Type 2. **Figure 2** shows two samples that are made by the 3D printing DMLS skill. Each sample is

Applied material	Sample type	Sample number	Width (mm)	Length (mm)	Height (mm)	Truss diameter (mm)		Weight (grams)
						Outer	Inner	
AlSi10Mg	Type 1	1	20	20	20	1.5	3	5.91
		2	20	20	20	1.5	3	5.91
		Average	20	20	20	1.5	3	5.91
	Type 2	1	20	20	20	1.5	3	5.29
		2	20	20	20	1.5	3	5.29
		Average	20	20	20	1.5	3	5.29
	Difference							11.72%

Table 5.
Measured weights for Type 1 and Type 2 model made by AlSi10Mg alloy.

121

designed as width 20 mm, length 20 mm, height 20 mm, inner truss diameter 3 mm, and outer truss radius 1.5 mm. Type 1 is core-spaced model shown in **Figure 2(1)** and Type 2 is core-filled model shown in **Figure 2(2)**.

Before the uniaxial compression test, measured weight for Type 1 is 5.91 grams and Type 2 is 5.29 grams. Difference between Type 1 and Type 2 is about 11.72% in weights. Details are summarized in **Table 5**.

Applied material is Al alloy and powder type shown in **Table 2**. Applied speeding in the UTM machine is defined as 2 mm per minute. Type 1 is core-filled model
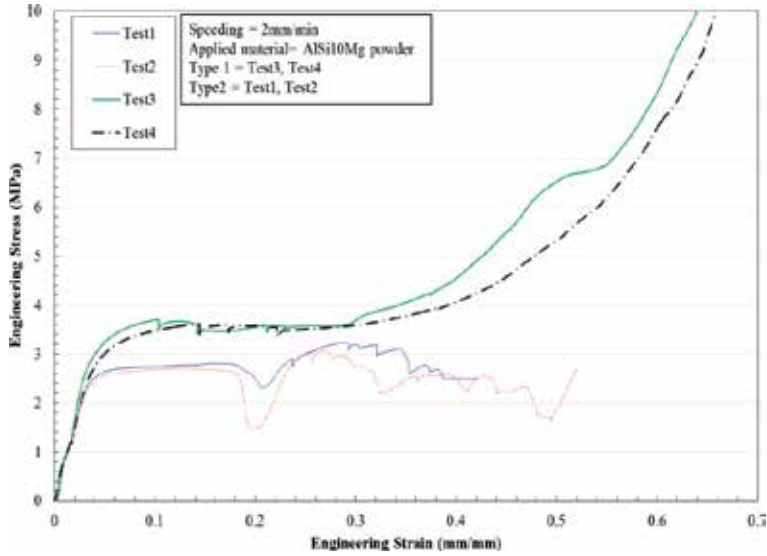
Figure 9.
Engineering stress as a function of engineering strain from uniaxial compression.
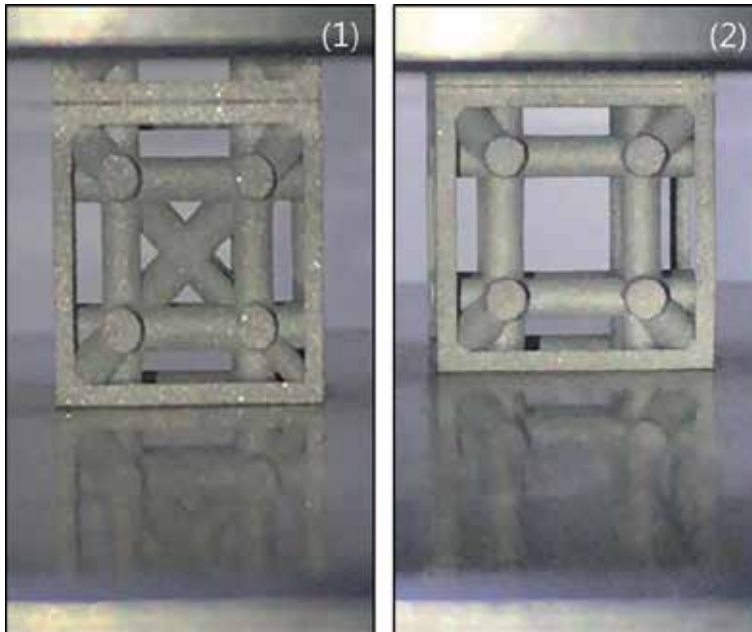
Figure 10.
Uniaxial compression test in UTM for (1) Type 1 and (2) Type 2.

Type	Sample number	Material properties			
		Young's modulus (GPa)	Compressive yield strength (MPa)	Ultimate compressive strength (MPa)	Compressibility (%)
1	Test 3	0.92	2.60	13.40	70
	Test 4	0.72	2.54	11.47	68
	Average	0.82	2.57	12.44	69
2	Test 1	0.71	2.29	3.22	42
	Test 2	0.66	2.29	3.08	49
	Average	0.69	2.29	3.15	46
Difference		19.7%	12.2%	294.8%	51.6%

Table 6.
Material properties of Type 1, core-filled model, and Type 2, core-spaced model.

of test 3 and test 4. Type 2 is core-spaced model of test 1 and test 2. Thus, tested result shows engineering stress as a function of engineering strain in **Figure 9**. Based on the compression test, **Figure 9** shows material properties for elastic modulus, compressive yield strength, ultimate compressive strength, compressibility, and so on. **Figure 10** shows setup for uni-axial compression test in UTM for (1) Type 1 and (2) Type 2 model.

For Type 1, the average values of material properties are elastic modulus is 0.82GPa, compressive yield strength is 2.57 MPa, ultimate compressive strength is 12.44 MPa, and percent compressibility is 69%, approximately. For Type 2, the average values of material properties are elastic modulus is 0.69GPa, compressive yield strength is 2.29 MPa, ultimate compressive strength is 3.15 MPa, and compressibility is 46%, approximately. **Table 5** summarizes the material properties of core-filled or core-spaced model. It shows differences between Type 1 for core-filled model and Type 2 for core-spaced model about material properties. For Young's modulus, core-filled model is higher 19.7%, compressive yield strength 12.2%, ultimate compressive strength 294.8%, and compressibility 51.6% than core-spaced model as summarized in **Table 6**.

9. Results

Material properties between core-filled model and core-spaced model are investigated. All models are based on aluminum alloy AlSi10Mg and they are made by the 3D printing DMLS technique. Finally, 4D cube models defined as core-filled as Type 1 and core-spaced as Type 2 are tested by compression. Thus, Type 1 shows a higher Young's modulus, compressive yield strength, compressive ultimate compressive strength, and compressibility. The reason is that Type 1 can endure outer loads with a diagonal truss connected with inside hexagonal truss structure. However, Type 2 can be broken easily because they do not have a diagonal truss supporting. It is simply connected with outer or inner hexagonal structure without a cross truss. Thus, Type 1 shows a general shape of compressive tested line on **Figure 9**.

However, Type 2 shows an elastic line, yield, plateau, and up down line in **Figure 9** as in test 3 and test 4. Here, the interest is in the up down line. When it is tracked by broken specimens, it is identified as a reason; that is, when specimens are made by the 3D printing DMLS skill, laser melt metal powder at first and then the
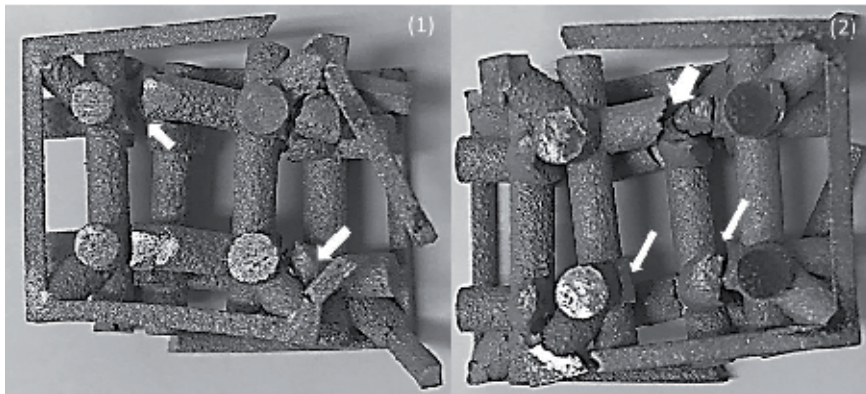
Figure 11.
Crushed samples shown as arrows: (1) core-filled model. (2) core-spaced model.

melted metal is added on each side of the truss clot by clot. Thus, each clot does not create perfect solid shape and it is not precisely connected with each truss. These are shown in **Figure 9**. Therefore, due to these reasons, material properties for 4D cube models made by the 3D printing DMLS skill show lower than solid material properties. Based on broken section in the sample (1) or (2) shown in **Figure 11**, there shows two issues. One is that melted metals are not connected with each other like a solid precisely. Due to this reason, connected sections in each model as Type 1 or Type 2 are easily broken after outer loading. These are shown as arrows in **Figure 11(1)** and **(2)**. The other one is there shows a space in additive layer when additive manufacturing makes a shape of specimen. Because of the space in the additive layer, each truss created by melted metals does not have enough to support outer loadings.

10. Conclusion

This chapter focused on finding material properties for two models defined as core-filled model, Type 1, and core-spaced model, Type 2, created by the 3D printing direct metal laser sintering (DMLS) technique. The models use aluminum alloy AlSi10Mg powder with a skill of direct laser sintering. After the uniaxial compressive test, it is proved that core-filled model has an elastic modulus of 19.7%, compressive yield strength of 12.2%, ultimate strength of 294.8%, and percentage of elongation of 11% higher than core-spaced model. It also shows core-filled model have a higher strength but core-spaced model shows a lower strength after compression. There shows two issues that melted metals by DMLS skill are not connected with each other like a solid precisely and there shows a space in additive layer when additive manufacturing makes a shape of specimen. These issues are the main reasons for weaker strength or lower elastic modulus in the models. It is hoped that the two models be made sandwich core structure and then the structure be investigated more deeply. In nearby future, it is hope that 3D printing techniques such as FDM [8, 10], SLS [9], DLP [7, 8], SLA [11, 13], LOM [11, 14], SL [14], MPSL [14], 3DP [14], FFF [15, 16], or DMLS [17, 18] are applied into making hypercube models and then it is to do the testing to check what is the differences of mechanical properties are. In addition, it is expected that hypercube models are applied into make a sandwich panel and then they are to be obtained to find mechanical properties. Finally, it is hope that the sandwich panels will be approved to be selected as one of aerospace materials.

Acknowledgements

Conflict of interest

I confirm there are no conflicts of interest.

Notes/thanks/other declarations

Many thanks go to Dr. Sang-ik Lee for doing this project.

Author details

Jeongho Choi
School of Mechanical Engineering, College of Engineering, Kyungnam University, Chang-won, Republic of Korea

*Address all correspondence to: choicaf@gmail.com

IntechOpen

References

[1] Eugenio B, Carlo C, Marco L. Shape/size of truss structures using optimization for non-probabilistic description of uncertainty. Transactions on the Built Environment—Computer Aided Optimum Design of Structures V. 1997;**28**:163-172. DOI: 10.2495/OP970161

[2] Bertsekas DP, Ozveren C, Stamoulis GD, Tseng P, Tsitsiklis JN. Optimal communication algorithms for Hypercubes. Journal of Parallel and Distributed Computing. 1991;**11**:263-275. DOI: 10.1016/0743-7315(91)90033-6

[3] Ostrouchov G. Parallel computing on a hypercube-An overview of the architecture and some applications. Oak Ridge National Lab. CONF-8703131-1. DOE: AC05-84OR21400

[4] Mane SA. Structure connectivity of hypercubes. AKCE International Journal of Graphs and Combinatorics. 2018;**15**:1. DOI: 10.1016/j.akce.2018.01.009

[5] Harary F. A survey of the theory of hypercube graphs. Computers & Mathematics with Applications. 1988;**15**:277-289. DOI: 10.1016/0898-1221(88)90213-1

[6] Mane SA. Structure connectivity of hypercubes. AKCE Int. J. Graphs Comb. 2018;**15**:49-52. DOI: 10.1016/j.akcej.2018.01.009

[7] Gibson LJ, Ashby MF. Cellular Solids—Structure and Properties. 2nd ed. Cambridge, United Kingdom: Cambridge University Press; 1997. DOI: 10.1017/CBO9781139878326

[8] Song Y, Li Y, Song W, Yee K, Lee K-Y, Tagarielli VL. Measurements of the mechanical response of unidirectional 3D-printed PLA. Materials & Design. 2017;**123**:154-164. DOI: 10.1016/j.matdes.2017.03.051

[9] Gibson I, Shi D. Material properties and fabrication parameters in selective laser sintering process. Rapid Prototyping Journal. 1997;**3**:129-136. DOI: 10.1108/13552549710191836

[10] Kulkarni P, Dutta D. Deposition strategies and resulting part stiffnesses in fused deposition modeling. Journal of Manufacturing Science and Engineering. 1999;**121**:93-103. DOI: 10.1115/1.2830582

[11] Feng P, Meng X, Chen JF, Ye L. Mechanical properties of structures 3D printed with cementitious powders. Construction and Building Materials. 2015;**93**:486-497. DOI: 10.1016/j.conbuildmat.2015.05.132

[12] Hornbeck LJ. Digital light processing update: Status and future applications. In: Proceeding SPIE3634, International Society for Optics and Photonics Projection Displays V (Electronic Imaging'99); 20 May 1999; San Jose, CA, United States. 1999. pp. 158-170

[13] Ikuta K, Hirowatari K, Ogata T. Three dimensional micro integrated fluid systems (MIFS) fabricated by stereolithography. Micro electro mechanical systems. In: Proceedings IEEE Micro Electro Mechanical Systems an Investigation of Mirco Structures, Sensors, Actuators, Machines and Robotic Systems (MEMS'94); 25-28 January 1994. Siso, Japan: IEEE Workshop on; IEEE; 1994. pp. 1-6

[14] Engkvist G. Investigation of microstructure and mechanical properties of 3D printed Nylon [thesis]. Materials Engineering: Lulea University of Technology; 2017

[15] Basgul C, Yu T, MacDonald DW, Siskey R, Marcolongo M, Kurtz SM. Structure-property relationships for 3D-printed PEEK intervertebral

lumbar cages produced using fused filament fabrication. Journal of Materials Research. 2018;**33**:2040-2051. DOI: 10.1557/jmr.2018.178

[16] Mohseni M, Hutmacher DW, Castro NJ. Independent evaluation of medical-grade bioresorbable filaments for fused deposition modelling/ fused filament fabrication of tissue engineered constructs. Polymers. 2018;**10**:1-17. DOI: 10.3390/polym10010040

[17] Kundu S, Hussain M, Kumar V, Mumar S, Das AK. Direct metal laser sintering of TiN reinforced Ti6Al4V alloy based metal matrix composite-fabrication and characterization. The International Journal of Advanced Manufacturing Technology. 2018;**97**:2635-2646. DOI: 10.1007/s00170-018-2159-7

[18] Alsalla HH, Smith C, Hao L. The effect of different build orientations on the consolidation, tensile and fracture toughness properties of direct metal laser sintering Ti-6Al-4V. Rapid Prototyping Journal. 2018;**24**:276-284. DOI: 10.1108/RPJ-04-2016-0067

[19] Cantrell J, Rohde S, D0amiani D, Gurnani R, diSandro L, Anton J, et al. Experimental characterization of the mechanical properties of 3D printed ABS and polycarbonate parts. In: Yoshida S, Lamberti L, Sciammarella C, editors. Advancement of Optical Methods in Experimental Mechanics. In: Proceedings of the Society for Experimental Mechanics Series Book Series (CPSEMS'17). Cham: Springer; 2017. pp. 89-105

[20] Leite M, Fernandes J, Deus AM, Reis L. Study of the influence of 3D printing parameters on the mechanical properties of PLA. In: 3rd International Conference on Progress in Additive Manufacturing (pro-AM 2018); 14-17 May 2018; Singapore. 2018

[21] Salet TAM, Ahmed ZY, Bos FP, Laagland HLM. Design of a 3D printed concrete bridge by testing. Virtual and Physical Prototyping. 2018;**13**:222-236. DOI: 10.1080/17452759.2018.1476064

[22] Mehta LS, Pillai P. Compression testing of PLA in 3D printing. International Journal of Electronics, Electrical and Computational System (IJEECS). 2017;**6**:466-470. ISSN: 2348-117X, DOI: No Data

[23] Divyathej MV, Varun M, Rajeev P. Analysis of mechanical behavior of 3D printed ABS parts by experiments. International Journal of Scientific and Engineering Research. 2016;**7**:116-124. ISSN: 2229-5518, DOI: No Data

[24] Hernandez R, Slaughter D, Whaley D, Tate J, Asiabanpour D. Analyzing the tensile, compressive, and flexural properties of 3D printed ABS P430 plastic based on printing orientation using fused deposition modeling. In: Proceedings of the 27th Annual International Solid Freeform Fabrication Symposium—An Additive Manufacturing Conference Reviewed Paper (Solid Freeform Fabrication 2016). 2016. pp. 939-950

[25] ASTM E8/E8M-13. Standard Test Methods for Tension Testing of Metallic Materials. West Conshohocken, PA: ASTM International; 2013. Available from: www.astm.org. DOI: 10.1520/E0008_E0008M-13

Edited by Aykut Kentli

This book presents the application of new techniques in analyzing truss and frame structures. The book contains two main sections: Numerical Analysis of Structures and Mass-Saving in Structures. Under each section, different approaches on the topic are given. Covered in these sections are dynamic stability analysis, design optimization considering vibration, FEM analysis, topology optimization methods, and recommendations to build lightweight structures. It is believed that this book will be helpful to its readers for new perspectives on the analysis of structures.

IntechOpen